# Investigation of Transonic Buffet Reduction Devices Using Pressure Sensitive Paint

Master of Science Thesis

Zyanya Rabilotta

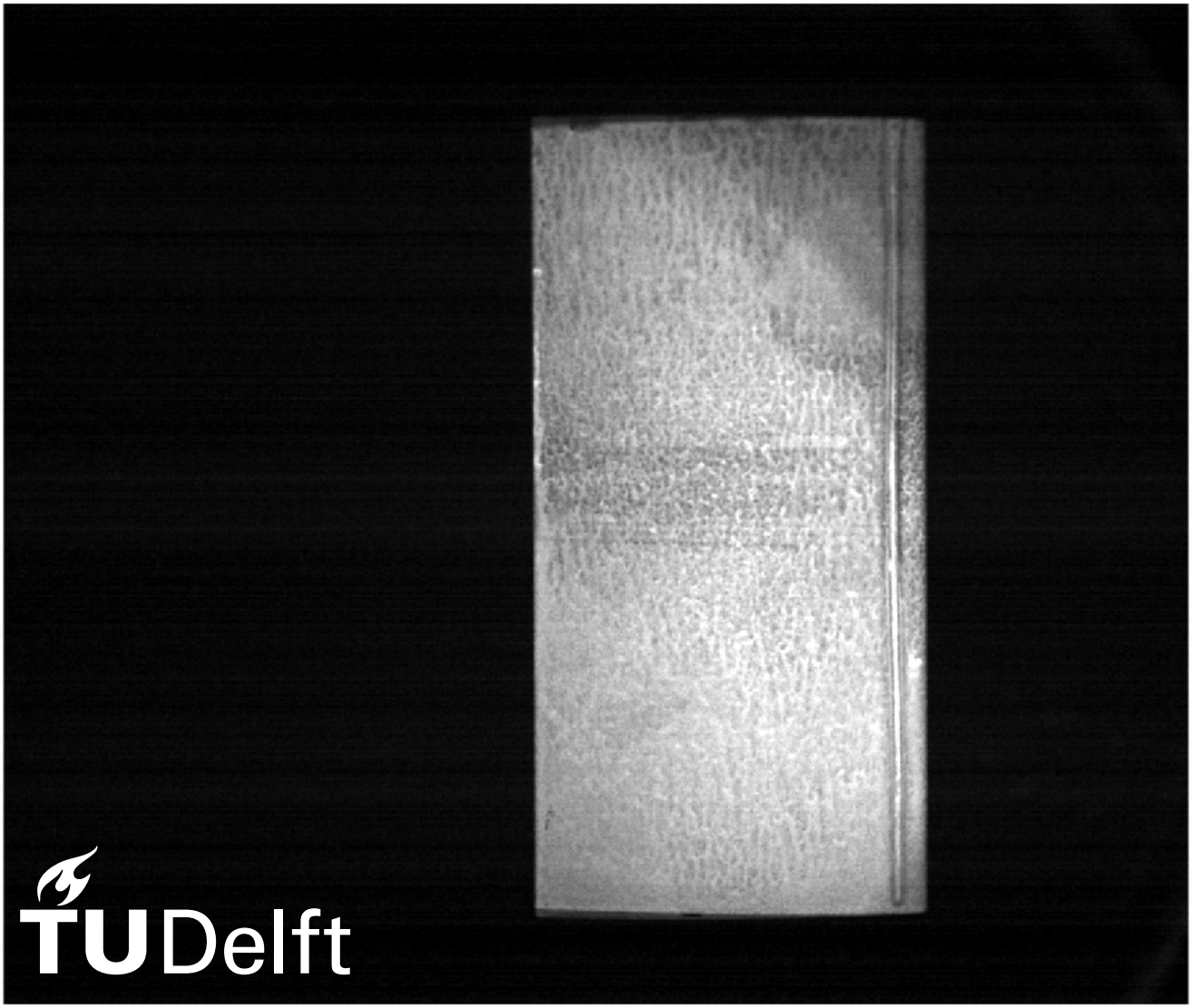

TU Delft

# Investigation of Transonic Buffet Reduction Devices Using Pressure Sensitive Paint

by

Zyanya Rabilotta

Student: Zyanya N. Rabilotta Yañez
Thesis committee:
Dr. ir. B. W. van Oudheusden — Chair
Dr. ir. F. F. J. Schrijer — Supervisor
Dr. D. Ragni — Examiner
Dr. A. D'Aguanno — Additional

Faculty of Aerospace Engineering, TU Delft
March 2023

TU Delft

# Acknowledgements

The last two years have been an experience, to say the least. From wind tunnels that did not work, to part of the equipment stranded in Rotterdam for months, to the normal struggles that come with writing a master thesis.

I would like to start by thanking Ferry and Bas for being there throughout this entire time, without whom I might not have completed this work. I would also like to thank Peter, Frits, Dennis and Henk-Jan who helped make the experiments possible.

A big thanks to all of my friends and family who have been there for mental and emotional support throughout these past years.

*Zyanya Rabilotta*
*Delft, March 2023*

# Executive Summary

The transonic regime is of great interest for designing aircraft wings because most aircraft fly in transonic conditions. The problem with flying in transonic is the severe instability that occurs. This instability gives rise to the phenomenon known as buffet, which is responsible for shock wave oscillations.

Two remarkable developments in aerofoil design that improve the flow during transonic conditions are the supercritical aerofoil and shock control bumps. The supercritical aerofoil has a geometry with a flatter upper surface than a conventional aerofoil. This difference in the upper contour ensures a smaller pressure jump, causing a weaker and more aft shock wave. Shock control bumps are an external geometry added on top of the upper surface of the aerofoil. Their shape resembles that of a triangular "bump", hence the name. They work by splitting the man shock wave into multiple ones, thus weakening the shock.

Pressure sensitive paint is a non-intrusive flow measurement technique. This paint works by a principle known as oxygen quenching. This process involves the luminophores in the paint molecules either reacting with the oxygen in the environment or emitting a photon back due to luminescent excitation. Depending on the amount of oxygen available, a camera captures a different luminescent emission due to the different experienced surface pressure on that region.

The objective of this research is to obtain the average pressure and lift coefficient during transonic conditions using pressure sensitive paint as the flow measurement technique. The model for the study consists of the ONERA OAT15A supercritical aerofoil with and without shock control bumps in the TST-27 wind tunnel at the TU Delft.

The data from the experiments show promising results regarding the overall qualitative pressure distribution. However, due to the shortage of temperature data and other errors, the measured pressure values are shifted from the actual values. This results in partially fulfilling the objective of the study due to the wrong lift coefficients computed with the data.

# Contents

# List of Figures

# List of Tables

# Nomenclature

## Abbreviations

| Abbreviation | Definition |
|---|---|
| PSP | Pressure sensitive paint |
| SCB | Shock control bump |
| TST-27 | Trans/supersonic wind tunnel |
| RMS | Root mean square |
| STD | Standard deviation |

## Symbols

| Symbol | Definition | Unit |
|---|---|---|
| $V$ | Velocity | [m/s] |
| $c$ | Speed of light | [m/s] |
| $C_L$ | Lift coefficient | [-] |
| $C_p$ | Pressure coefficient | [-] |
| $E_{photon}$ | Excitation photon energy | [J] |
| $h$ | Planck's constant | [Js] |
| $I$ | Measured intensity | [-] |
| $I_0$ | Background intensity | [-] |
| $k_D$ | Deactivation terms decay rate | $[s^{-1}]$ |
| $k_P$ | Photon emission decay rate | $[s^{-1}]$ |
| $k_Q$ | Oxygen quenching decay rate | $[s^{-1}]$ |
| $M$ | Mach number | [-] |
| $M_{crit}$ | Critical Mach number | [-] |
| $M_\infty$ | Freestream Mach number | [-] |
| $p$ | Pressure | [Pa] |
| $Re$ | Reynolds number | [-] |
| $\alpha$ | Angle of attack | $[^o]$ |
| $\delta$ | Excitation wavelength | [m] |
| $\rho$ | Density | $[kg/m^3]$ |

# 1

# Introduction

When an aircraft is flying in the transonic flow regime, the wing of the aircraft tends to experience a phenomenon known as buffet. The buffet phenomenon has been deeply studied in the past century. However, this phenomenon is still far from fully understood. The transonic regime is known for not always being stable. A reason for this is the complexity in the physics that govern buffet, which is responsible for causing an oscillation of the shock wave(s) on the geometry that is experiencing buffet. This shock oscillation prevents the proper measurement of the surface pressure of aerofoils and wings at transonic conditions due to the unsteady nature of this flow regime. Therefore, a way of obtaining the average surface pressure on the tested models is required. By doing so, the buffet phenomenon can be better-taken care of when designing a wing.(Gianelis, Vio, and Levinski (2017) and D'Aguanno, Schrijer, and Oudheusden (2019))

There are multiple methods of improving the performance of a wing when it is experiencing the transonic regime. The first approach is designing a wing with a supercritical aerofoil. The reason for this is that the upper shape supercritical aerofoil is flatter, which ensures the delay in drag rise and thus a delay in the transonic buffet as stated by Whitcomb (1974). The second approach is using shock control bumps (SCBs), which passively control the shock by modulating the flow, as found in the work of Bruce and Colliss (2014).

Obtaining accurate pressure measurements in the transonic regime is challenging, due to the surface pressure not remaining constant. Pressure sensitive paint (PSP) is a flow measurement technique that has not been used in the high-speed wind tunnel of the TU Delft so far. However, this technique is promising regarding its ability to measure the surface pressure of a model during buffet. PSP is a technique that consists of a paint that reacts with the oxygen found in the environment, as stated by Liu and Sullivan (2005) and Jahanmiri (2011). Not only do the molecules in the paint react with the oxygen, but they can also change their charge state through laser excitation. This means that a light source consisting of a specific wavelength aimed at the paint will cause the paint molecules to become charged. The charged molecules will then emit a photon with a characteristic wavelength as found in the works by Liu and Sullivan (2005) and Gouterman (1997). By recording the intensity emitted by the paint molecules and applying the Stern-Volmer equation, the surface pressure is computed (Liu and Sullivan (2005)). The PSP technique could eventually lead to the average surface pressure of the models tested in the wind tunnels of the TU Delft, which means that the average pressure and lift coefficients of aerofoils can be experimentally obtained during buffet.

The purpose of this report is to present the experimental research done to fulfil the objective

of **applying pressure sensitive paint to measure the average pressure distribution in a transonic wind tunnel to study the effect of shock control bumps on a supercritical airfoil during buffet.**

## 1.1. Report setup

The report first introduces the concept and physics of the buffet phenomenon. Secondly, Chapter 3 presents the physics of PSP to the reader. The chapter starts with the background on the basic principle of PSP, which is luminescence (photon emission) and oxygen quenching. The two most common methods, lifetime and intensity, of PSP are also treated. Chapter 4 deals with the methodology and experimental setup. The chapter starts by explaining how the method for calibrating and using PSP works. This is followed by an explanation of the experimental setup necessary for the experiments. Chapter 5 explains why and how the data is processed, which is also done by means of going through the calibration process. The calibration process also serves as the validation of PSP as a flow measurement technique. The calibration also serves to find the pressure trend when using PSP as a measurement technique. The results are in Chapter 6, which starts with the results from the validation experiments followed by the results from the main experiments. The results are followed by a discussion in Chapter 7. Finally, Chapter 8 gives the conclusion from the experiments.

# 2

# The Buffet Phenomenon

The purpose of this chapter is to present the buffet phenomenon as well as the effects of having a supercritical aerofoil and shock control bumps in the design regarding the model's performance when experiencing transonic conditions. This goal is achieved by briefly discussing high subsonic speeds, followed by introducing the buffet phenomenon. Then, the section about supercritical aerofoils provides the reader with basic information about this aerofoil geometry. The chapter then continues with an explanation of shock control bumps. The chapter ends with a recap of the provided data.

## 2.1. Transonic Aerodynamics and Critical Mach number

Transonic aerodynamics is a branch of aerodynamics concerned with the flow of gases that have a velocity close to the speed of sound. Many conventional aircraft fly in the transonic regime. However, flying at these speeds can cause flow instabilities. Thus, for achieving the optimum aerodynamic performance of the aircraft, a good understanding of this regime is necessary.

Transonic flow occurs when there is a freestream with Mach numbers ranging from 0.6 to 1.2, this causes a mix of sub-and supersonic flow inside the same flow field region, see Figure 2.1. The supersonic region is terminated by a shock wave which allows the flow to slow down to subsonic speeds. The mix of sub-and supersonic flow leads to the critical Mach number, which is the lowest Mach number that causes the airflow at some point on the geometry to reach the speed of sound without exceeding it (Mason (2006)). Therefore, a weak shock wave is spotted. The value for the critical Mach number is dependent on the geometry of the aerofoil. A thicker wing will deflect the airflow more than a thin wing, causing the critical Mach number to be lower because by deflecting the airflow and accelerating the airflow to a higher speed.

For Figure 2.1, where the Mach number is 0.5, the maximum local velocity is still subsonic. Once the Mach number reaches a value of 0.72, there is a point on the aerofoil with a sonic speed which means that 0.72 would be considered the critical Mach number. After the Mach number reaches 0.77, a supersonic region on the top of the aerofoil forms creating a shock wave. After the shock wave, the flow becomes subsonic again, and separation can exist. After a Mach number of 0.82, there is supersonic flow in both upper and lower regions on the aerofoil, and separation occurs after the shock wave. When the Mach number has trespassed 1.0, there is a bow wave that forms before the aerofoil, and there are shock waves at the trailing edge.

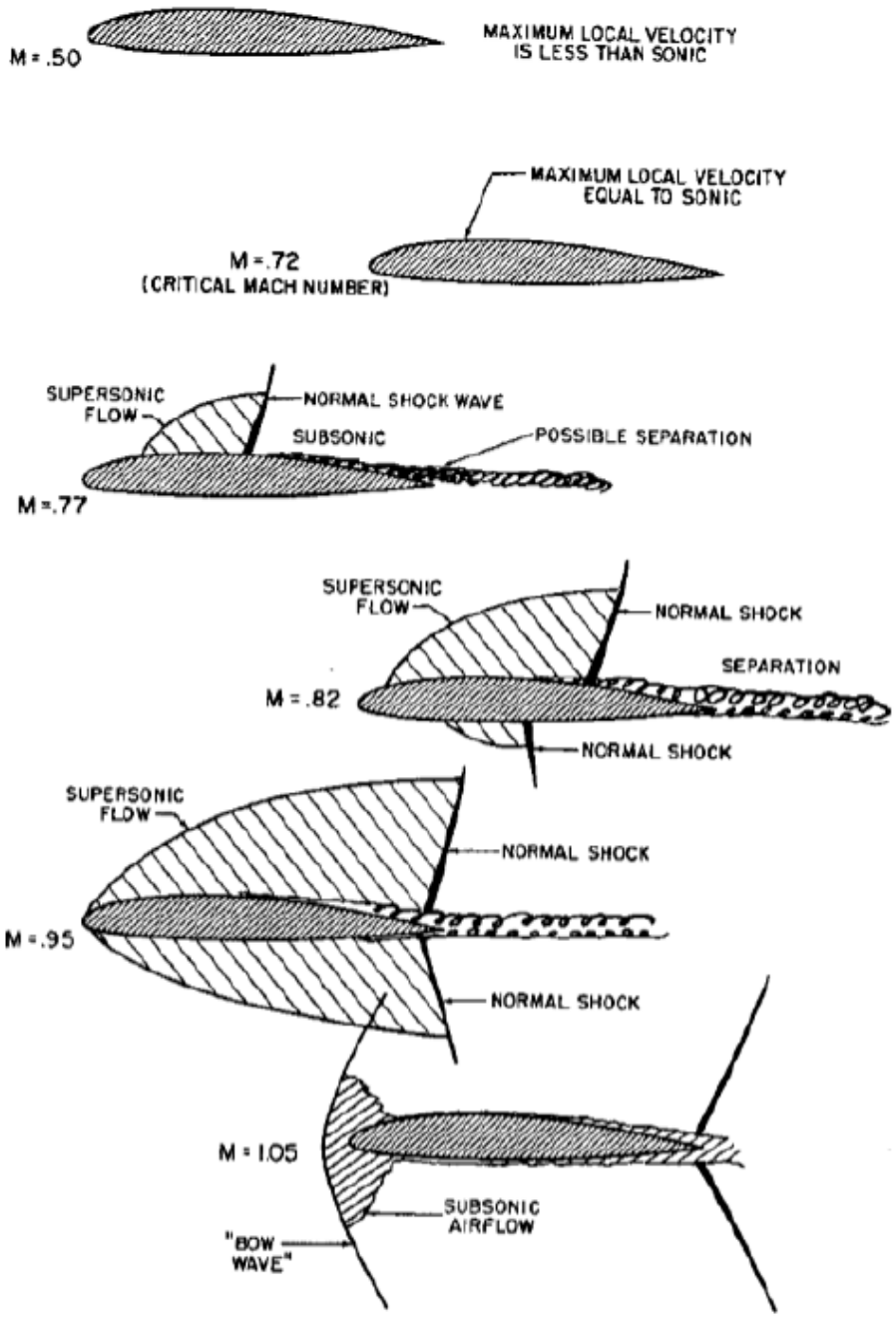


**Figure 2.1:** Effects on the flow field from increasing Mach number (in the transonic regime). (Mason (2006))

### 2.1.1. High Subsonic Speeds

High subsonic speeds above the critical Mach number create a shock wave on an aerofoil. The shock occurs due to the formation of a supersonic region on the upper surface of the aerofoil. The purpose of the shock wave is to decelerate the supersonic flow to subsonic speeds. The different aspects of the shock, such as its position and strength, are dependent on multiple factors. These factors are the Mach number, the circulation of the flow and its geometry. The boundary layer, which is a layer of air in contact with the airfoil's surface, at the foot of the shock wave thickens by an abrupt rise in the pressure, and separation may occur at that location. Even when the boundary layer experiences no separation, it still affects the shock

and influences the flow quality that separates and forms the wake. The separation causes the outer flow to experience the aerofoil's geometry as less cambered than it is in reality, which decreases the production of circulatory flow at the trailing edge. The generation of shock waves leads to the generation of wave drag due to entropy production. Therefore, the shock affects the boundary layer by increasing the separation of the boundary layer. It also decreases the lift generated by the aerofoil in the process, see Figure 2.2. The reason for this is that to generate lift is necessary to have circulation. The circulation creates a difference between the pressure experienced by the aerofoil's upper and lower surfaces. (Sobieczky and Seebass (1984))

It is worth noticing that different drag sources can diminish the aerofoil's performance. A common type of drag is skin friction drag, that as the name suggests, is caused by the friction between the aerofoil and the air. Another common type is pressure drag, which is dependent on the cross-sectional area of the front of the object, in this case, an aerofoil. So the more blunt and larger the frontal cross-section is, the larger its pressure drag. Finally, another type of drag is a lift-induced drag. For example, at lower speeds, a greater angle of attack provides a higher lift coefficient. However, due to the increase in the angle of attack, the air ends up pushing the aerofoil backwards. And this is responsible for an increase in the induced drag. (Anderson (2011))

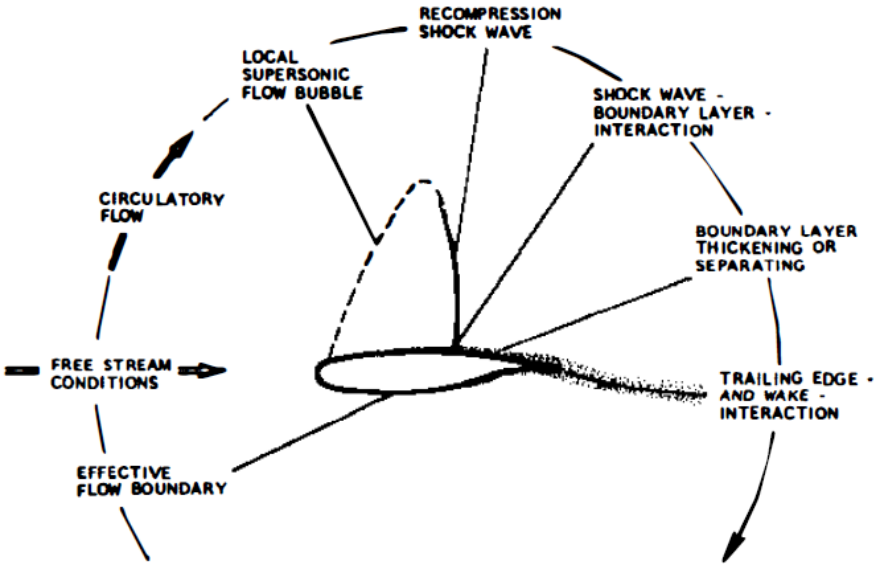


**Figure 2.2:** Transonic airflow with viscous interactions (Sobieczky and Seebass (1984)).

## 2.2. Buffet

Buffet is a phenomenon that occurs inside the transonic regime. This phenomenon consists of the interaction between shock waves and the wake, which gives rise to shock oscillations. Buffet occurs when certain conditions such as the angle of attack, the Mach- and the Reynolds number are at specific values, which cause boundary layer separation close to the foot of the shock wave. The separation influences the shock's motion towards the leading edge while it gains intensity due to the large difference in velocities between the incoming flow and the shock. When the shock wave is near the location where the turbulent boundary layer is generated, thus in the direction upstream of the flow, the shock intensity starts to decrease due to the thinner boundary layer in that specific region and the separation bubble behind it pushing it upstream.

During this upstream motion, the shock begins to reattach. The reattachment of the shock causes the shock to become stronger and reverse direction and move downstream. The motion is repeated in a periodic manner creating self-sustained shock oscillations. Figure 2.3 shows the shock buffet cycle more clearly. Figure 2.3 (a) shows the shock at its most downstream position on the aerofoil, and the interaction between the separation bubble and the shock foot is visible. In Figure 2.3 (b), the shock has moved more upstream due to the pressure that the separation exerted on the shock self. At its most upstream position, (c), the shock is the weakest and the separated region downstream of the shock starts to reattach. As the separated flow starts to reattach, the shock increases in strength, as seen in (d), completing and restarting the cycle.(Iovnovich and Raveh (2012))

### 2.2.1. Types of buffet

The high amplitude with a low-frequency motion of a shock wave characterises the unsteady oscillatory phenomenon of buffet (Hilton and Fowler (1952)). Both numerical and experimental research identified two distinct types of buffet.

- Type I encompasses shock oscillations on the aerofoil's pressure and suction surfaces. This type occurs at a zero incidence on biconvex sections. For instance, a NACA 00XX airfoil has both the lower and upper surfaces that are convex. The complex interaction between the shock wave and the boundary layer generates phase-lock oscillation on the aerofoil. Furthermore, the shock weakens as it moves upstream. This motion permits the reattachment of the separated region and drives the shock downstream. On the lower surface, the motion of a shock has a similar manner, but with a phase delay of half a period. These motions yield a shock buffet cycle that is self-sustained. (Gianelis, Vio, and Levinski (2017))
- Type II deals with the upper surface shock oscillations at non-zero angles of attack, which is characteristic of supercritical aerofoils nowadays. The second type of buffet has two distinct models. Model A consists of a shock-induced separation bubble and model B, for which the trailing edge separation is either additionally present or in development. Model B has three variants. Variant I has a rear separation provoked by the formation of a bubble. Variant II has a rear separation provoked by the shock, and variant III has a rear separation present from the outset. Throughout the thesis work, it is expected to collect data to have a better understanding of this type of buffet. (Gianelis, Vio, and Levinski (2017) and Terlizzi (2020))

Tijdeman (1977) characterised three distinct types of shock motion during buffet by looking at the sinusoidal flap deflections on a NACA 64A006 aerofoil. Figure 2.4 displays the different types of motion. The first type of shock motion is type A, which consists of sinusoidal shock oscillations. The location of the shocks is on the upper surface of the aerofoil. This shock is present during the entire time the aerofoil experiences buffet. However, the shock varies in strength. When the shock is moving upstream, then its maximum strength is achieved. Type A happens for the highest Mach number, $M_\infty$=0.9. Analysing this case with the model he proposed, Tijdeman (1977) stated that when in the unsteady case, f=120Hz, two changes occurred: "a phase shift and an amplification of the variation in shock strength.". This means that the maximum strength of the shock is reached after the shock has moved from its most backward position. The motion of the shock remains larger than one through the entire cycle, which means that the shock remains present during the entire time.

The second type is B, which consists of a form of shock motion similar to type A. However, it experiences a larger variation in the magnitude of the shock strength. This leads to the shock

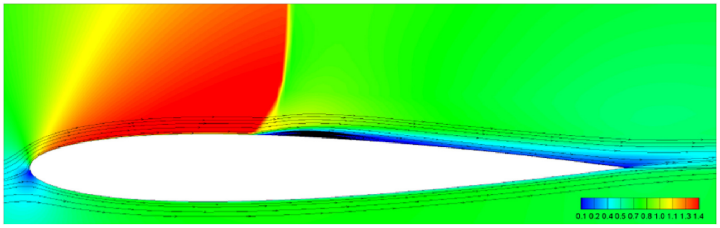

(a) Downstream shock

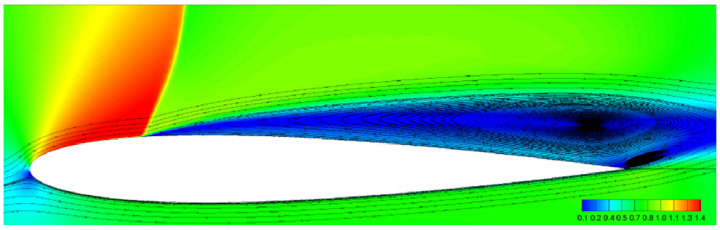

(b) Central shock (upstream excursion)

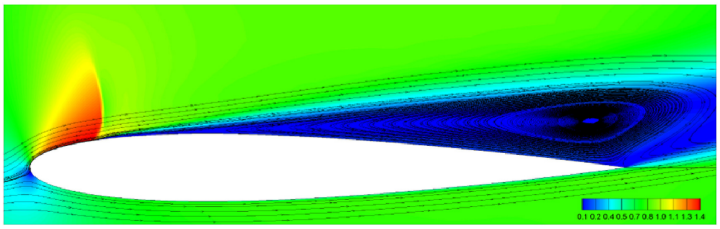

(c) Upstream shock

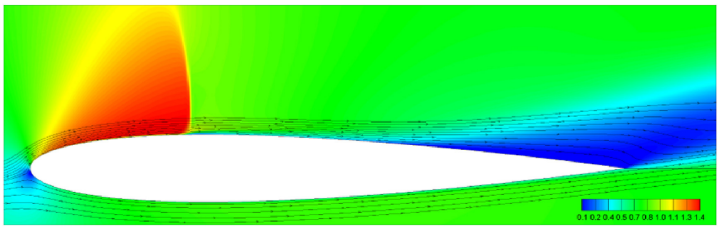

(d) Central shock (downstream excursion)

**Figure 2.3:** The buffet cycle of the NACA 0012 for Mach 0.72 at an angle of attack of $6^o$. (Iovnovich and Raveh (2012))

disappearing during its downstream excursion. This type of shock occurs when the Mach number of the free stream is slightly lower than for the previous case, $M_\infty$=0.875. The results from his analysis made suggested that in-phase variation was also applicable to this case. However, at the same frequency of 120Hz, the shock strength was lower than one for a part of the cycle. This magnitude variation means that the shock vanishes during the downstream

excursion. (Tijdeman (1977))

Finally, the third motion type was called type C. This motion was recorded at a Mach number of $M_\infty$=0.85. This motion is different from the previous ones because in this case, the shock continues to move forward while it strengthens and weakens. The shock eventually propagates as a free shock wave into the oncoming flow. From his analyses, Tijdeman (1977) noticed that during part of the shock cycle, the amplitude of the shock motion became extremely large. The large amplitude led to a shock strength smaller than one during said part of the cycle. Thus, shock disappearance occurred when the shock strength decreased below one. (Tijdeman (1977))

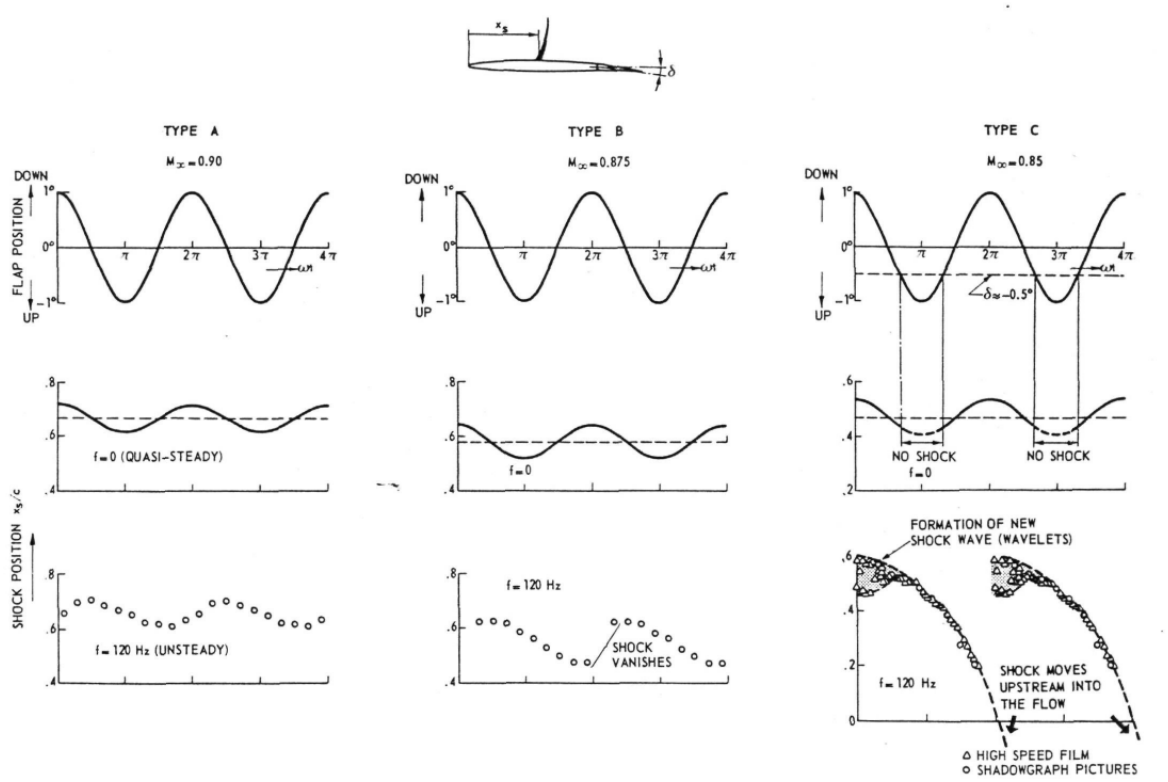


**Figure 2.4:** Observed types of periodical shock-wave motion on the upper surface. (Tijdeman (1977))

## 2.2.2. Physics of buffet

This subsection aims to explain the governing physics of the buffet phenomenon. The physics behind this aerodynamic phenomenon is a complicated matter due to the interaction between the boundary layer and shock, which induces shock oscillations possessing a large amplitude.

### Wave-propagation Feedback

The wave-propagation feedback consists of a feedback loop. The energy exchange between the upstream propagating pressure waves and the shock is responsible for creating the feedback loop. The energy exchange happens when the pressure waves and the shock interact with each other. This loop sustains itself as a periodic shock oscillation. The time necessary for disturbances to propagate downstream to the trailing edge and back upstream is essential as the shock cycle is dependent on its period of time. (Gianelis, Vio, and Levinski 2017)

Lee (1990) proposed the model in which the periodic shock motions result from the wave-propagation feedback mechanism, Figure 2.5 shows the proposed model. In the illustration, the shock motion generated propagating waves downstream of the flow with a velocity of $a_p$ occurring in the wake of the airfoil can be seen. These propagating pressure waves travel from the separation point through the shear layer, increasing the instability. When the disturbances are close to the trailing edge, pressure waves are generated in the upstream direction satisfying the unsteady Kutta condition, which deals with the vortex sheet formations generated at sharp edges. The waves generated in the upstream direction move in the subsonic region towards a velocity equal to $a_u$, which causes an interaction between the shock and the pressure waves. This interaction creates an exchange of energy which completes the feedback loop and, thus the also the periodic shock oscillation. (Gianelis, Vio, and Levinski (2017))

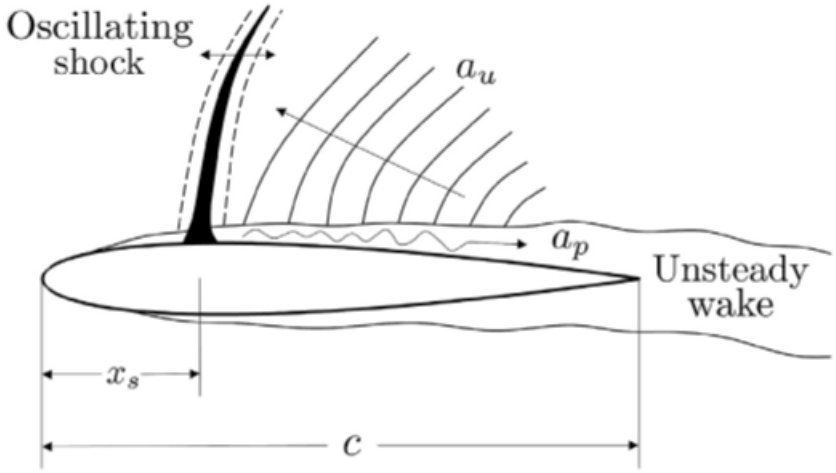


**Figure 2.5:** Model of self-sustained shock oscillation for a symmetric aerofoil (Lee (1990) and Gianelis, Vio, and Levinski (2017))

**Transonic Pre-stall Instability**

As the shock moves upstream, the shock strength increases, which causes the separated shear layer to thicken. As this happens, three effects take place (Gianelis, Vio, and Levinski (2017)): the first one is the effect caused by the separated region behaving similarly to a wedge on the upper surface. Because of this, the flow separation occurs at the foot of the shock. The pressure rise originating from the shock causes the flow separation. The second effect is known as the dynamic effect. As this effect occurs, the relative Mach number of the upstream flow increases as the shock moves upstream. The strength of the shock is dependent on the square of the Mach number. So strengthening of the shock rises. The third and final effect is the effect due to the curvature of the aerofoil. The curvature of the aerofoil plays an important role in the expansion of the flow going over it, where a greater local curvature causes a reduction in shock strength. The previously mentioned buffet cycle with the effects can be seen in Figures 2.3 and 2.6. However, due to the lower angle of attack and the greyscale, Figure 2.6 is less clear than in Figure 2.3 but the shock oscillation is still clear.

**Relation Between buffet and Lift Coefficient**

The maximum lift generated by an aerofoil in transonic speeds is highly affected by buffet (Vos and Farokhi (2015)). From previous sections, it can be concluded that the buffet region is unstable while the shock is moving from back to front in a periodic manner while occasionally

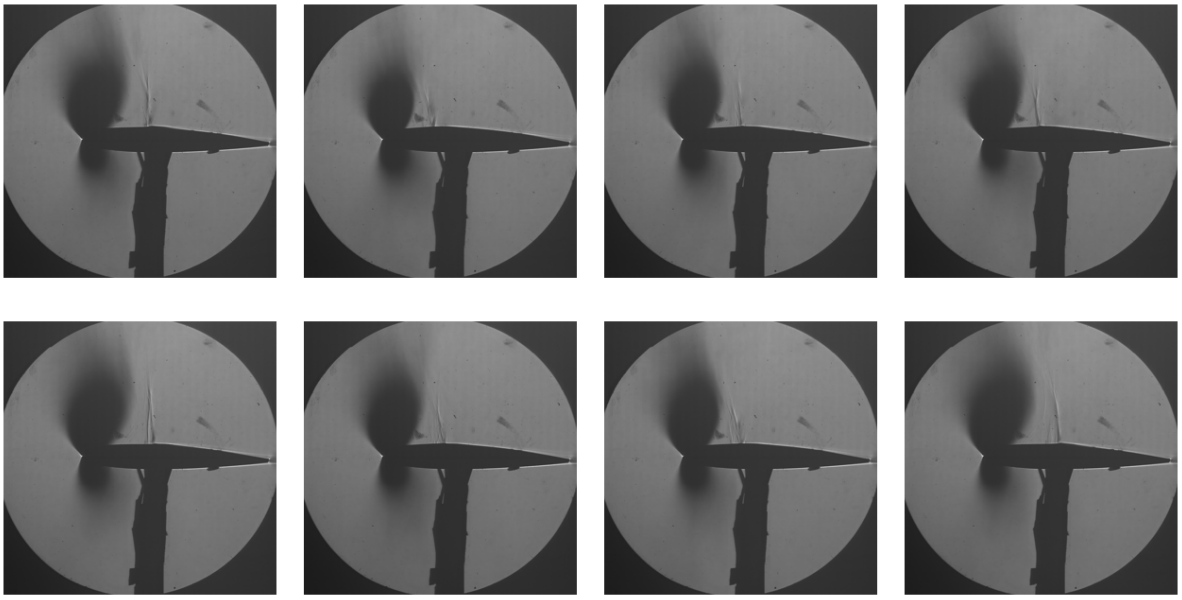

**Figure 2.6:** Consecutive Schlieren photographs of the NACA 0012 aerofoil at the TST-27 wind tunnel to showcase the buffet phenomenon for the pre-stall instability. At Mach 0.7 and $2^o$ angle of attack.

vanishing in parts of the cycles. Thus the pressure on the upper surface of the aerofoil continuously changes while experiencing transonic conditions. Furthermore, when the Mach number is very close to one, instead of having the shock more towards the end of the aerofoil when M<1, it will be in front of the aerofoil when M>1, Figure 2.1 shows this. Moreover, Figure 2.7 shows how the separation behaves relatively with the Mach numbers and the lift coefficients. Near transonic conditions, the lift coefficient drastically decreases, and it reaches a minimum at Mach 1.0. During the computation and analysis of the data collected from the experiments for this thesis, emphasis on the lift coefficient at transonic speeds will happen.

### 2.2.3. Control of Transonic Shock Oscillation

Designing the wing of an aircraft requires controlling the shock oscillations when in the transonic regime. It is crucial to have some control of the shock oscillations that happen in the transonic regime. Different methods for controlling the shock oscillations are applied to decrease the adverse effects of the transonic buffet. The first one is the use of trailing edge deflections. Trailing edge deflections can alter the flow state and make it a stable region; however, they can often increase the drag. Therefore, these methods are often undesirable for the control of shock oscillations. (Gianelis, Vio, and Levinski (2017))

The second is by using vortex generators, which promote attached flow and inhibit the shock-induced separation. The generators energise and stabilise the boundary layer to achieve the attached flow. The vortex generation method of control also comes with some drag penalties at lower angles of attack. The extra energy caused by the vortex generators reduces the wake's width, and correspondingly, the drag coefficient at higher angles of attack. However, vortex generators provide means of suppression at buffet conditions. The generators cause interactions between the shock and the vortices. Those interactions create a shift of the shock location downstream and inhibit the development of separated flow. The vortex generators also influence the frequency content of the aerodynamic coefficients. (Gianelis, Vio, and Levinski (2017))

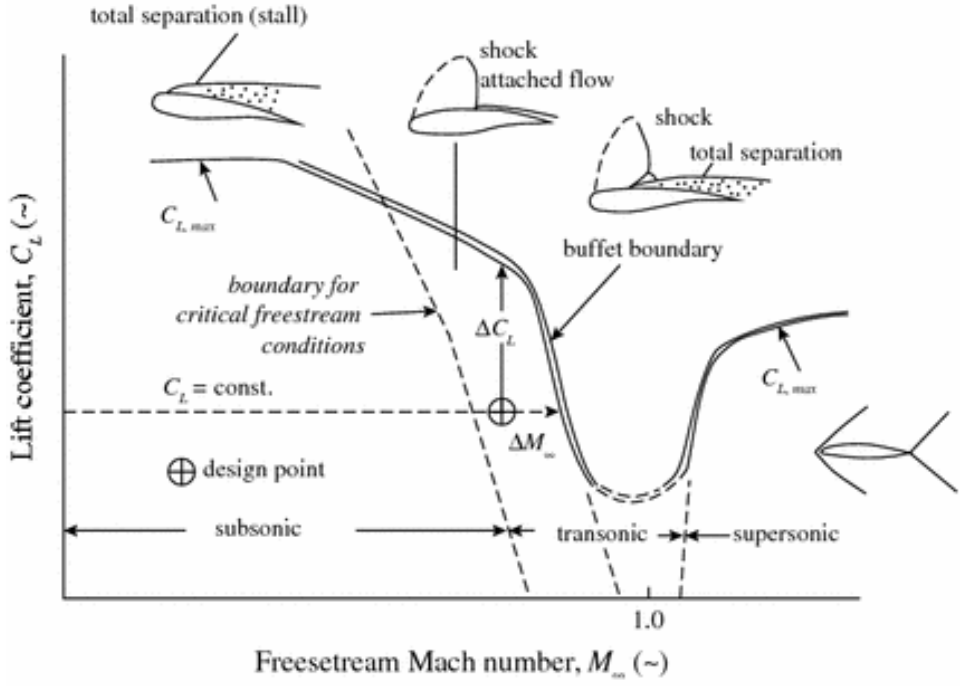


**Figure 2.7:** Separation boundary at different Mach numbers and lift coefficients. (Stanewsky and Basler (1989))

The third one is employing shock control bumps (SCB). SCBs provide a passive manner of controlling the shock by modulating the flow field close to the interaction between the shock with the boundary layer by reducing separation (Gianelis, Vio, and Levinski (2017)). The following section will discuss shock control bumps in more detail.

## 2.3. Supercritical Aerofoils

This section serves to present the workings of supercritical aerofoils. It first introduces the concept of a supercritical aerofoil. Then, this section dives into the working of the ONERA OAT15A supercritical aerofoil during buffet.

### 2.3.1. Supercritical Aerofoils

The design of supercritical aerofoils is to delay the rise of drag during transonic conditions. This delay is caused by changing how the flow above the upper surface behaves by flattening this surface. These aerofoils have an increase in overall aerodynamic performance during transonic flow. The flattening of the geometry ensures a weakening and a change in the location of the shock. Thus, the Mach numbers for the drag rise are higher than those of the conventional aerofoils because of the weaker shock which leads to a smaller separation (Whitcomb (1974)). Figure 2.8 shows the plot of a representation of the coordinates of an 11%-thick NASA supercritical aerofoil (Whitcomb (1974)). From the image, it is clear that the upper surface of the supercritical aerofoil remains quite flat throughout the chord length. The main goal of supercritical aerofoils is reducing the adverse effects of drag increase and their compromise in the lift. This goal is accomplished by tailoring the aerofoil geometry to avoid strong shock waves. (Sobieczky and Seebass (1984))

Supercritical aerofoils are of importance during transonic flow due to the phenomenon of transonic buffet. The geometry of the supercritical aerofoils causes a delay during transonic buffet. Therefore, using an aerofoil with a flatter upper surface causes the instability caused

**Figure 2.8:** Available coordinates for 11%-thick representative NASA supercritical aerofoil. The coordinates can be found in Whitcomb (1974).

by buffet to move to a higher critical Mach number. Setting both aerofoils side by side, it is concluded that due to the flatter upper surface of supercritical aerofoils, there is less "compression" of the flow above the aerofoil, which translates into a smoother pressure distribution throughout the chord leading to a shock further back of the aerofoil. (D'Aguanno, Schrijer, and Oudheusden (2019) and Gianelis, Vio, and Levinski (2017))

Figure 2.9 shows the main differences between a supercritical aerofoil from a conventional one. On the left, the image shows the flow above the aerofoils. When using the supercritical aerofoil, the supersonic region on the upper surface of the aerofoil takes up more of the chord. However, the shock wave is weaker. On the right, the image shows the typical pressure distributions. The pressure coefficient of the supercritical aerofoils tends to remain more constant throughout most of the chord. The pressure also drops more towards the trailing edge with a smaller jump in pressure. This smaller jump in pressure coefficient means that the shock wave weakens.

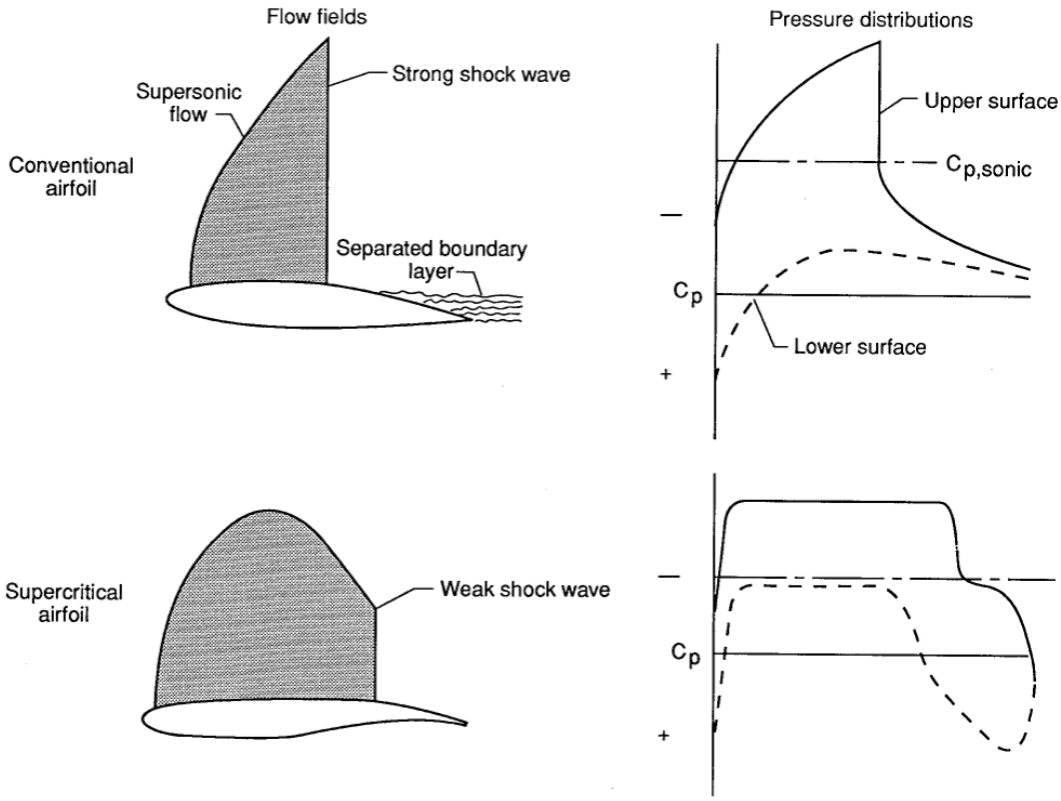


**Figure 2.9:** Comparison of a typical conventional aerofoil and typical supercritical aerofoil. (Harris (1990))

### 2.3.2. The OAT15A Aerofoil and buffet

The ONERA OAT15A aerofoil has been studied by different parties to look at the shock oscillations over the aerofoil. Through experimenting with the OAT15A in transonic conditions, the definition of the buffet onset conditions has been characterised. The experiments were done with the use of high-speed Schlieren and laser Doppler velocimetry with a primary goal to provide validation data to the computations using CFD. The experiments carried out suggest that the buffet phenomenon is mostly two-dimensional with some detected three-dimensional effects. (Jacquin, Molton, et al. (2009))

In experiments performed by Jacquin, Molton, et al. (2009), the data provided with information to help gain a deeper understanding of the buffet phenomenon. For executing the experiments, conditions such as the Mach number and the angles of incidence were manipulated. This handling ensured that the conditions leading to the transonic buffet were characterised. The tests led to results that showed consistent relations with the buffet process between the interaction of the shock motion and the boundary layer behaviour. The experiments also showed that the dynamics of this phenomenon are mostly two dimensional and periodic. However, there are three-dimensional patterns discovered in wall-flow visualisations.

D'Aguanno, Schrijer, and Oudheusden (2019) performed multiple experiments at the TU Delft on the OAT15A aerofoil. The purpose of the tests was to obtain a better understanding of the buffet phenomenon. In the experiments, Schlieren and Particle Image Velocimetry were used to investigate upstream travelling waves while experiencing buffet. During the test, the propagation velocity of the waves and their oscillatory frequency was determined. When performing the experiments, Schlieren ensured the proper detection of upstream travelling waves and their propagation velocity. From the research done on the OAT15A aerofoil, it was proved that the propagation velocity of the waves was not constant, but in fact, it is equal to the local speed of sound in the flow. During these experiments, they also demonstrated the relation between the shock wave and the separation area. Figure 2.10 shows the transonic feedback mechanism on the OAT15A.

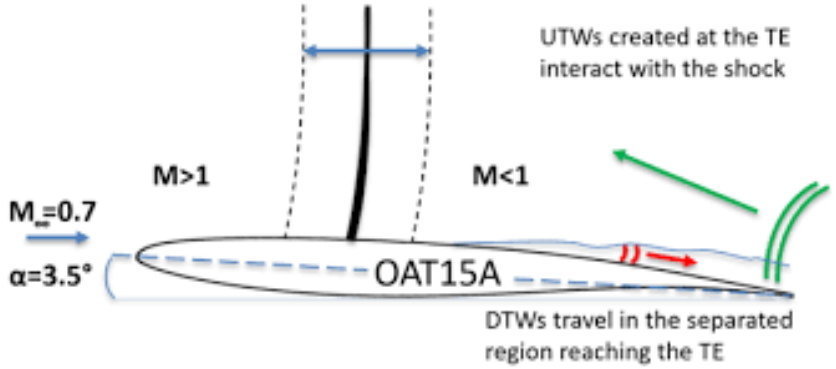


**Figure 2.10:** Sketch of the transonic feedback mechanism on the OAT15A aerofoil. (D'Aguanno, Schrijer, and Oudheusden (2019))

## 2.4. Shock Control Bumps

Research from numerical models shows that an increase in a shape similar to that of a bump decreases the amplitude of buffet and ensures that the structural frequencies of the vibration are separate from those of buffet (Raghunathan et al. (2008)). This data means that shock control bumps show improvement in the aerodynamic performance of transonic wings. It

has been demonstrated in the literature that they have the capacity for reducing drag and delaying the onset of buffet. The reason for the delay is the influence of certain flow conditions such as shock strength and position and post-shock pressure gradient. The principle of the shock control bump is shown in Figure 2.11. When one places the bump on top of the surface before the location of the main shock's occurrence, a weaker shock is created, which slightly decelerates the flow. Thus, the shock control bump improves the flow behaviour by splitting the main shock into multiple weaker oblique shocks or compression waves. In conclusion, by placing a SCB on the surface of the aerofoil, the flow decelerates more gradually than with a single uncontrolled shock wave which in return reduces the stagnation pressure and the drag. (Bruce and Colliss (2014))

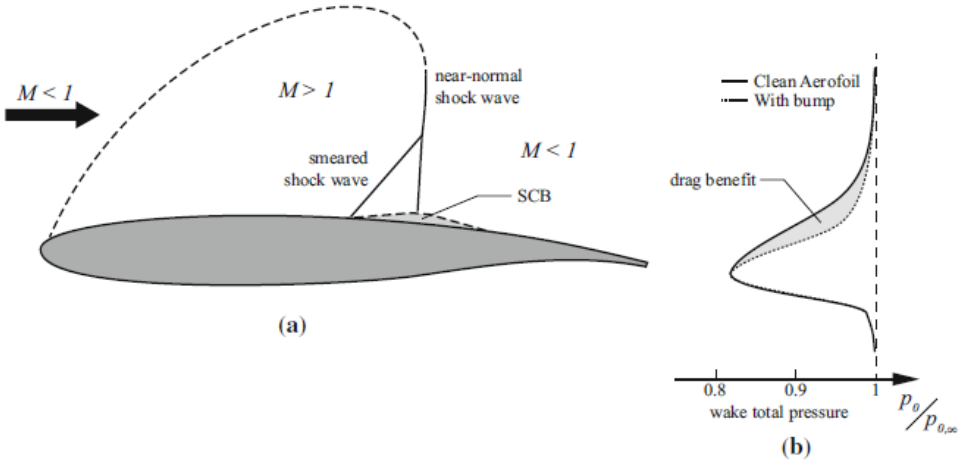


**Figure 2.11:** Principle of a shock control bump device on a supercritical wing. (a) shows the transonic flow over the wing with the shock control bump. (b) shows the total pressure in the wake. (Bruce and Colliss (2014))

### 2.4.1. Geometry

The geometry of the shock control bumps has a blunt triangular shape resembling a bump. Its shape consists of a ramp, followed by a crest and tail. This bump is placed on the top of the surface before one expects the shock to occur. So, the bump's location is on the upper surface of an aerofoil, where it is expected to experience transonic flow. The SCBs placed on the surface of the wing will split the shock wave into multiple weaker shocks, which ensures for the flow to decelerate more gradually, causing lower drag and a reduction in the stagnation pressure loss, as seen in Figure 2.11. Typically, a shock control bump is located upstream of the nominal shock location. The purpose of the ramp in the geometry is to generate an oblique shock before the main shock wave, which intends to deflect the incoming supersonic flow away from the surface. The crest region serves to decelerate the flow to subsonic speeds through a near-normal shock wave that is generated at said location. Finally, the tail aims to bring the flow behind the shock back to the surface of the aerofoil. Figure 2.12 shows how a slight change in geometry can have a different effect on the weaker shocks generated by it. The image also shows how a smoothly contoured bump creates compression waves in front of the shock, while a bump with a wedge structure creates the main shock with two shock "legs". They both serve to improve the aerodynamic performance of the wing. However, the exact manner they do so is slightly different. (Bruce and Colliss (2014))

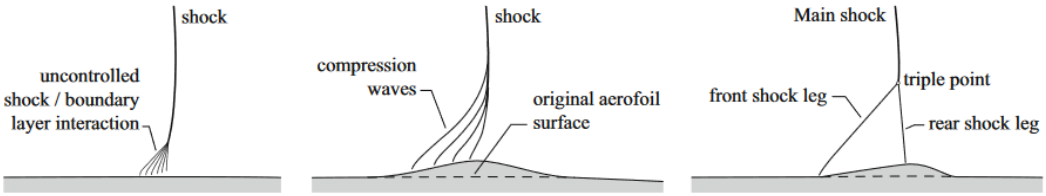


**Figure 2.12:** Effect of shock control bumps on the shock structure:(a) no-control case ;(b) compression waves produced by a smoothly contoured bump Birkemeyer, Rosemann, and Stanewsky (2000); (c) shock structure produced by a wedge bump Ogawa et al. (2008). Bruce and Colliss (2014)

### 2.4.2. Flow around Shock Control Bumps

The flow passing through the shock control bumps is sensitive to the shock position and the state of the incoming boundary layer. The flow characteristics of SCBs need to be understood in different operating conditions to account for the sensitivity of the flow passing around the bumps. Research has considered mostly cases with a bump that has a height of the same order as that of the local boundary layer thickness and with a shock strength close to Mach 1.3. (Bruce and Colliss (2014))

#### Two Dimensional Shock Control Bumps

A 2D shock control bump produces a flow that resembles the one shown in Figure 2.12. Ashill and Fulker (1992) studied the performance of 2D SCBs. The experiments showed that when the shock position was not at its optimum location, expansions and secondary shock systems appeared. These expansions and shock systems resulted detrimental to the performance of the shock control bumps. Figure 2.13 illustrates how the shock position impacts the flow structure over a 2D SCB. The expansions and shock waves from Figure 2.13 impose strong pressure gradients on the boundary layer, which happen on the surface of the shock control bump. How the boundary layer behaves determines the performance of the 2D shock control bump. A well-designed 2D SCB is of great importance in keeping its impact on the health of the boundary layer as small as possible, compared to a case where the shock position is closer to optimal. Furthermore, shock locations that are not optimal can allow for an increase of the viscous drag and can promote separation of the boundary layer. However, in conclusion from studies, two-dimensional SCBs have shown a positive impact because of their ability to delay the buffet onset in transonic flow and improve shock stability. (Bruce and Colliss (2014))

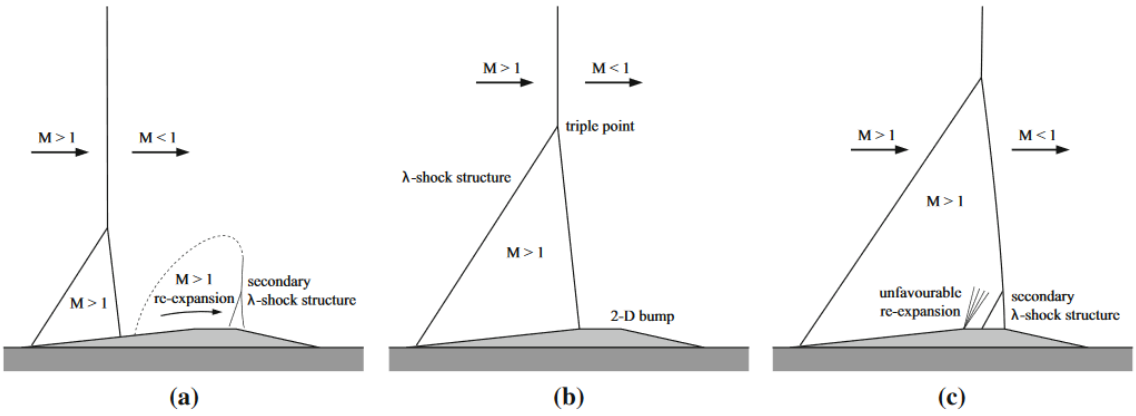


**Figure 2.13:** Effect of the position of the shock on SCB flow structureOgawa et al. (2008): (a) shock upstream of the optimum location; (b) at the optimum location; (c) downstream of the optimum location. (Bruce and Colliss (2014))

**Three Dimensional Shock Control Bumps**

The physics of the flow around a 3D shock control bumps is different from that of a 2D SBC in multiple ways. The three-dimensional SCBs create a shock structure that goes along their central axis. However, this shock formation decays spanwise. Thus, a three-dimensional shock control bump produces a curved shock front such a shock front is shown in Figure 2.14 (a). Ogawa et al. (2008) studied this decay and observed that the shock front decay is gradual, which means that with the proper arrangement of the SCBs, a quasi 2D shock control bump can be created, as illustrated in Figure 2.14 (c). Figure 2.14 (a) highlights the variation in the thickness of the boundary layer downstream of the SCB. This situation is complex due to the SCB introduction of vorticity. Similarly, as with the 2D shock control bumps, the secondary shock structures that appear and the flow re-acceleration can be detrimental in terms of the drag and the health of the boundary layer. (Bruce and Colliss (2014))

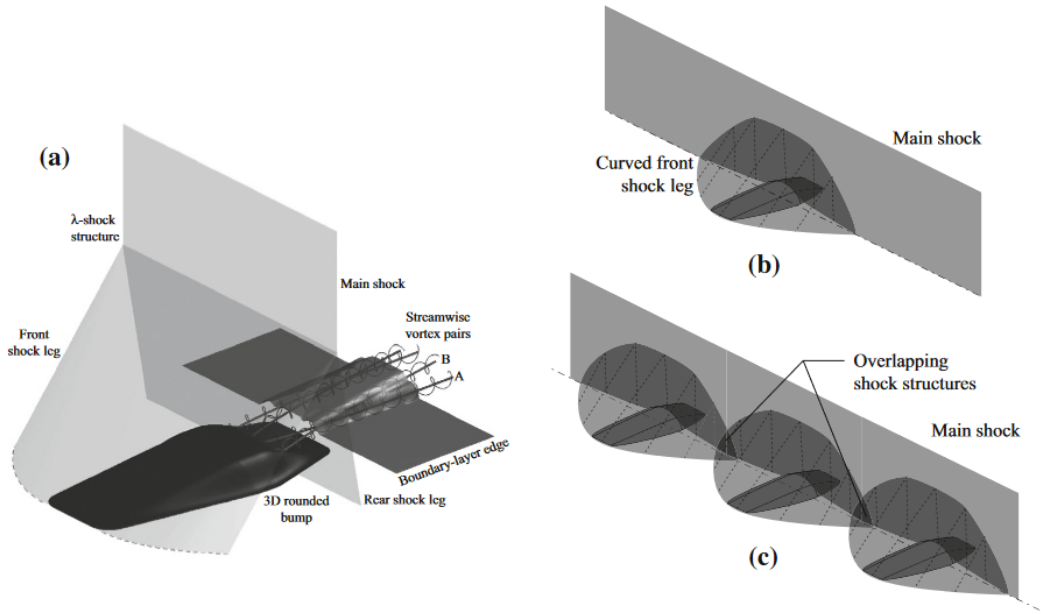


**Figure 2.14:** Shock structure produced by 3D shock control bumps: (a) shock structure proposed by Ogawa et al. (2008); (b) spanwise influence of a single 3D SCB; (c) 3D SCB array. (Bruce and Colliss (2014))

### 2.4.3. Performance

For assessing the performance of shock control bumps, one looks at the lift-to-drag ratio and the boundaries. The first assessment of performance is the drag since this affects the lift-to-drag ratio. There is a balance between a reduction in wave drag and a decrease in lift due to viscosity in the SCBs' performance. Research has shown that SCBs can have an overall positive effect on the lift-to-drag ratio of aerofoils in transonic conditions. SCBs show an increase in the aerodynamic performance of the wing. Specifically, high values for the lift coefficient are achieved by supercritical aerofoils or wings. The reason for this benefit is the fact that shock control bumps have a positive impact on the presence of a shock wave that is relatively strong. (Milholen and Owens (2005) and Bruce and Colliss (2014))

The second assessment of performance is off-design. This evaluation came to exist from investigations into methods for increasing the Mach number of the drag-divergence of transonic aerofoils (Tai (1977)). Ogawa et al. (2008) have also performed studies on the 'robustness' of SCBs by experimenting with them at off-design conditions. These settings were close to the conditions experienced during cruise, as well as for the design conditions. König et al.

(2009) conducted numerical studies. From their research, the importance of the SCB geometry was highlighted by its performance. In the studies, they reported that smoothly contoured SCBs provide optimal drag reduction. This decrease in drag occurs at the design point of the shock. However, the more angular the device is, the higher the 'robustness' that it provides for variation in the position of the shock, with only a small loss in its efficiency. Furthermore, variations in the position of the shock can cause vortical structures and separations in the flow, which can impact the performance of the wing during off-design conditions (Ogawa et al. (2008)). (Bruce and Colliss (2014))

### 2.4.4. Shock Control Bumps During Transonic buffet

Both two-dimensional and three-dimensional shock control bumps need to be discussed separately. These analyses will focus on the SCBs' performance in transonic flow. The reason for the separation is that they have different behaviour. The primary cause is the extra dimension that can generate vortices in the downstream flow.

#### Two Dimensional Shock Control Bumps

Birkemeyer, Rosemann, and Stanewsky (2000) provided observations of the impact of shock control bumps on the separation and pressure fluctuation at the trailing edge of a wing. In the remarks, Birkemeyer, Rosemann, and Stanewsky (2000) mentioned that 2D SCBs postpone the onset of buffet to higher lift coefficients. For achieving these observations, they ran experiments and RANS computations. The goal behind the tests was to show that a SCB placed downstream of the main shock would have a positive effect on the pressure fluctuations and separation when approaching the buffet boundary. These conclusions are in agreement with observations from Ashill and Fulker (1992), where they concluded that 2D shock control bumps could provide a delay to the onset of the transonic buffet by introducing attached flow in between the trailing edge and the shock wave, which postpones the flow breakdown.

#### Three Dimensional Shock Control Bumps

From research on both 2D and 3D SCBs of the flow over an unswept wing in transonic conditions from Eastwood and Jarrett (2012), the conditions at which the two regions experiencing separation would coincide, which causes fully reversed flow ranging from the shock to the trailing edge. With the results, the impact that the SCBs have on the characteristics of buffet, as well as the lift-to-drag ratio, were studied. There are two major conclusions from this research. The first one is that 3D shock control bumps show great potential to postpone the onset of buffet, even when they are close to the position of the shock, unlike 2D SCBs. The second is that 3D SCBs can improve the buffet margin. However, there is a penalty for achieving peak aerodynamic performance.

### 2.4.5. Supercritical Aerofoil with Shock Control Bumps in Transonic Flow

Messina (2020) wrote his MSc thesis on the investigation of the reduction of the detrimental effects of the buffet onset through the use of shock control bumps. The aerofoil used for the experiments was the OAT15A supercritical airfoil. The tests took place at the TST-27 wind tunnel of the TU Delft. The results of his work led to the validation of using SCBs due to their usefulness in reducing the energy that is associated with the oscillation of the shock wave. Figure 2.15 shows the results he obtained from comparing the shock wave oscillation between the clean aerofoil and the aerofoil with eight shock control bumps. Figure 2.15 demonstrates that by using SCBs the intensity region decreases. Figure 2.16 shows the results with ten shock control bumps. The image shows a difference between both figures, the image with the ten SCBs has a region of high intensity smaller than the image with eight SCBs. However, the

location behind the high-intensity region for the case with ten SCBs has a higher intensity than that of the case with eight SCBs, which is mostly because the total shock region experienced by the flow is weaker when using ten SCBs. The results also showed a decrease in the position range of the shock wave oscillation when using SCBs, as seen in Figure 2.17. Comparing Figures 2.15 and 2.16, leads to some similarities with the discussion about two- and three-dimensional shock control bumps. When the quantity of shock control bumps increased, the experiments showed a result resembling those of a quasi-2D shock control bump, which causes a lower pressure gradient after the shock.

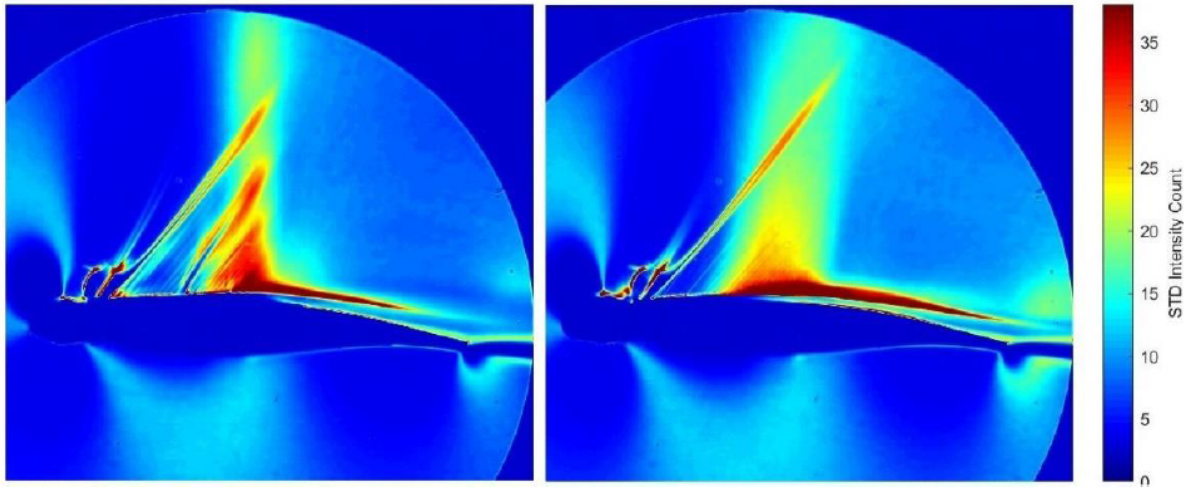


**Figure 2.15:** Comparison of the shock wave oscillation between the test with eight shock control bumps and the clean aerofoil. (Messina (2020))

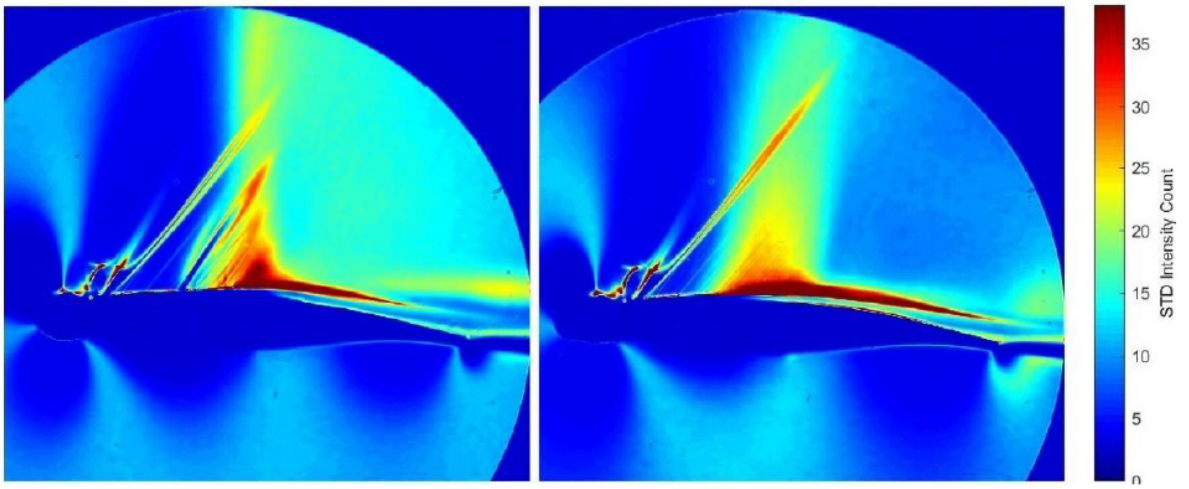


**Figure 2.16:** Comparison of the shock wave oscillation between the test with ten shock control bumps and the clean aerofoil. (Messina (2020))

Yun et al. (2017) looked at the performance of shock control bumps on the RAE2822 supercritical aerofoil using RANS and URANS. In their research Yun et al. (2017) considered two different types of SCBs' configurations, the first being forward-mounted shock control bumps and the second being backwards-mounted. The two arrangements had the purpose of how a SCB mounted more rearwards from its ideal position would also have the same positive

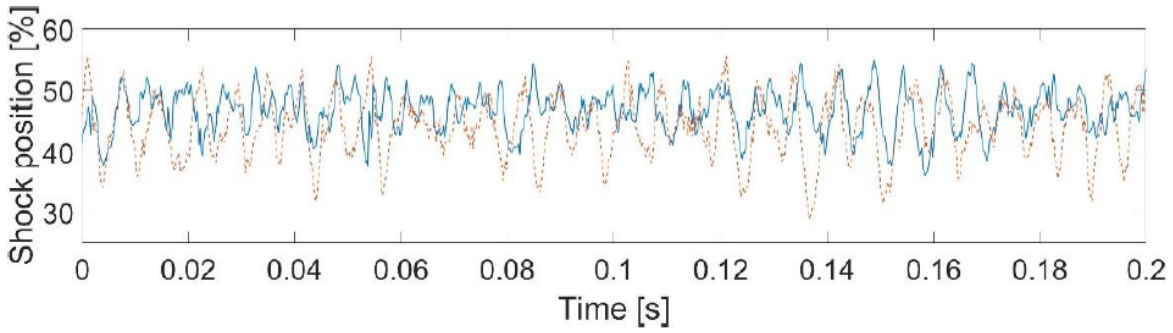


**Figure 2.17:** Comparison of the oscillation of the shock wave position between the test with 10 shock control bumps in blue and the clean aerofoil in red. The shock position is given as a percentage of the chord location. (Messina (2020))

effects as one mounted in its optimal position or slightly forward. The first configuration, with the SCBs, mounted more towards the front of the aerofoil, proved to reduce the shock's strength at a variety of buffet conditions at the design point. The second SCBs configuration, with the SCBs backwards-mounted, showed alleviation of the adverse pressure gradient at off-design conditions, where a second shock wave may occur. The second shock intensifies the adverse pressure gradient. Therefore, it also strengthens the main shock. It was noticed that the SCBs' configuration mounted more towards the trailing edge flattened the leeward part of the aerofoil, which means that the upper surface is flattened in the same manner that a supercritical aerofoil, whose design consists of a flatter surface. By these means, the shock wave weakens.

# 3

# Pressure Sensitive Paint

Pressure sensitive paint works as an optical sensor for helping determine the surface pressure of models in aerodynamic facilities, such as wind tunnels. One of the main advantages of the PSP technique is its non-intrusive nature. The two main working principles behind PSP are oxygen quenching and photo-luminescence. The photo-luminescence principle works by using UV light to excite the luminophores in the paint. These paint molecules react with the UV photons and the oxygen content in the environment. Therefore, the more oxygen available, the less the paint reacts with the UV. When the UV excites the paint molecules, they emit a photon which is a different wavelength than the excited one, which means that the more oxygen there is, the less intense the emission will be. The paint works under the assumption, that the oxygen in the environment corresponds to the pressure level. (Liu and Sullivan (2005))

## 3.1. Pressure sensitive Paint and Photon Emission

The purpose of this section is to explain the principle driving the working of pressure sensitive paint as a flow measurement technique. The luminescence process of oxygen quenching is the basic principle responsible for the working of PSP. Oxygen quenching is a reversible process in molecular photoluminescence. The molecular photoluminescence process means that each luminophore (the paint dye molecule) absorbs a photon. By this luminophore absorbing a photon, an electron in the molecule is excited. This excitation brings the luminophore into a higher energy state. Once the molecule is excited, it releases the excess energy by radiating a photon. This photon radiation serves to bring the luminophore into a lower energy state. However, there is another way for the luminophore to experience a reaction. This other reaction is with the oxygen present in the environment. This reaction is best known as oxygen quenching. Therefore, depending on the local pressure that the luminophores experience, a different luminescence is emitted. Due to oxygen quenching, the luminescence intensity decreases with increasing air pressure. The Stern-Volmer Equation (3.1) describes the relationship between the luminescent photograph intensity and oxygen. In the equation, $\frac{I_0}{I}$ is the measured intensity to background intensity ratio, $k_Q$ is the oxygen quenching decay rate, $k_P$ is the photon emission decay rate, and $k_D$ is for all other deactivation terms. (Liu and Sullivan (2005), Mantel (2005), and Schanze et al. (1997))

$$\frac{I_0}{I} = 1 + \frac{k_Q[P]}{k_P + k_D} \tag{3.1}$$

### 3.1.1. Kinetics of Luminescence

The kinetics of luminescence can be best understood utilizing the Jablonsky energy-level diagram. Figure 3.1 shows the diagram. The goal of the diagram is to illustrate the electronic states of the molecules and their energy transitions. In the diagram, the lowest horizontal line represents the ground-state energy of the molecule, the singlet state $S_0$. Through the absorption of photon radiation, the luminophore can be excited from the ground state to either the $S_1$ or $S_2$ electronic state. Due to both radiative and radiationless processes, the excited electron can go to a lower state. The change in energy state through light emission occurs through the radiative process of luminescence. And for the transition from the lowest singlet state to the ground state is fluorescence. (Liu and Sullivan (2005))

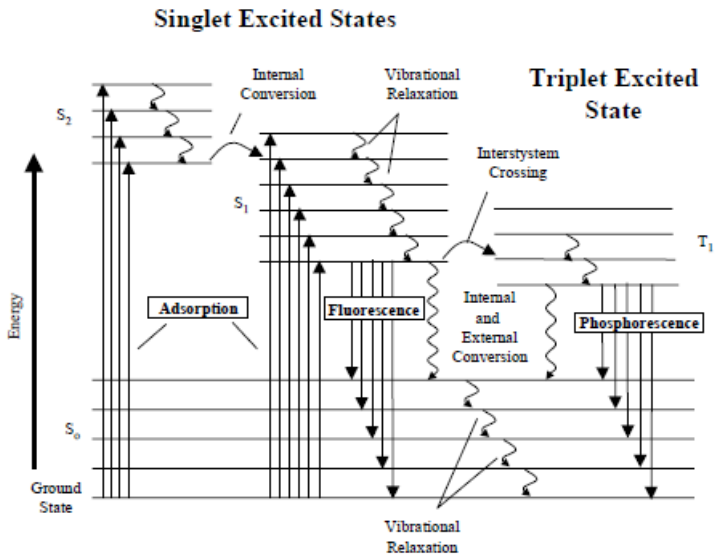


**Figure 3.1:** Jablonsky energy-level diagram.Liu and Sullivan (2005)

When the excited molecules interact with the rest of the components of the system, the excited singlet and triplet states are deactivated. The processes are known as quenching processes, with oxygen quenching being the leading photophysical mechanism for PSP. Thus, the air pressure on the model is determined by the Stern-Volmer equation using the luminescent intensity. However, if an increase in temperature takes place, the efficiency of the paint decreases. (Liu and Sullivan (2005))

### 3.1.2. Excitation

Excitation of the luminophores in PSP is crucial for measuring the surface pressure with this technique. For the excitation, a light source with a specific wavelength is necessary. This explicit wavelength is essential because the luminophores are sensitive to a wavelength range. The typical wavelengths of excitation light range from 300nm to 500nm, from UV to green. The reason for this is that each PSP configuration needs a different amount of energy for electron excitation. The excitation energy of the photon is shown by Equation (3.2), where c is the speed of light in [m/s], h is Planck's constant in [Js], and $\lambda$ is the excitation wavelength in [m]. (Liu and Sullivan (2005))

$$E_{photon} = \frac{hc}{\lambda} \tag{3.2}$$

The energy of the excited state is lower than that of the photon. This difference in the amount of energy is due to the energy loss that happens when changing forms. Once a dye molecule has reached an excited energy state, it can be excited into a higher state. However, at each energy state, the optimal wavelength to excite the photon will be different. (Liu and Sullivan (2005))

### 3.1.3. Photon Emission

Once a dye molecule has been excited, that molecule can emit a photon to release its energy. However, this photon's energy will be lower than the energy needed to excite the dye. This difference in energy between the excitation and emission energy is known as the Stokes' shift. One cause for the energy reduction is the necessary activation energy for going from one state to a higher one, as seen in Figure 3.1. After excitation, the energy of the reached state will be higher than the minimal energy of the said state. The cause of the actual energy being higher than the state's energy is that the molecule is now in a vibrational state. So the following incident consists of the molecule losing energy through vibrational relaxation. When this occurs, the molecule emits a photon decreasing its internal energy even further. After photon emission, the molecule goes to the ground state with a higher vibrational state. (Bell et al. (2001) and Mantel (2005))

The wavelength of the photon emission is different from that of photon excitation. The difference in wavelengths forms an advantage when performing experiments with pressure sensitive paint. Photon emission is luminescent behaviour. Meanwhile, fluorescence happens if the excited state is a singlet state. However, if the excited state is a triplet, the emission is known as phosphorescence. Chemical reactions, such as oxygen quenching, also cause luminescence to occur. (Liu and Sullivan (2005))

### 3.1.4. Oxygen Quenching

The main principle in the working of PSP is the principle of oxygen quenching. Oxygen quenching is a chemical reaction between the luminophore and the oxygen in the environment. The best way to explain this process is by having a model in a wind tunnel. Inside the wind tunnel, the model experiences a different pressure depending on which area of the model is measured. It is clear that the higher the air pressure, thus the local pressure, on the model, the more oxygen there is at that location. Therefore, the more oxygen present at a place on the model, the more oxygen quenching will occur. The reaction with oxygen also serves to relax the luminophores in the paint. When the equilibrium between excitation and relaxation exists, the more dominant oxygen quenching becomes for increasing pressure. Because oxygen quenching is the dominant principle, the less intense the photon emission from the paint is. Therefore, the decay of the paint dye molecule decreases with higher pressure. (Liu and Sullivan (2005))

Oxygen quenching occurs when an excited molecule loses its energy by exchanging it with one triplet oxygen. So the luminophore ends up in the ground state, and the oxygen is excited into a singlet state. The oxygen will also lose energy and reach the ground state. (Liu and Sullivan (2005))

For the principle to work, an initial photoexcitation places a luminophore, X, in an excited state, $X^*$ with a finite lifetime, as seen in Equation (3.3). (Gouterman (1997))

$$X + hv_{ex} \rightarrow X^* + heat \tag{3.3}$$

Once the luminophore is in an excited state, there are two main ways how the luminophore will behave. The first manner is shown in Equation (3.4), $X^*$ emits a photon and then returns

to the ground state, and the second in Equation (3.5), $X^*$ returns to the ground state without radiating. (**textOxygenQuenching_article**)

$$X^* \rightarrow X + hv_{em}(rate \;\; k_p) \tag{3.4}$$

$$X^* \rightarrow X + heat(rate \;\; k_n) \tag{3.5}$$

However, in the wind tunnel, another reaction path is required, this path is shown in Equation (3.6). This equation means that when a higher concentration of oxygen is present, the lifetime of the luminophore is reduced. Equation (3.6) competes with Equations (3.3) and (3.4) for the depopulation of the excited state. (Gouterman (1997))

$$X^* + {}^3O_2 \rightarrow X + {}^1O_2 + heat(rate \;\; k_q[O_2]) \tag{3.6}$$

Diatomic oxygen has two degenerate highest occupied molecular orbitals containing one electron each. The lowest energy state contains one electron in each orbital, both electrons spin in parallel. This is known as a triplet state, ${}^3O_2$, shown in Figure 3.2 (a).The two electrons can also form singlet states by having antiparallel spin, Figure 3.2 (b), or by being in the same orbital with an antiparallel spin, Figure 3.2 (c), these states are denoted as ${}^1O_2$. (Gouterman (1997))

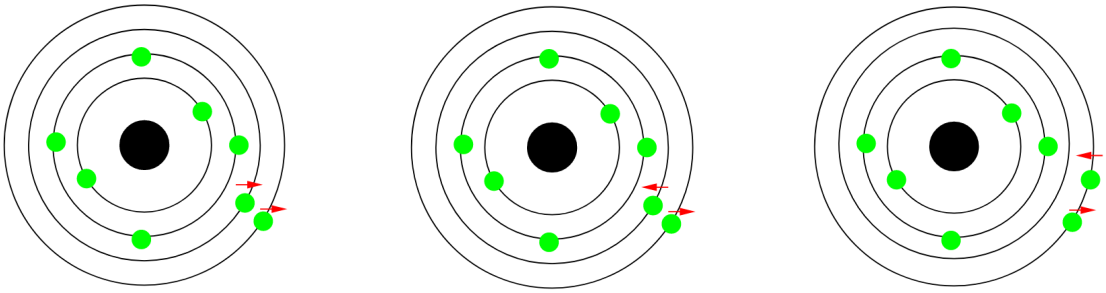

**Figure 3.2:** (a) Triplet state (b) singlet state 1 (c) singlet state 2

The oxygen state ${}^1O_2$ is more reactive than ${}^3O_2$. Therefore, ${}^1O_2$ is a complication when using PSP in the wind tunnel. (Gouterman (1997))

## 3.2. Intensity versus Decay

The section's goal is to give an overview of the two main types of PSP measurement systems, intensity-based and lifetime-based, and compare them.

### Intensity-Based Measurement Systems

The paint for performing the intensity method consists of two luminescent dyes, and two different luminophores ensuring that the experiments have multiple pros. The effects caused by mole concentration, paint thickness, and spatial variations in illumination are no longer a problem. The reason that these effects are not an issue is that there are two signals measured. Each of the two types of luminescent molecules emits a different wavelength, thus signal. Therefore, taking both signals causes compensation for errors. This error compensation occurs by taking the ratio between the wind-on and wind-off images to eliminate said effects. For the calibration of PSP, a correction of the temperature effect needs to occur. That way, the pressure is accurately computed from the luminescent intensity. (Jahanmiri (2011) and Liu and Sullivan (2005))

**Lifetime-Based Measurement Techniques**
The lifetime-based measurement technique is also known as the decay-based measurement technique. This PSP method has other advantages than the intensity one. This method aims to diminish the dependence that the pressure and the luminescent lifetime have on the illumination intensity. Theoretically speaking, the lifetime-based approach is insensitive to multiple variables. These variables are the luminophore concentration, photodegradation, paint thickness and contamination. The insensitivity of the method is due to the use of a pulsed light source. The pulsing in the light ensures an intensity degradation of the emitted luminescence in between pulses. By measuring the emitted luminescence in between pulses, one obtains the decay rate. This decay rate of luminescence is related to the air pressure. (Liu and Sullivan (2005))

**Comparison**
Both intensity- and lifetime-based PSP can be used for multiple applications because PSP offers quantitative pressure measurements and initial boundary conditions necessary for numerical flow simulations. Moreover, the composition of both is different because the paint for decay systems consists of one dye. Meanwhile, the composition of the paint for the intensity systems method consists of two dyes. Therefore, the intensity methods require that both dyes are measured and correlated, and a homogeneous light source is needed. Decay methods can measure pressure and temperature at the same time. However, they require a pulsed light source. (Engler, Klein, and Trinks (2000))

## 3.3. Experimental Setup of pressure sensitive Paint

The basic experimental application and setup of pressure sensitive paint are the same for the different methods. However, slight variations do occur. Multiple pieces of equipment are generally required. Figure 3.3 shows the general equipment to carry out the experiments. The most obvious is the model covered in PSP. For the paint to work, illumination light is necessary. The illumination light needs to emit the correct wavelength to excite the luminophores. A CCD camera records the emitted illumination. Because the camera tends to record in back and white, a filter in front of the lens is applied. The output of the camera is calibrated for the temperature and pressure before the experiments. The purpose of this filter is to filter out all other wavelengths that are not the ones emitted. The camera connects to a computer for saving and analysing the images.

Figure 3.4 shows a general image of the photon excitation and emission. In this image, it is clear that the excitation light can consist of different components. The three most common in the picture are UV lamps, LEDs and lasers. This light source shoots to the luminescent molecule, and the molecule emits a photon. The photon passes through an optical filter. As previously discussed, this filters the nondesirable wavelengths. Behind the filter, there is a detector. The detector captures the photons that passed through the filter. The most common are photomultiplier tubes, charge-coupled devices and partial discharge detectors.

## 3.4. Pressure Sensitive Paint in Transonic Flows

The usage of PSP for transonic testing appeared after the method was already proven successful in subsonic and supersonic flows. Vardaki et al. (2010) studied how the behaviour of PSP in transonic flows compares to that of other more conventional measurement techniques, such as electronically scanned pressure taps. The PSP method for the experiments was the lifetime approach with in-situ calibration, where the larger source error comes from the temperature changes. The study showed PSP to be successful as a technique to be used in the transonic

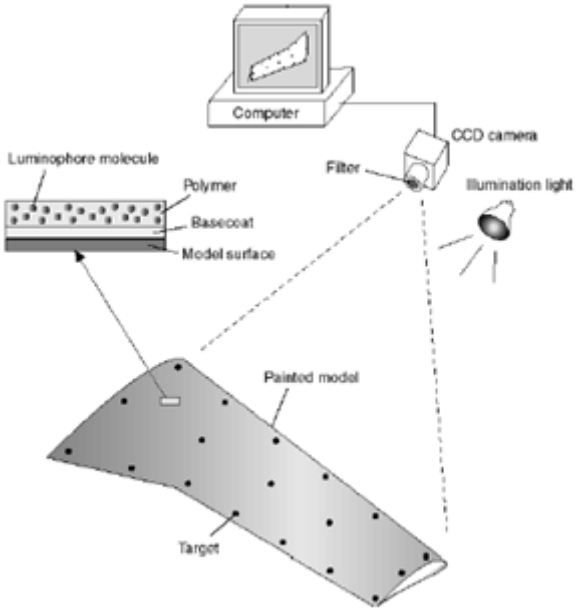


**Figure 3.3:** Illustration of a typical PSP experiment setup. Liu and Sullivan (2005)

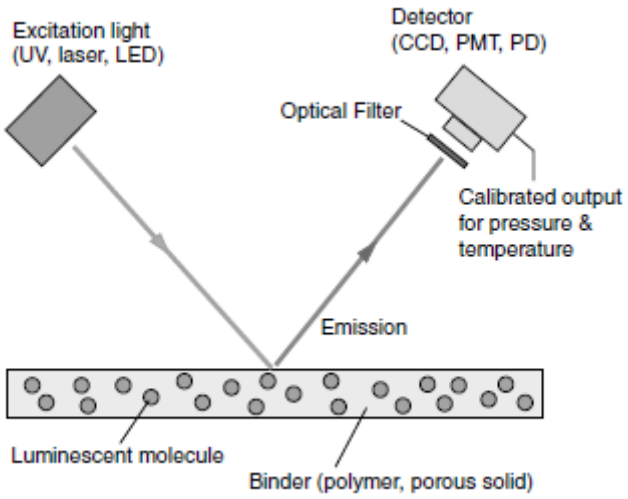


**Figure 3.4:** Basic illustration of PSP physics. Liu and Sullivan (2005)

regime with an uncertainty of 700Pa or less after doing temperature correction. Figure 3.5 shows the pressure contours obtained with the PSP experiments at two different angles of attack. The values provided in the contours match the data from the pressure taps on the presented upper surface of the wing.

Later, fast-responding paints started to be manufactured for unsteady flows. Merienne et al. (2013) used anodized aluminium instead of the usual PSP. A thin layer of aluminium oxide can be created on the surface by the anodising of aluminium. Anodised Aluminium has high porosity that is uniformly distributed on the surface increasing its sensitivity to oxygen (Liu and Sullivan (2005)). The results from Merienne et al. (2013) using AA-PSP allow us to see

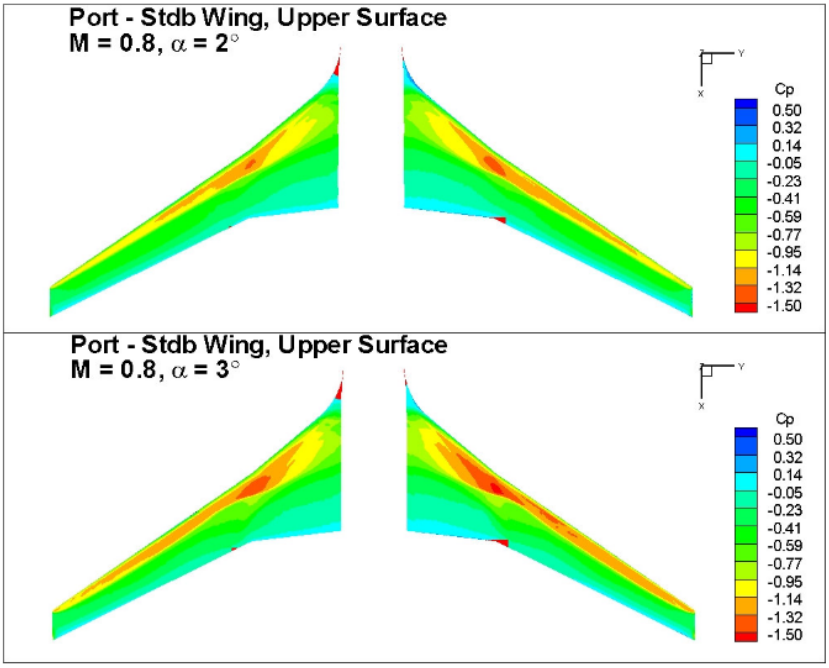


**Figure 3.5:** Wings of the ARA reference model set at an incidence of $\alpha$=2$^o$ and $\alpha$=3$^o$ at M=0.8 Vardaki et al. (2010)

the shape and position of the shock wave on the lower wall channel where an anodized insert covered in PSP was placed. The oscillation of the shock can be seen in Figure 3.6

## 3.5. Chapter Recap

The purpose of this chapter was to introduce the reader to the pressure sensitive paint technique. After the introduction to the topic, the chapter aimed to explain the principles behind this technique. The two most common methods, intensity and lifetime, were presented. The last two chapters informed on the most common types of paint and the general setup for experiments.

Pressure sensitive paint is a non-intrusive method that can measure an entire surface. It consists of dye molecules in paint that are excited by a light source. These molecules emit a photon when excited. The paint excitation photons and the emitted ones are of different wavelengths. Furthermore, the intensity of the images recorded is dependent on the pressure in the environment.

The main conclusion from this chapter is that the recorded intensity decreases with an increase in pressure. The reason for this intensity-pressure dynamic is the principle of oxygen quenching. During this process, the luminophore in the paint reacts with the oxygen in the environment. Therefore, there are fewer luminophores available to be excited by the light source.

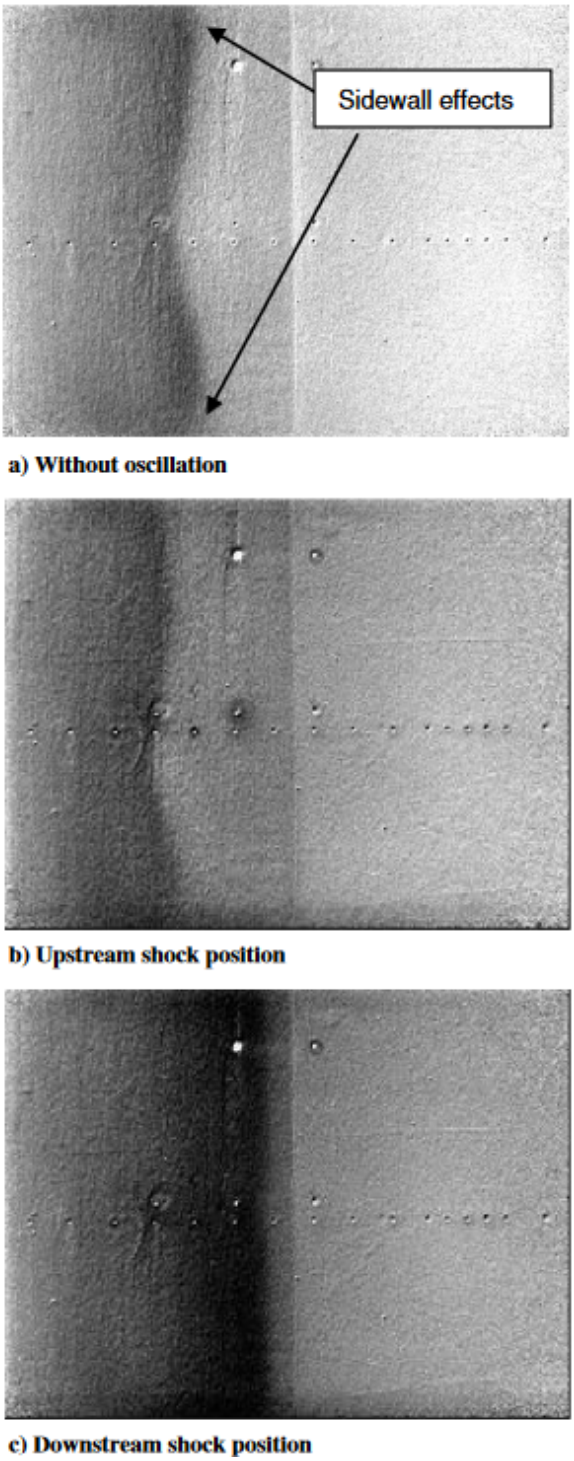


**Figure 3.6:** PSP images a) without, b-c) with oscillation. (Merienne et al. (2013))

# 4

# Methodology and Experimental Setup

This chapter aims to provide the reader with the necessary steps for performing the experiments of the OAT15A supercritical airfoil in the TST-27 wind tunnel of the TU Delft using PSP as a flow measurement technique. The chapter starts by reintroducing the research objectives, followed by the steps and the experimental setup needed.

## 4.1. Open Points for Research and Formulation of the Objectives

The purpose of this section is to reestablish what the research objectives are. The main aim is to **apply pressure sensitive paint to measure the average pressure distribution in a transonic wind tunnel to study the effect of shock control bumps on a supercritical airfoil during buffet**, by achieving the following:

1. To use pressure sensitive paint for the first time at the TU Delft and determine if it can provide the department with any additional information.
2. To determine the effect of the shock control bumps on the surface pressure of the OAT15A supercritical aerofoil using pressure sensitive paint.
3. To determine the average pressure and lift coefficients of the OAT15A supercritical aerofoil with and without shock control bumps during the transonic regime.

By the end of the experiments and data analysis, the following question will be answered: **Is it possible to obtain the average pressure and lift coefficients of the OAT15A supercritical airfoil with and without shock control bumps during buffet with the use of pressure sensitive paint?**

## 4.2. Methodology

The purpose of this section is to provide the reader with the required methodology for the experiments. This section first presents the general methods for all of the experiments. The following subsections provide more information on the specific approaches for the three different sets of experiments, the verification/calibration, the validation and the main experiments.

### 4.2.1. PSP Lifetime-Based Methodology

For the experiments, the PSP lifetime approach is used. The lifetime approach consists of computing the time it takes the paint luminophores to dye out. As previously mentioned, the

luminophores react with both the oxygen and the UV photons. With this approach the UV excitation remains the same; however, the oxygen molecules change depending on the pressure. Thus, a higher pressure leads to fewer photons emitted by the luminophores. This also means that for the two distinct capture windows, the regions with a higher surface pressure will experience a higher relative drop in measured intensity, see Figure 4.1. What this means is that from each PSP measurement, there will be an intensity ratio between both camera window captures depending on the region. Thus $\frac{I_1}{I_2}$ for a higher pressure is larger than $\frac{I_1}{I_2}$ for a lower pressure at the same temperature. Then with the intensity ratios, the lifetime of the paint can be computed according to Equation (4.1).

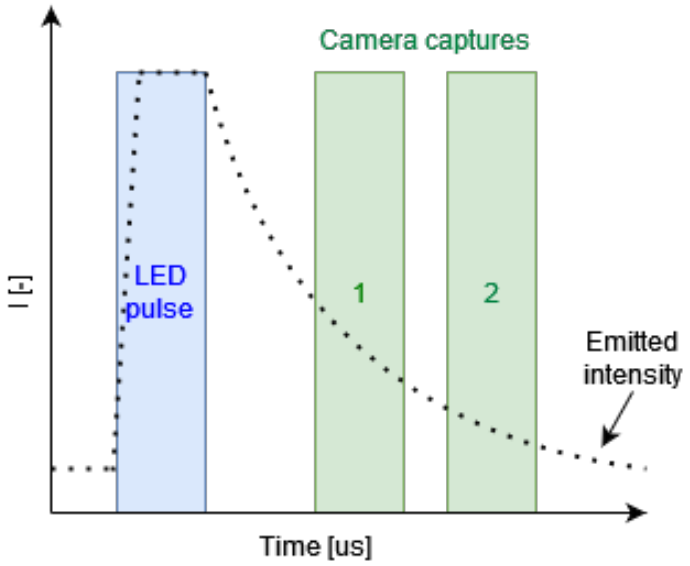


**Figure 4.1:** Schematic plot of the emitted intensity from the photons when being exited by the LED lamps and when the camera exposures would need to occur. The blue represents the LED light pulse and the green columns represent the first and second acquisition windows. All of the pulses are in the order of microseconds.

$$\tau = \frac{-\mathrm{d}t}{\ln\left(\frac{I_2}{I_1}\right)} \tag{4.1}$$

For actual PSP measurements, a reference pressure is used to compute the reference lifetime. The reference pressure and lifetime are used for determining the pressure in wind tunnel experiments as presented in Equation (4.2). The equation is also dependent on the surface temperature as the lifetime of the luminophores decreases as the temperature increases.

$$\frac{\tau_0}{\tau} = A(T) + B(T)\frac{P}{P_0} \tag{4.2}$$

The theory from the previous paragraphs can be accomplished by a UV light source that periodically gives a light pulse to excite the luminophores. Parallel to this, a camera also periodically experiences two capture windows after the UV light pulse; these windows do not happen at the same time but one is a few microseconds after the first one. Both the UV LED light source and the camera experience their respective trigger at the same frequency.

**Pressure sensitive measurement**

A PSP measurement consists of three image capture windows, which are the background image without any excitation. Then there is the first window for data gathering which occurs

after the LED lamp's pulse is finished. After the first capture window is done and some time has passed, the second capture starts. Figure 4.1 shows a schematic of the location of the first and second capture images in time. To account for noisy images, each capture set is repeated multiple times. At the end of the data acquisition, the quantity of images is high because each captured image is slightly different from the others for reasons such as a short exposure time from the camera, a short exposure time from the LEDs and the unstable nature of the transonic flow.

**Data filtering**

Due to the small lens exposure window during the capture and the low intensity emitted from the paint luminophores, digital filters need to be applied to prevent the error from growing. The two dimensions in which the data is filtered are the spatial and time dimensions. Before each image is further processed, it needs to pass through spatial filtering to have the noise removed by smoothing the image. Filtering in time removes the outliers that appear when performing multiple acquisition sets in the same spatial location. Figure 4.2 shows a schematic drawing of the same pixel location through a period in time. Once the outliers are removed, the average of each capture window can be computed, thus the average background, first capture and second capture. Section 5.1 explains the digital filtering of the data in more detail.

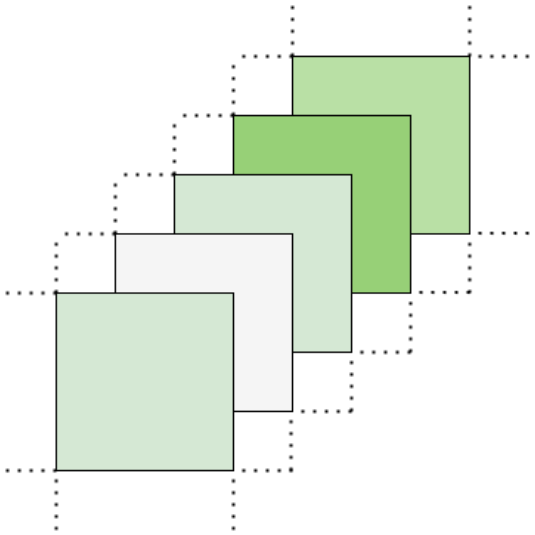

**Figure 4.2:** Schematic drawing of how a pixel may vary through time.

### 4.2.2. Measurements overview

There are three distinct measurements to perform for performing the experiments. The first is the calibration of the PSP, which also doubles as a verification of the measurement technique. The calibration data is meant to provide information about the technique giving a logical trend regarding the lifetime with respect to the pressure for which an environment with a controllable pressure (and temperature) is necessary. This trend is then used for the second set of measurements, the validation experiments. The validation experiments are performed in the wind tunnel, for these measurements, the pressure is determined by both the PSP and pressure taps, the idea is to see how accurately the calibration trend can be used to compute the pressure and fine-tune the equation for the pressure accordingly. The main sets of measurements are done on a model whose surface pressure is unknown and there is no other method to measure it.

**Calibration/Verification of PSP**

The methodology for the calibration of the pressure sensitive paint follows the previous steps up to the lifetime computation, see Figure 4.3. The idea behind the calibration of PSP is to obtain a trend of the luminophores' lifetime with respect to the pressure while controlling for the pressure and ideally also for the temperature. The lifetime at different pressures is then used for obtaining a lifetime ratio. Figure 4.4 shows a schematic of what the lifetime ratio vs. pressure plot looks like, the trend follows from Equation (4.2). $\tau_0$ is the decay rate at a reference pressure and $\tau$ is the decay rate at the specific pressures. When performing the calibration(/verification), it is expected to obtain an increasing ratio with increasing pressure. The trend from the calibration is then applied in future calculations for determining the pressure. The verification can be deemed successful when the lifetime ratio increases linearly with increasing pressure when the temperature remains the same throughout all of the measurements.

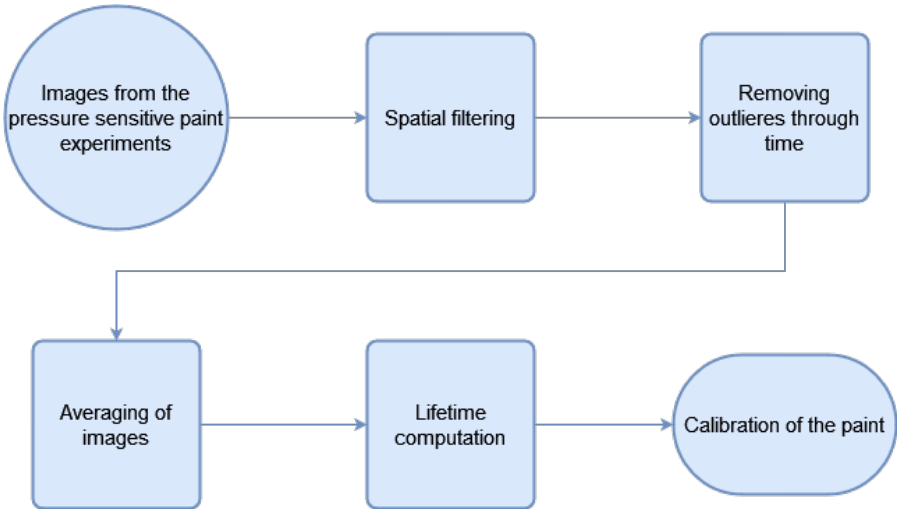


**Figure 4.3:** Flowchart of the calibration.

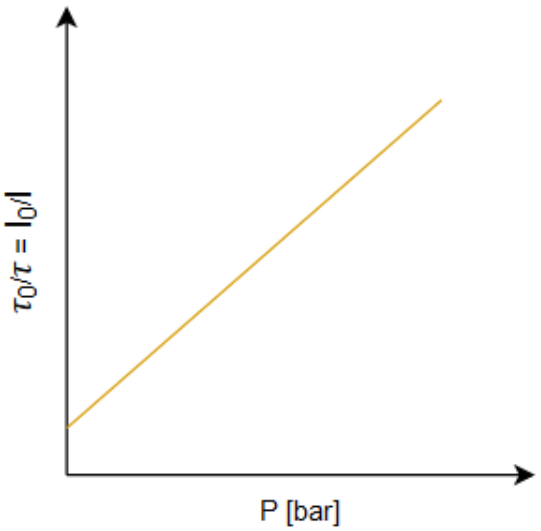


**Figure 4.4:** Schematic of the lifetime-pressure relation

**Validation and main experiments of PSP**

The methodology for the validation uses the lifetime-pressure trend from the calibration. The main goal of the validation is to find out if PSP provides reliable experimental data. For this, the trend from the calibration is used to compute the pressure, which is then compared to other pressure data. Pressure taps are reliable enough to compare the PSP data to the taps data. Any discrepancies in the results lead to a slight adjustment of the lifetime-pressure trend line from the calibration. These validation experiments also serve as an in-situ calibration of the paint. Figure 4.5 shows the validation flow diagram.

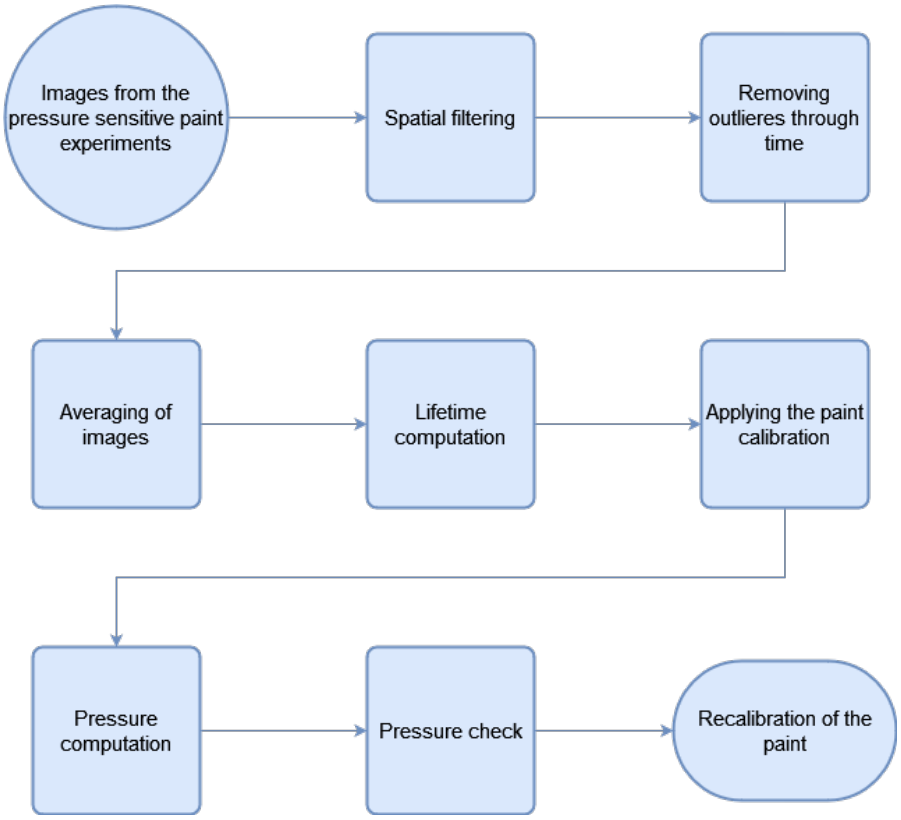


**Figure 4.5:** Flowchart of the validation.

Once the validation is successful, the main experiments can be performed. Figure 4.6 shows the schematic of the flow diagram for the main experiments. The flow shows that unlike for the verification and validations, the pressure cannot be checked anymore. And the pressure results from this data is then used for determining the pressure coefficient and the lift coefficient.

## 4.3. Experiment Setup

This section serves to present the experimental setup for the completion of the experimental objective. The experiments take place in the TST-27 wind tunnel at the High-Speed Lab of the Aerospace Engineering faculty of the TU Delft.

**TST-27 Transonic/Supersonic wind tunnel**

The TST-27 is a blowdown wind tunnel, which means that the airflow is being produced by the rapid discharge of a high-pressure tank. The wind tunnel has a test section of 280mm wide and a height that varies from 250mm to 270mm depending on the Mach number. The

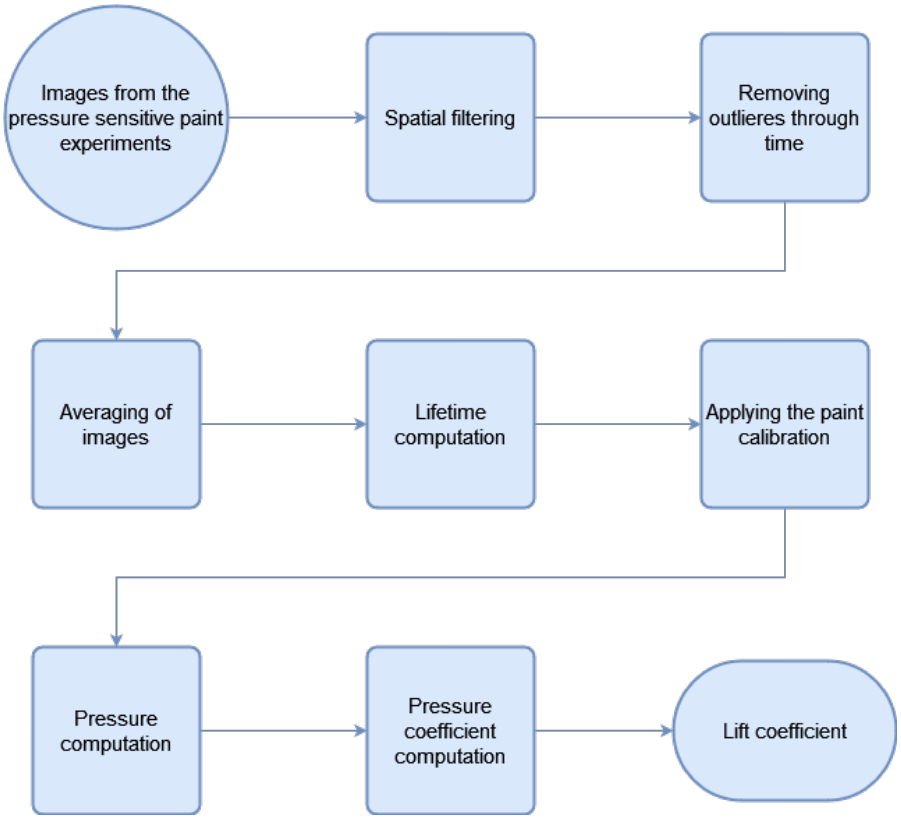


**Figure 4.6:** Flowchart of the main experiments with the OAT15A supercritical airfoil.

Mach numbers for the tests range from 0.5 to 0.85 in subsonic speeds and from 1.15 and 4.2 for supersonic speeds. For setting the supersonic Mach number the throat can be varied continuously and there are flexible upper and lower nozzle walls. A variable choke section in the outlet of the diffuser controls the subsonic Mach numbers. And, an automatic fine adjustment of the choke corrects for small deviations in the Mach number. The TST-27 has a running time that can go up to 300 seconds which allows for exploring the flow of a model in more detail. The tunnel was designed for operating at high stagnation pressures; the maximum Reynolds number varies from 38 million per meter in the transonic regime to 130 million per at Mach 4. meter. Figure 4.7 shows a schematic drawing of the TST-27 wind tunnel.[1]

### 4.3.1. Experimental Preparation

This subsection aims to present the experimental preparation necessary for performing the tests.

### 4.3.2. Experimental setup of the digital equipment

The general setup for the experiments consists of a computer. From this computer, the rest of the hardware is controlled. The computer is connected to a programmable timing unit that sends a pulse to an sCMOS camera and the Stanford pulse generator. The Stanford sends a pulse to trigger the LED lamps. The schematic of the setup is shown in Figure 4.8.

Figure 4.9 shows the same general setup but with the Scanivalve also connected to the PC this time. This setup is meant for the verification and validation experiments to obtain data

[1] https://www.tudelft.nl/lr/organisatie/afdelingen/flow-physics-and-technology/facilities/high-speed-wind-tunnels/tst-27-transonicsupersonic-windtunnel

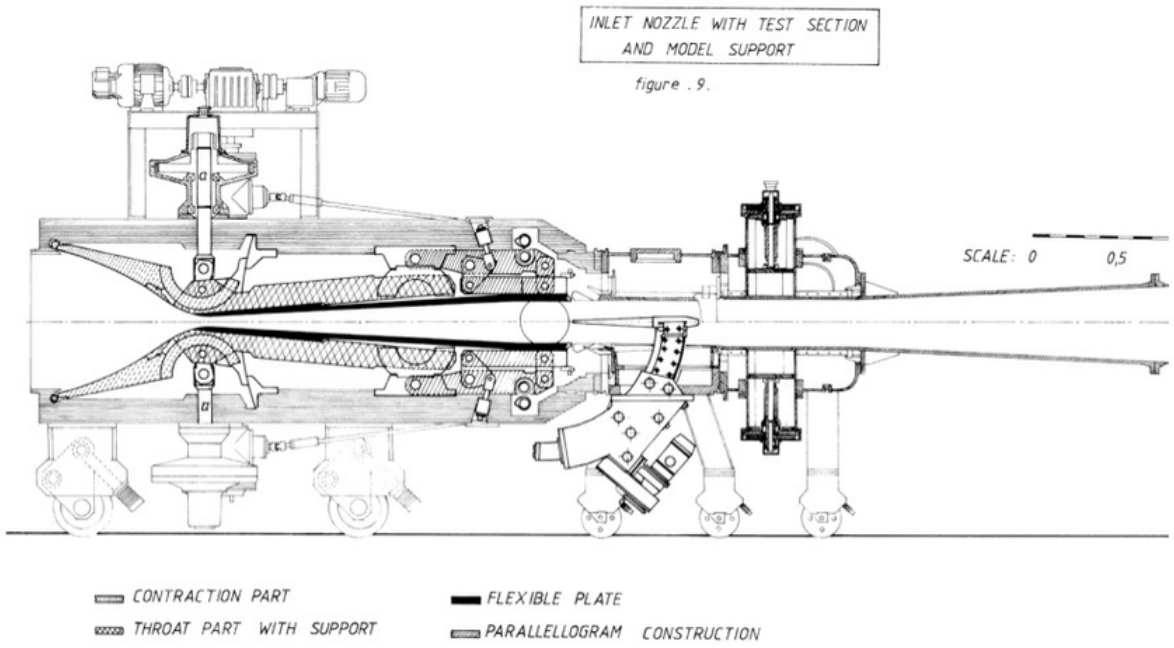


**Figure 4.7:** Schematic drawing of the TST-27 wind tunnel at the TU Delft.

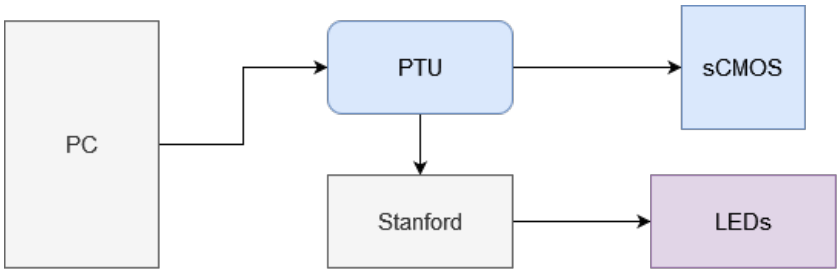


**Figure 4.8:** Schematic representation of the general PSP setup.

from pressure taps.

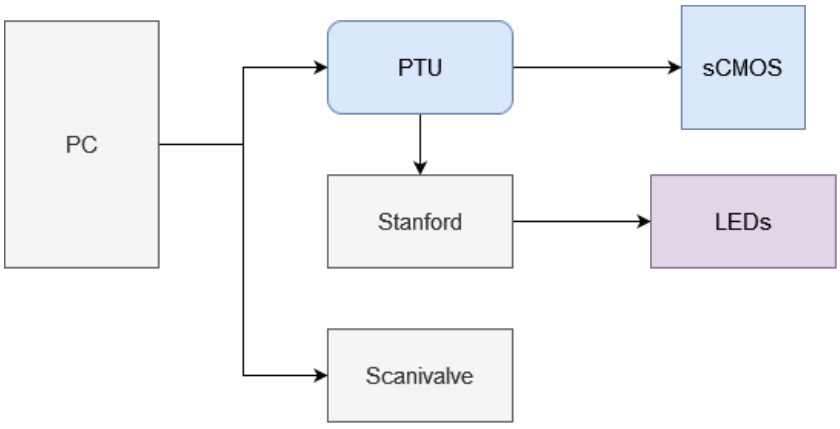


**Figure 4.9:** Schematic representation of the general PSP setup with the Scanivalve.

**Timing of the pulse trigger**
Because the Stanford Pulse generator is needed, the exact timing of when it triggers the LED lamps has to be determined. Any occurring delay between the pulse sent by the PTU and that sent by the Stanford has to be accounted for. However, another timing issue to take into consideration is the camera failing to do two consecutive captures after the LED emission with this setup.

Firstly, the two camera exposure times need to be determined. Figure 4.1 shows a sketch of the emitted intensity of the luminophores when a LED pulse is applied and when the camera captures would need to take place. The first exposure should occur right after the LED and the second one a few microseconds past that. The idea is to obtain the emitted intensity as the luminophores decay to determine the lifetime of the paint molecules.

There is a limitation in the equipment that makes it impossible to perform double camera triggers, one after the other, after just one LED pulse. This limitation is the inability to perform two camera captures right after the other with the same time exposure and without triggering the LED lamps. Therefore, the camera trigger and exposure had to be kept constant while the LED trigger varied. This can be seen in Figure 4.10, where the camera pulse remains in the same position, but the pulse of the LED will switch with time. This will then mimic the double camera exposures.

Figure 4.11 shows how the timings for triggering the LED lamps are determined. In the image, it is noticeable that the camera trigger and exposure always happen at the same time, so with the Stanford pulse generator, two pulses can be sent to the LED lamps. The first pulse starts at A and ends at B, and the second pulse starts at C and ends at D. So, the times A, B, C and D need to be found. However, this leads to the second timing check, which is to check for any delay that could be happening between the camera's trigger and exposure.

Figure 4.12 shows the schematic of the method necessary to accomplish the timing setup because of possible delays between equipment triggers. The first step is to make the pulse of the LED lamps as small as possible, so the error margin decreases by ruling out a moment where the LED is not illuminating during the time of the camera exposure. The second step is changing the pulse in large enough time intervals to figure out when approximately the camera exposure starts. Once the approximate location in time of the exposure concerning the camera trigger is known, the light pulses can be shifted to smaller intervals to that time location to get to microseconds. Figure 4.13 shows the plot with the intensities of the pictures used for determining the timing which is determined using the method from Figure 4.12. Figure 4.13 shows that the actual capture and LED triggers coincide at a delay time between 9.915 and 9.925ms, the images showing how the intensities change with time are shown in Figure 4.14.

The pulse delay values found are A=0.05898s, B=0.05990s, C=0.10896s and D=0.10988s for a trigger frequency of 20Hz. The camera exposure was chosen to be $30\mu s$, that of the LED to be $20\mu s$ and a dt difference for the captures to be also $20\mu s$.

### 4.3.3. Experimental setup and list of equipment
This subsection aims to present the experimental equipment and preparation for the experiments.

**Experimental preparation and the models**
The equipment for the experimental preparation consisted of the pressure sensitive paint and the models. The paint is the UniFIB®Pressure Sensitive Paint, which consists of one

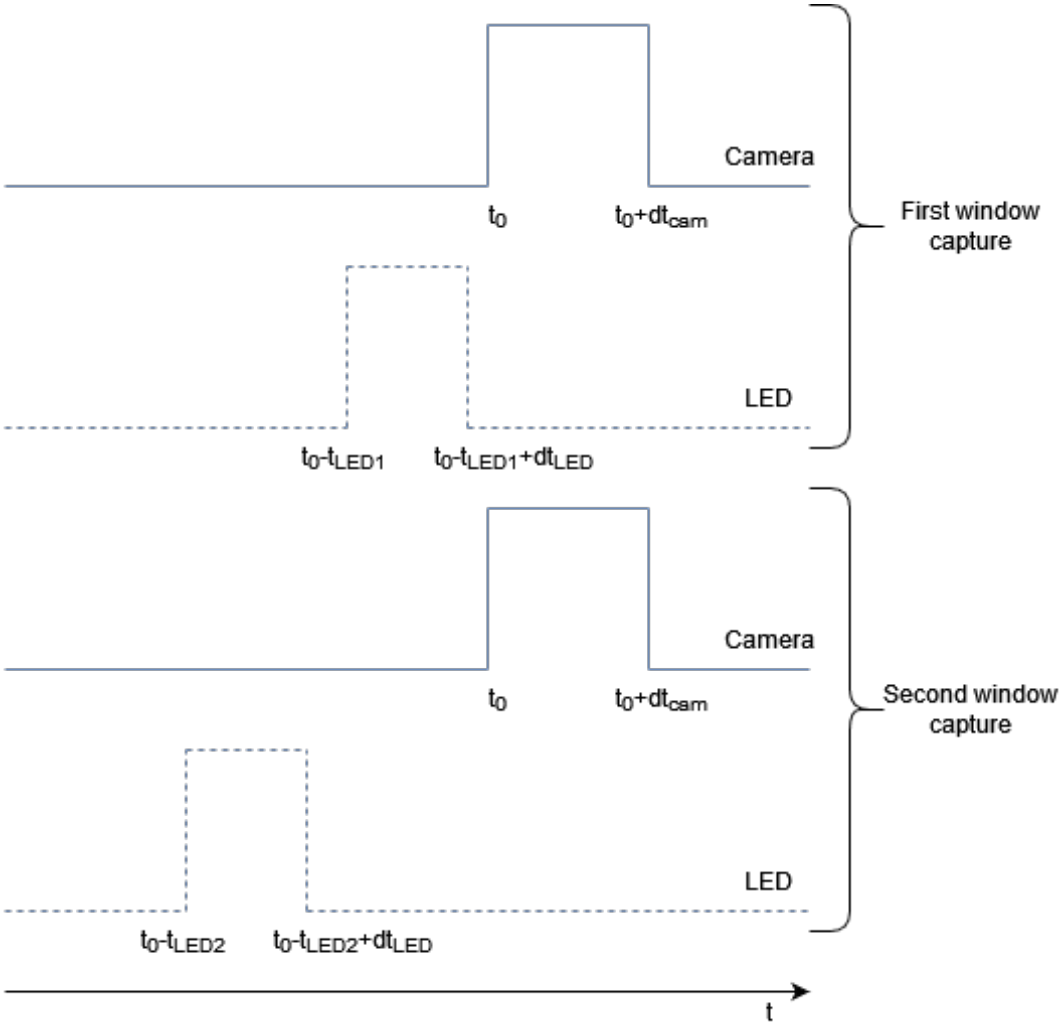


**Figure 4.10:** Schematic of when the pulse to trigger LED lamp needs to happen for obtaining a first and second camera capture.

luminophore. The model for the calibration is a big shock control bump, the model for the validation is a cone, and the model for the main experiments is a vertical OAT15A model with and without shock control bumps.

Both the big shock control bump and the cone are 3D printed models. The cone also has pressure taps to obtain the pressure at multiple points on the model. The length of the cone is 20cm and has 10cm diameter. The airfoil is a vertical OAT15A airfoil model with a chord of 10cm. A transition trip is placed at 7% of the chord to stabilise the flow, see Figure 4.15.

The first thing for the experiments consists of painting the models. The test models need to be fully covered by the paint by spraying. Once the models are painted, they need to be stored in a sealed and dark place until the time they are tested. Otherwise, the luminophores react with the oxygen in the environment and the light in the ambient. Figure 4.16 shows on the left, the airfoil right after the primer was applied, and on the right, the painted models. For the wind tunnel runs, the angle of attack of the model need to be set. Figure 4.17 shows how the angle of attack was set for the vertical airfoil. The digital level is placed on the airfoil and the airfoil's position is slightly altered until the desired angle is reached.

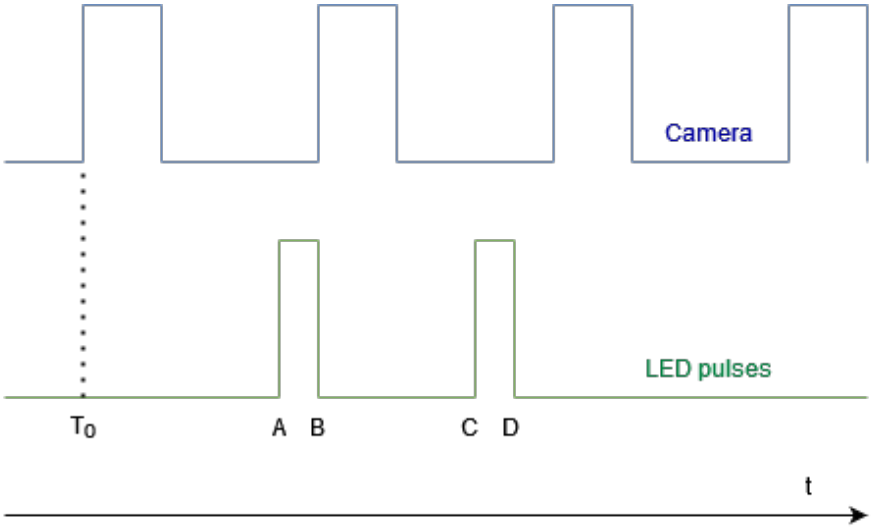


**Figure 4.11:** Schematic of the necessary pattern of pulses for the experiments. The top part shows the camera acquisition pulses, where the time between the start of the first pulse and the start of the second is $\frac{1}{f_{camera}}$s, where $f_{camera}$ is the frequency of pictures taken per second. The bottom shows the LED pulses set by the pulse generator.

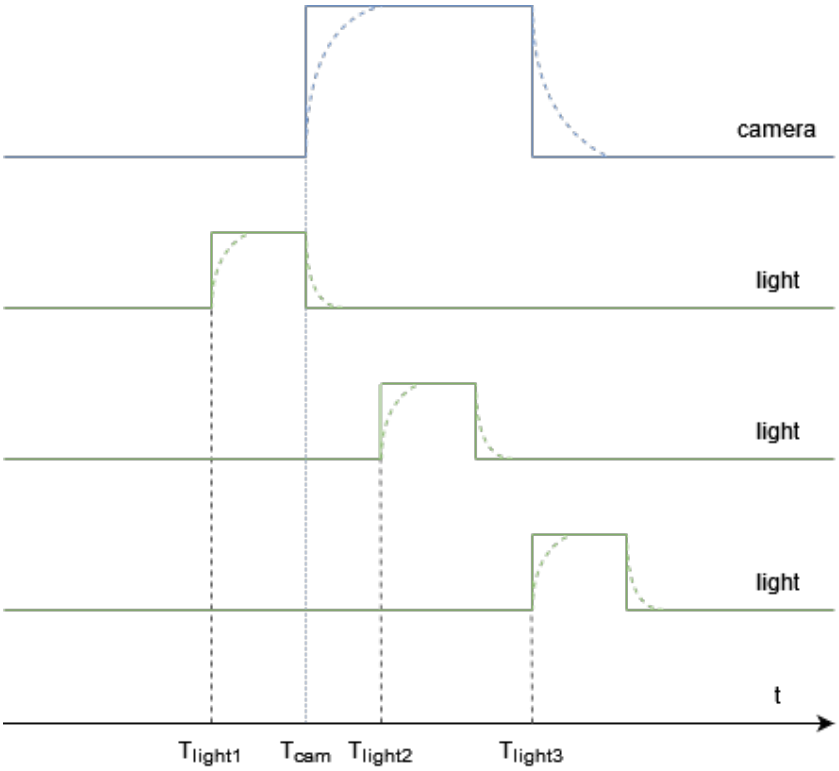


**Figure 4.12:** Schematic of the methodology for finding the trigger-pulse offset.

### General equipment

The general list of equipment consists of the equipment necessary for the verification & validation of the measurement technique and for the main experiments. The equipment is the following:

- Camera: LaVision sCMOS
- Filter: Kodak 75mm #29 Deep Red Wratten 2

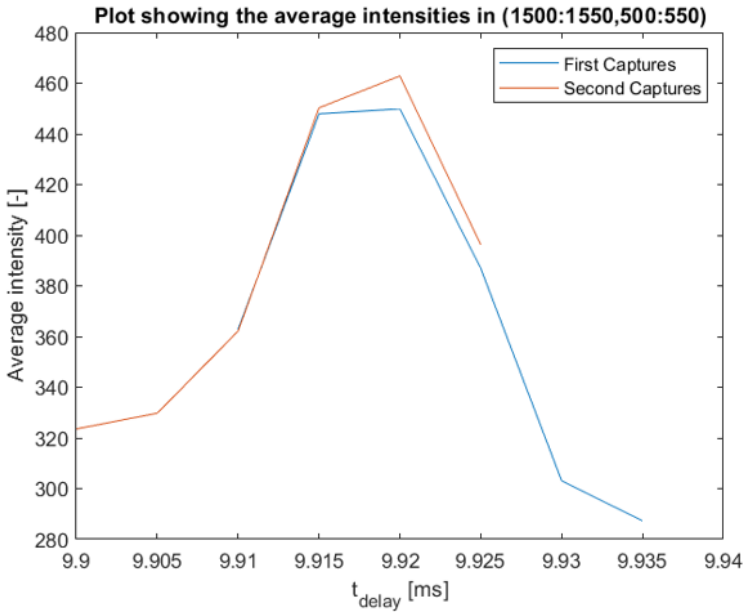


**Figure 4.13:** Plot showing the intensities for determining the delay of the Stanford trigger.

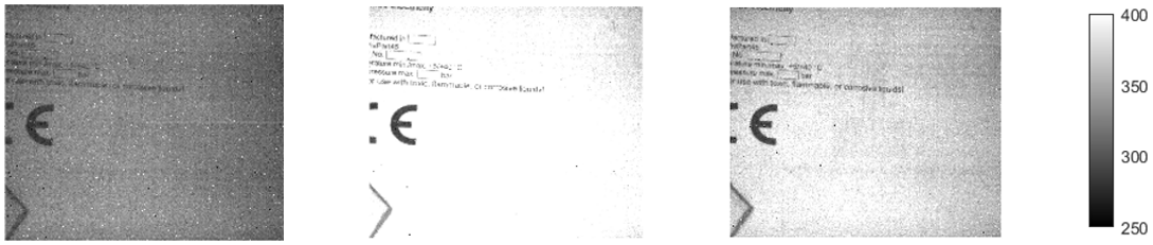


**Figure 4.14:** Photos of the images for determining the delay of the Stanford trigger. On the left: a delay of 9.905$\mu s$. In the centre: a delay of 9.915$\mu s$. On the right: a delay of 9.925$\mu s$.

- Lens: Nikon AF-S NIKKOR 60mm
- Programmable timing unit: LaVision PTU
- Pulsing unit: Stanford Digital Delay Generator DG535
- 2 UV LED lamps: 2-inch Air-Cooled from ISSI

**Extra equipment for the calibration and the validation**

For the validation, the only extra equipment is the **Scanivalve pressure sensor**, which is connected to the cone for the experiment.

**Extra equipment for the verification/calibration**

The calibration of the PSP also requires **a pressurized chamber to control the pressure and a thermocouple** to know if there are any changes to the temperature.

### 4.3.4. Experimental models in their experimental setting

**Calibration/Verification experiments model**

The model for the calibration is a big 3D-printed SCB, see Figure 4.16. The model's requirement was to fit in the pressurised chamber, see Figure 4.18. The SCB is a representation of the SCBs that are placed in the airfoil for the main experiments.

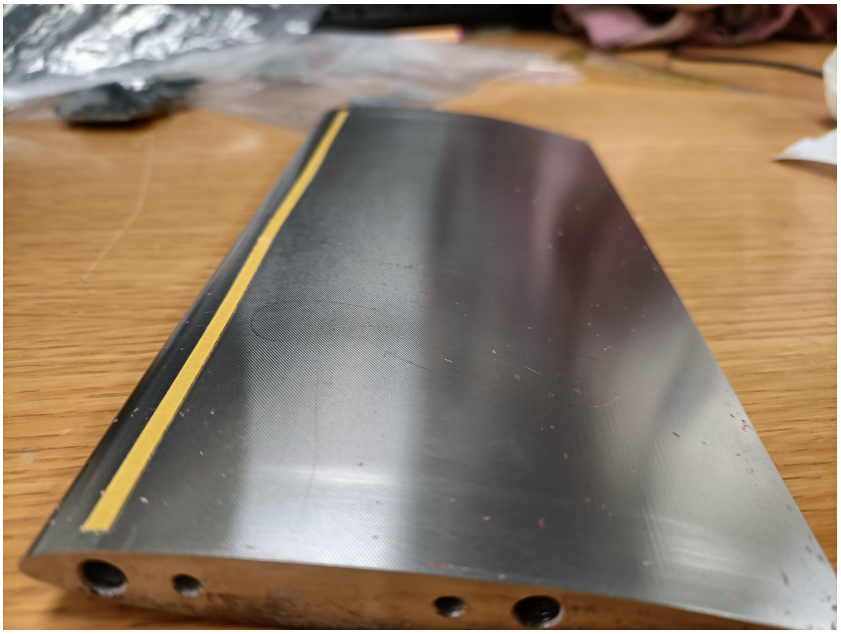

**Figure 4.15:** The OAT15A model with the transition trip on it.

**Figure 4.16:** On the left: the airfoil after having been primed. On the right: the big SCB, the airfoil and the cone having been painted.

### Validation experiments model

The model for the validation experiments for the technique is a 3D-printed cone with pressure taps along its length. It is a 20cm long cone with a base diameter of 10cm. Figure 4.19 shows the model in the wind tunnel.

### Main experiments model

The model for the main experiments consist of a vertical ONERA OAT15A supercritical airfoil model. The chord of the model is 10cm and the span is 20cm. A 2mm transition trip at 7% of the chord from the leading edge is placed on the airfoil to ensure that the flow on the airfoil remains as homogeneous as possible. The transition trip consists of Carborundum particles.


**Figure 4.17:** Setting the angle of attack of the airfoil.

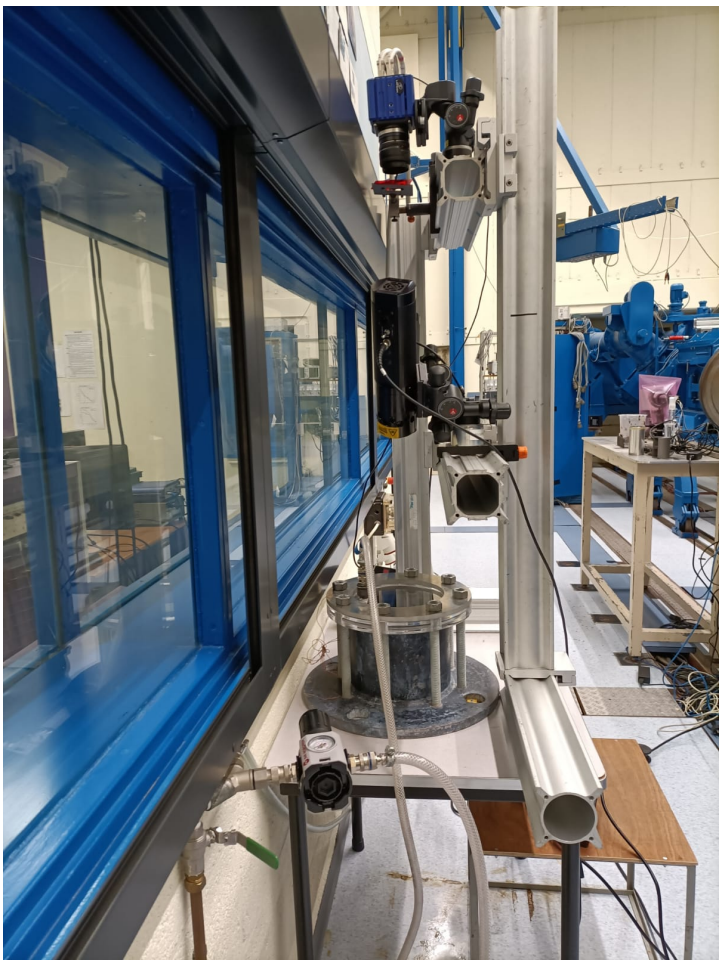

**Figure 4.18:** Photograph of the setup for the paint calibration.

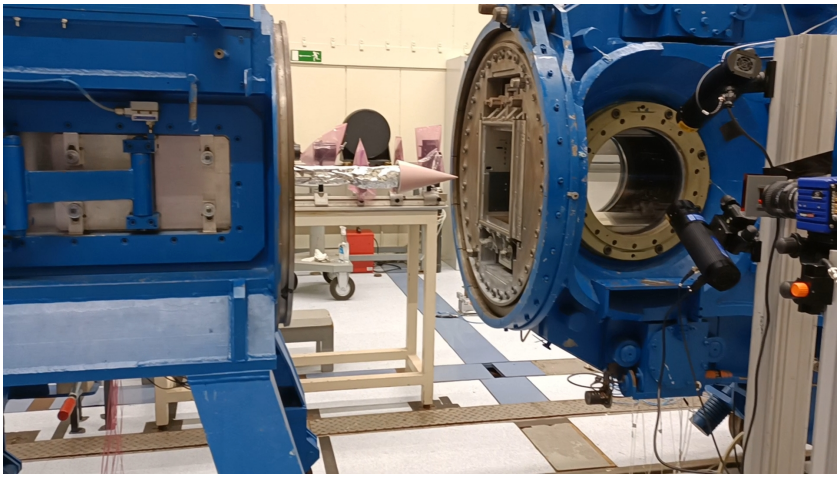

**Figure 4.19:** Photograph of the setup for the validation experiments.

For the runs to study the effect of SCBs, 5 small SCBs are placed on the top of the airfoil at 30% of the chord from the leading edge. Figure 4.20 shows part of the general equipment in the setup for the main experiments.

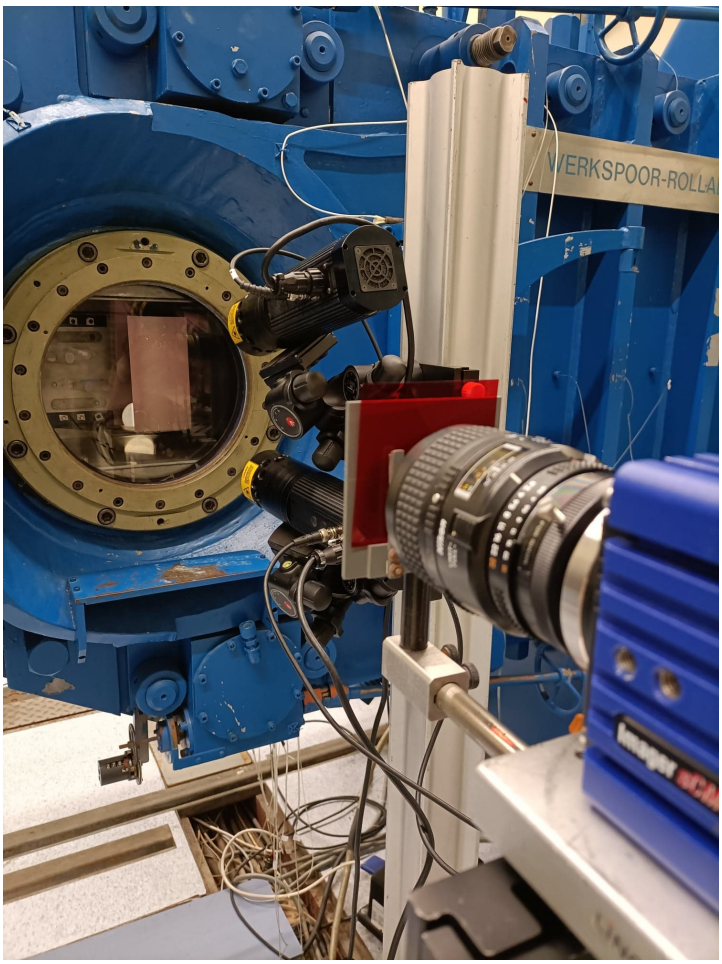


**Figure 4.20:** Photograph of the painted OAT15A airfoil in the wind tunnel. The LED lamps are pointed towards the model. The red light filter is in front of the lens of the sCMOS camera.

# 5

# Data Processing and Calibration

A crucial part of the research is processing the data acquired during the experiments. The data handling needs to follow a specific order for processing the results. In this chapter, the processing is explained with the use of the calibration data. Therefore, this chapter aims to provide the data processing and the calibration of the PSP technique.

## 5.1. Filtering of the images

This chapter explains the process for filtering, smoothing and removing the outliers from the data to keep the error as low as possible throughout the calculations. There were two methods to filter the images captured during the experiments. The first filtering is in the spatial domain, which reduces the noise significantly. The second way is to filter the data in the time domain to get rid of the outliers that could influence the averaging of the images negatively.

### 5.1.1. Spatial image filtering

For performing the spatial filtering, as soon as the image was loaded in MATLAB, it was smoothed. The reason for filtering each picture as it is being loaded into MATLAB before further data processing is the high levels of noise obtained during the captures. It is necessary to take this noise out of the images when they are still raw because the error caused by the noise can exponentially grow as the data processing continues. Figure 5.1 shows a schematic drawing of how a specific region in space might have some noise standing out. The image represents a small area in the capture, and it serves to show how some pixels are not equally intense, even though they captured the same region, or the jumps between the intensities of the pixels are too high to make sense (like salt and pepper on the image).

The filter used for noise removal and smoothing in the spatial domain is the Gaussian filter found in the MATLAB library. This Gaussian filter follows the Gaussian distribution given by the following equation:

$$G(x, y) = \frac{1}{2\pi\sigma^2} e^{\frac{-x^2+y^2}{2\sigma^2}}$$

The filter size of the function is determined by the value of $\sigma$ leading to a filter size equal to $2(2\sigma) + 1$. A way to see this is taking a $\sigma$=0.5, this leads to a filter size of 3. Figure 5.2 shows a visual example of how a pixel is treated when a filter size of 3 is applied. A $\sigma$ of 1 was used for handling the experimental data, this leads to a filter size of 5.

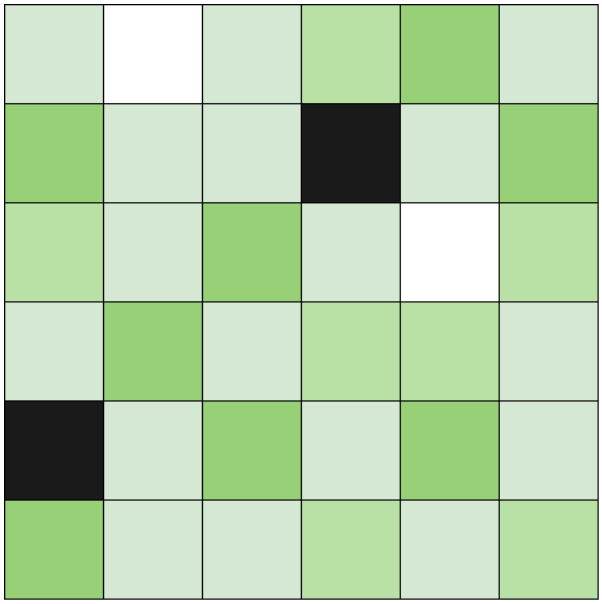

**Figure 5.1:** Representation of a group of pixels in no particular region in space showing noise and unevenness.

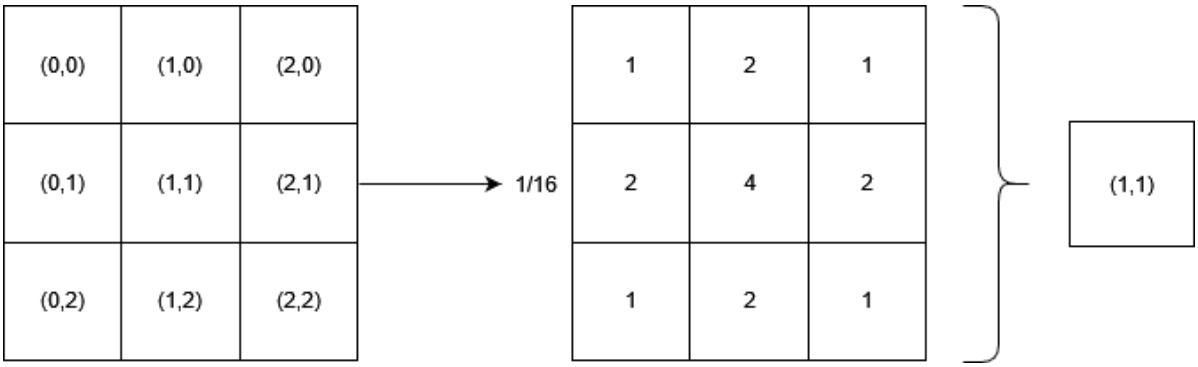


**Figure 5.2:** Diagram showing how a pixel is smoothed by a Gaussian filter using a filter size of 3.

To illustrate the spatial filtering process more tangibly, Figure 5.3 shows three completely raw images of the big SCB model inside the pressurized chamber at 1 bar. These images correspond to the first camera exposure after the LED pulse. Figure 5.4 shows how those same images look after the Gaussian filter is applied.

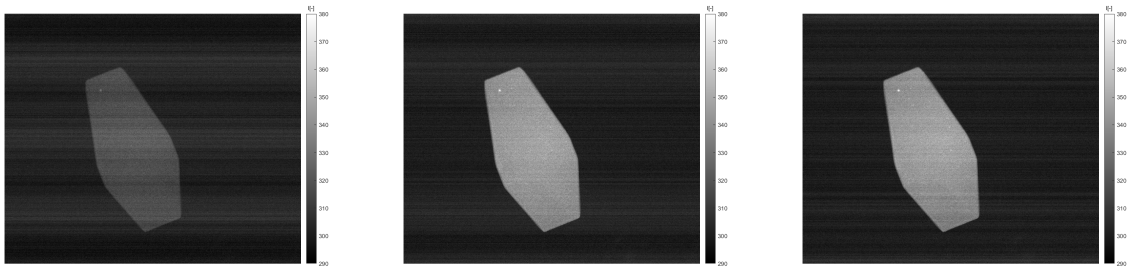

**Figure 5.3:** First three raw images of the first capture in the pressurized chamber at 1 bar before applying the Gaussian filtering. On the left: the first raw image captured. In the centre: the second raw image captured. On the right: the third raw image captured.

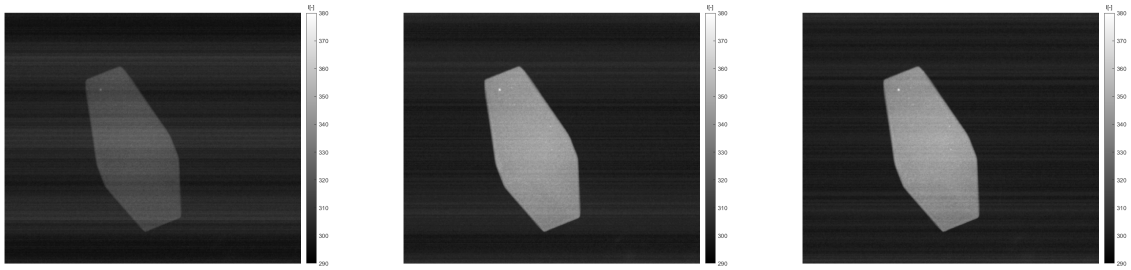

**Figure 5.4:** First three raw images of the first capture in the pressurized chamber at 1 bar after applying the Gaussian filtering. On the left: the first raw image captured. In the centre: the second raw image captured. On the right: the third raw image captured.

### 5.1.2. Filtering images through time

The reason for filtering through time is that a specific pixel in space can have different intensities at different points in time, which would act as one (or multiple) outlier(s), as shown in the schematic drawing of Figure 4.2. Some differences in pixel intensities within time are expected because of performing the experiments in the transonic regime. However, if the values are outliers that mend the data in any manner that adds an error to further data, they should be removed from the data set. This error continues to propagate through each computation growing more and more. For removing these outliers, the pixels throughout time with a value higher than twice the standard deviation of that pixel were removed.

The reason for using two times the standard deviation comes from a trade-off between the number of images left for the average and the removal of the pixels that distort the data the most. See Figure 5.5 for a visual representation of the number of data points per pixel that are removed.

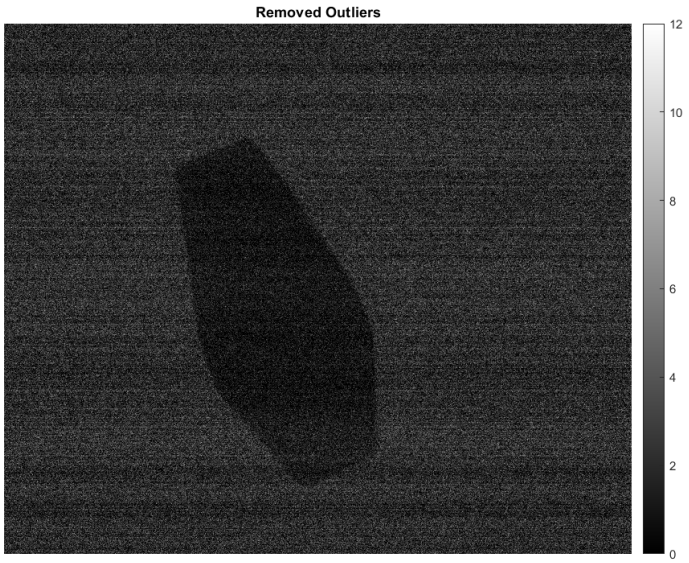


**Figure 5.5:** Plotted image of the outliers that were removed.

### 5.1.3. Averaging

Once the images are free from noise and outliers, they are ready for averaging. The reason for the averaging is to have a more distinctive image that represents the average of the flow, due to the unstable flow over the surface of the airfoil. Figure 5.6 shows the average of the images, and Figure 5.7 shows the average without the background, which was also completely filtered before the removal.

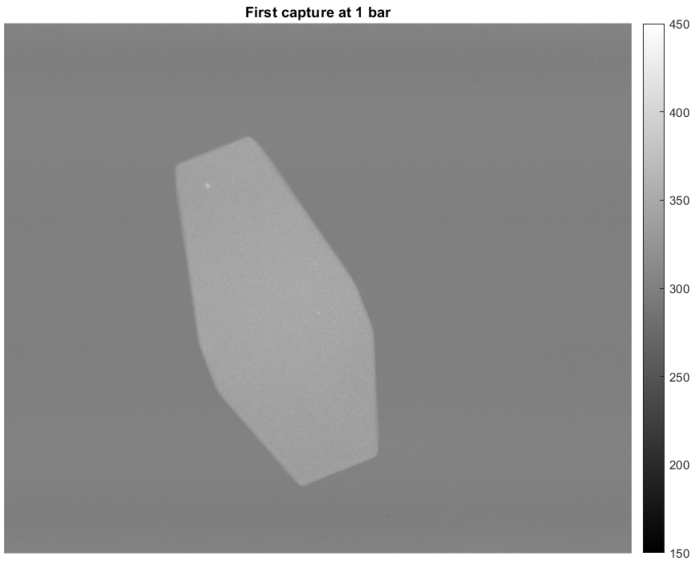


**Figure 5.6:** Averaged result of the images at 1bar.

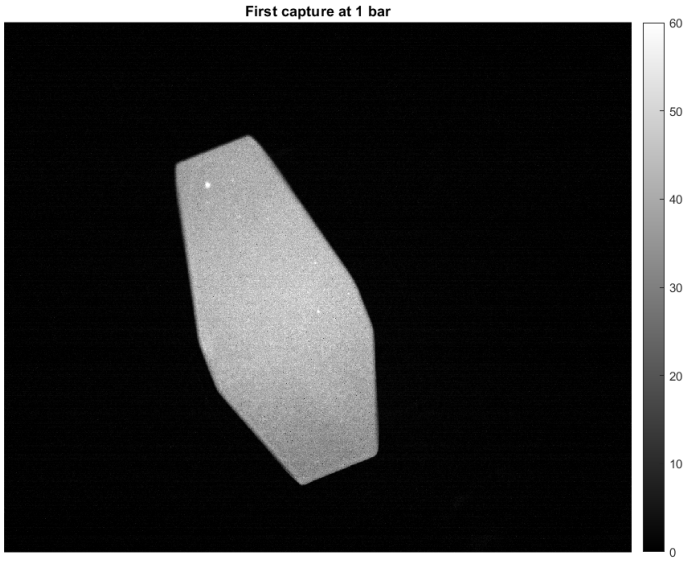


**Figure 5.7:** Averaged result of the images at 1 bar with the background removed.

## 5.2. Lifetime and calibration curve

Finding the lifetime is a crucial step in PSP. Equation (4.1) provides the relation to calculate the lifetime using the averages of the first and second exposure. Figure 5.7 shows the intensity of the first exposure and Figure 5.8 shows the average intensity of the second exposure.

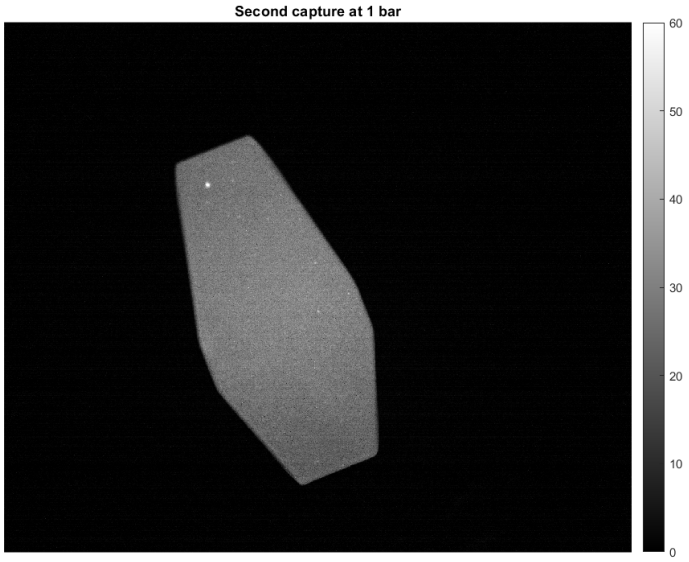


**Figure 5.8:** Averaged result of the images at 1 bar with the background removed. Second capture.

The lifetime is computed using the intensity ratio. Figure 5.9 shows the intensity ratio of both exposures on the left and the right lifetime.

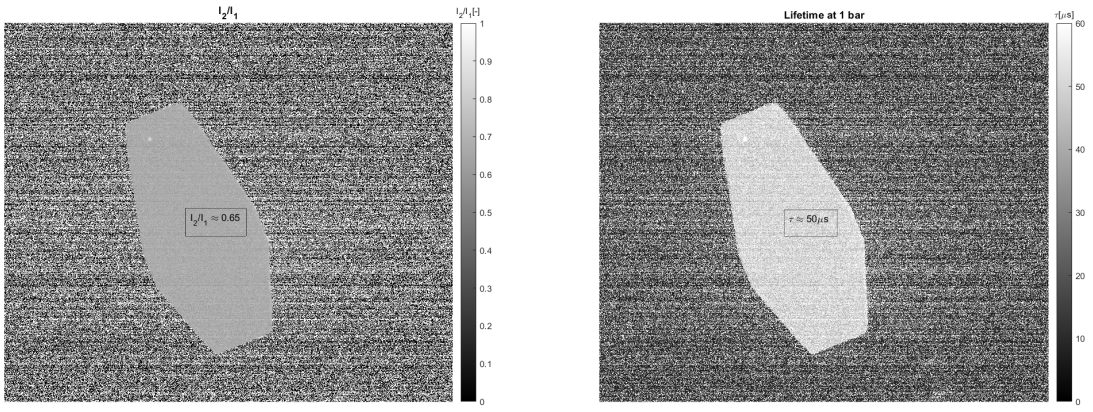


**Figure 5.9:** Intensity ratio on the left and lifetime image on the right.

The literature says that the lifetime-pressure trend is a decline in the lifetime as the pressure increases. Figure 5.10 shows two different plots, on the left, the lifetime at 1 bar and on the right, the lifetime at 2 bar. From the figure, it is clear that the lifetime indeed decreases with increasing pressure.

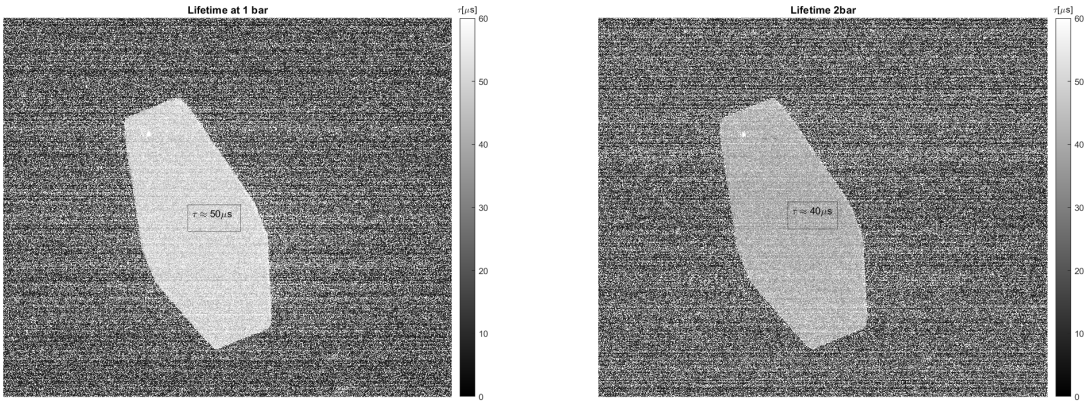


**Figure 5.10:** On the left: lifetime for 1bar. On the right: lifetime for 2bar.

Because two cases are not enough to show the trend, multiple pressures were set in the pressurized chamber. The first thing to notice is a decrease in intensity as the pressure increases, see Figure 5.11. This is caused by higher oxygen levels when higher air pressure is present.

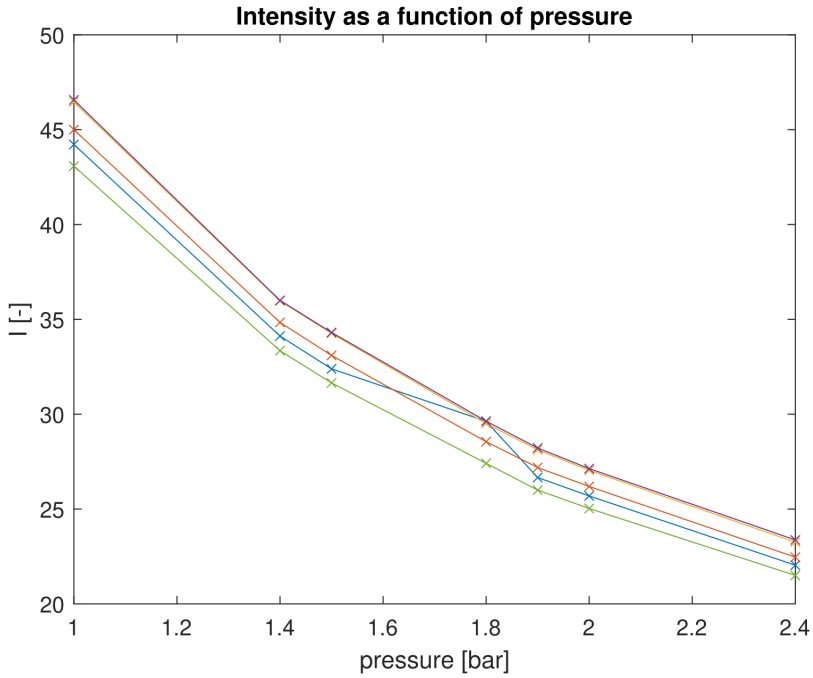


**Figure 5.11:** Intensity-pressure relation

The lifetime for all of the cases was obtained. The lifetime obtained for the 1bar case is then divided by the lifetime for each of the other pressures. This lifetime ratio is plotted for getting the lifetime-pressure trend. Figure 5.12 shows this lifetime trend.

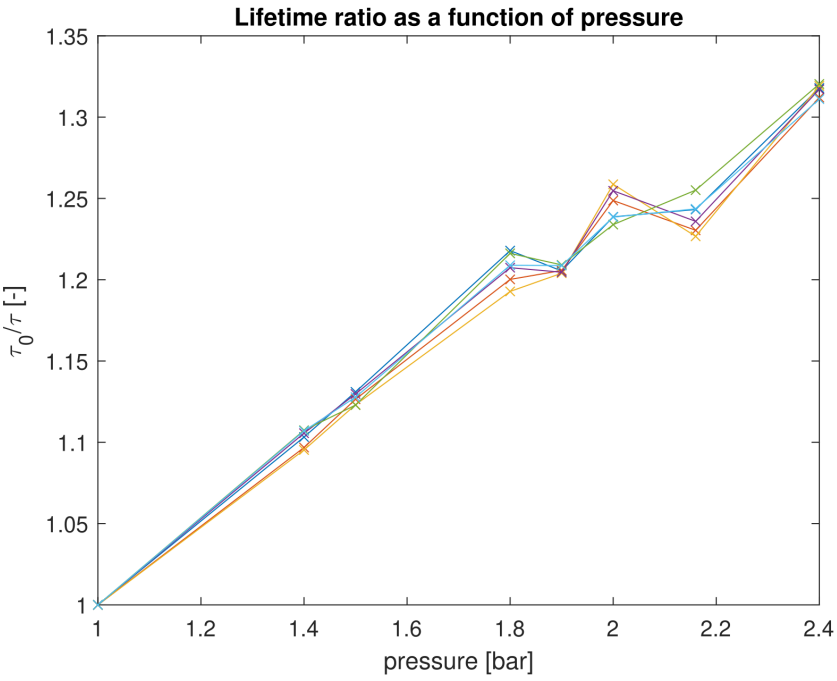


**Figure 5.12:** Lifetime-pressure relation with each line at a different location in the image.

Due to the constant temperature in the pressurised chamber and the lack of knowledge of the temperature in the wind tunnel, the temperature-dependent functions are assumed to be constant. Using the results from the lifetime ratio trend (4.2) with A(T) and B(T) assumed as constants, the equation is:

$$\frac{\tau_0}{\tau} = 0.75 + 0.25\frac{P}{P_0}, with P_0 = 1bar. \tag{5.1}$$

To check for the equation, this equation is plotted together with the lifetime ratio trend for the different locations in the images, as seen in Figure 5.13. The sensitivity of the paint is for a pressure of up to 2 bar[1], which is why the fit was done for lower pressures.

[1] https://innssi.com/wp-content/uploads/Pressure_Sensitive_Paint/UniFIB/Documentation/UniFIB-PSP-UF-XXX-Data-Sheet.pdf

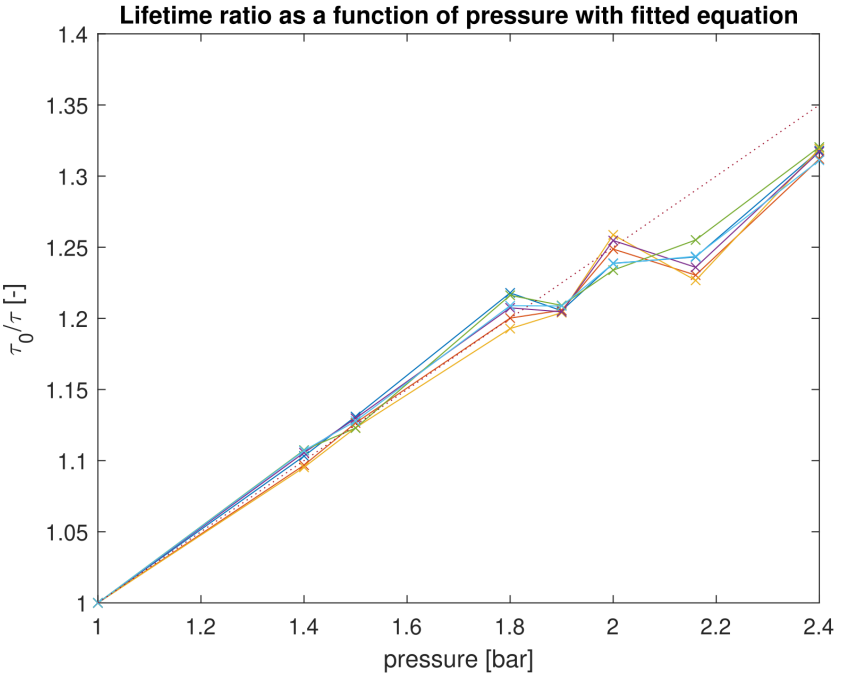


**Figure 5.13:** Lifetime-pressure relation with equation check in the dotted line.

# 6
# Results

This chapter presents the results from the experiments carried out in the wind tunnel using pressure sensitive paint as the flow measurement technique.

## 6.1. Validation Results

This section presents the results from the validation experiments. The validation experiments were conducted in the TST-27 wind tunnel at a Mach number of 0.5 and total pressure of 1.5 bar. The validation experiments also serve as an in-situ calibration. The conditions of the experiments were set to match those of the experiments conducted by Tambe et al. (2022) to be able to check the results with the results from those experiments.

### 6.1.1. Intensities

The first results from the experiments are averaged images of the two camera capture windows. These images provide the average intensity of the captures during the data acquisition. There are three sets of two capture windows for the validation. The first set of captures is acquired before the wind tunnel run, while the surface pressure is 1 bar. The second set is during the wind tunnel run, in which the expected intensity is lower because the surface pressure on the cone increases, as measured by the pressure taps. The final set of data happens after the wind tunnel test, which is when the experienced surface pressure on the cone is 1 bar. The intensities captured before the wind tunnel run are shown in Figure 6.1, the figure shows a decrease in intensity for the data captured during the second window.

Figure 6.2 shows the captured intensities during the wind tunnel run. The intensities are lower, which corresponds to the data obtained with the pressure taps. Furthermore, as the flow passes in a streamwise direction along the cone, the pressure surface pressure decreases, as measured by the Scanivalve. The freestream flow is blocked by the cone, and the first point of contact at the tip of the cone is the stagnation point, so the static pressure is the highest at that location. As the flow keeps going downstream, the blockage of the cone increases and the pressure decreases.

The intensities captured after the wind tunnel run are shown in Figure 6.3. The image shows higher intensities than during the run, as for the case before it (see Figure 6.1).

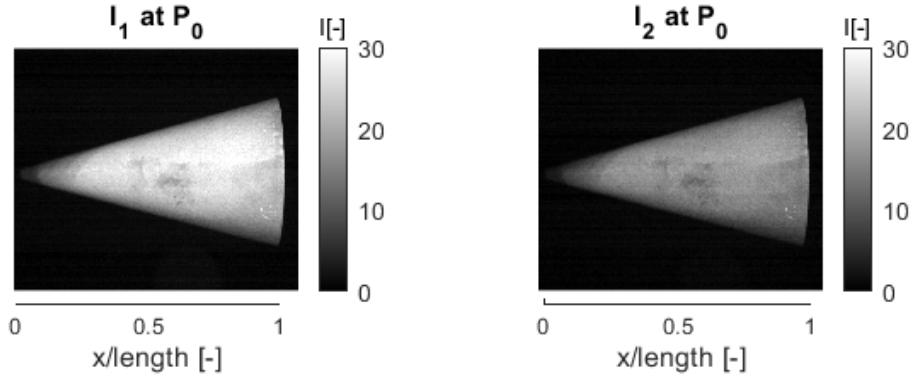


**Figure 6.1:** On the left: First capture of the intensity of the cone before the wind tunnel run. On the right: Second capture of the intensity of the cone before the run.

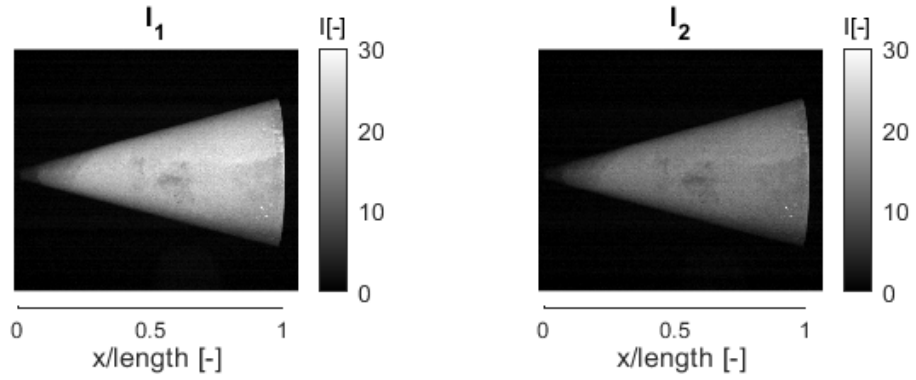


**Figure 6.2:** On the left: First capture of the intensity of the cone during the wind tunnel run. On the right: Second capture of the intensity of the cone during the run.

### 6.1.2. Lifetimes

To properly determine the pressure using PSP, the lifetime of the luminophores needs to be computed. To obtain the lifetime, Equation (4.1) was used. The lifetimes computed with the use of Figures 6.1 to 6.3 are presented in Figure 6.4. From top to bottom, the first image is the lifetime of the reference pressure before the wind tunnel, the second image shows the lifetime of the paint on the model during the wind tunnel run and the third image shows the lifetime after the wind tunnel run. The image of the cone during the run shows a lower lifetime than before or after the wind tunnel run, thus there are more oxygen molecules in the environment reacting with the luminophores, which is in agreement with the Scanivalve measurements with a pressure higher than 1 bar. However, the fact that the pressure decreases as the flow moves downstream is not noticeable to the naked eye in the figure.

Figure 6.5 shows the lifetime ratio using both the pre-and post-run measurements. The ratio for both cases is larger than 1, which means that the cone experiences a pressure higher

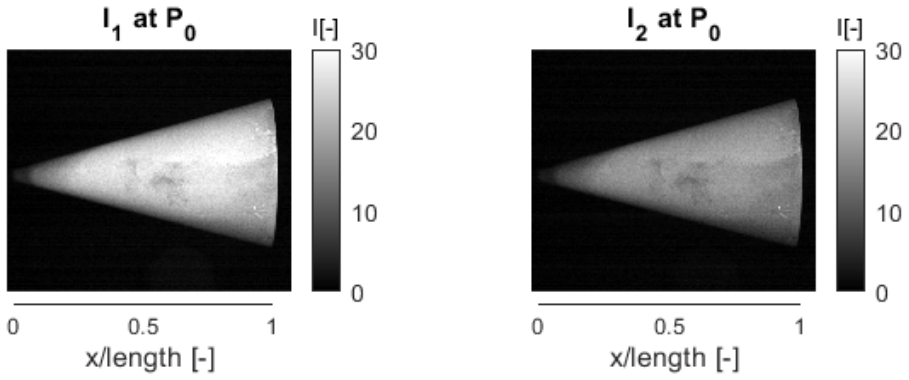


**Figure 6.3:** On the left: First capture of the intensity of the cone after the wind tunnel run. On the right: Second capture of the intensity of the cone after the run.

than ambient pressure during the run. With Equation (5.1) the pressure throughout the length of the cone can be computed.

### 6.1.3. Pressures

The pressure equation obtained using the ambient pressure before the wind tunnel run changed from Equation (4.2) to $\frac{\tau_0}{\tau} = 0.75 + 0.28\frac{P}{P_0}$ because the environmental conditions in the wind tunnel were not the same as during the experiments in the pressurised chamber, therefore, the validation experiments also serve as an in-situ calibration. The main reason is the temperature not being constant prior to, during and after the wind tunnel runs. Figure 6.6 shows the results when using this equation. It is visible that when the equation has been altered, the pressure from the lifetime matches that obtained with the pressure gauges. The RMS at x/length = 0.55 to 0.59 is 1.23 bar and the Scanivalve value is 1.21 bar.

For the case of using the pressure with the post-run ambient pressure, the equation became $\frac{\tau_0}{\tau} = 0.75 + 0.31\frac{P}{P_0}$. Figure 6.7 shows the results when using this equation. It is visible that when the equation has been modified, the pressure from the lifetime matches that obtained with the pressure gauges. The RMS at x/length = 0.55 to 0.59 is 1.17 bar and the Scanivalve value is 1.21 bar. The two different equation changes can be explained by the difference in temperature as the lifetime increases in the data acquisition after the wind tunnel run due to the lower temperature.

From the fine-tuning for both cases, it is clear that when the data from before the wind tunnel run is taken as a reference value, the change in the calibration equation is 50% lower. From this, the only thing that can be concluded is that the temperatures during the calibration match better than that of the computations with data pre-run. No one of these cases is better than the other because there is no data on the temperature to calibrate and measure during the wind tunnel runs. Therefore, one is meant for the calculations using one reference and the other as a second reference.

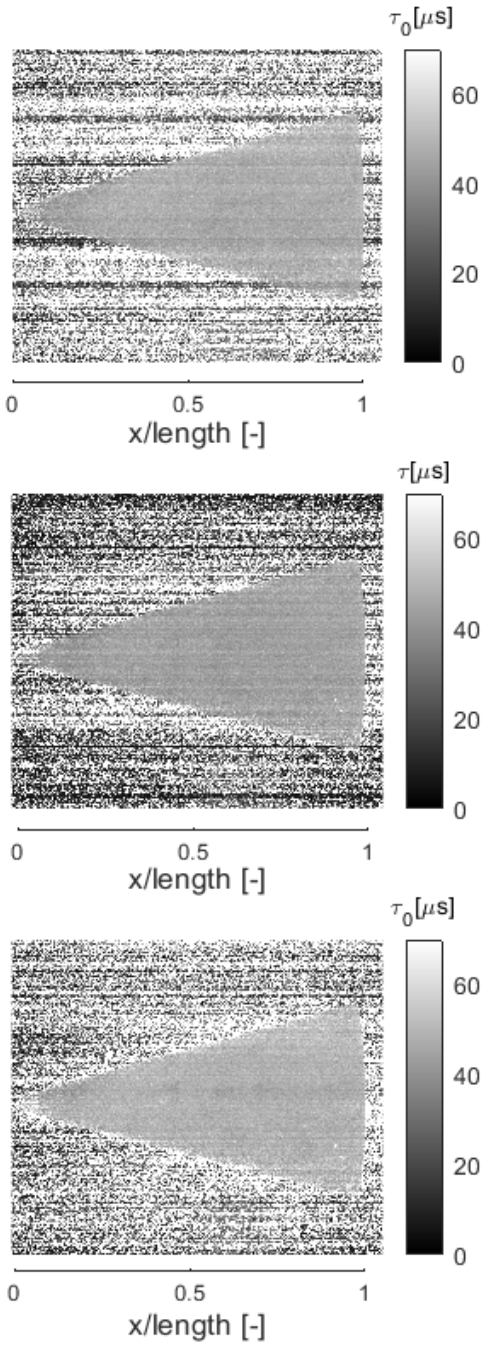


**Figure 6.4:** Plot of the lifetime for the three sets of data. On the left: the lifetime of the cone at ambient pressure before the wind tunnel run. On the centre: the lifetime of the cone during the wind tunnel run. On the right: the lifetime of the cone at ambient pressure after the wind tunnel run.

### Temperature and noise

As seen from the results, the temperature of the surface of the model plays an important role in determining the lifetime of the luminophores. As mentioned in Section 5.2 for the experiments the temperature functions of the lifetime equation are treated as constants, which creates

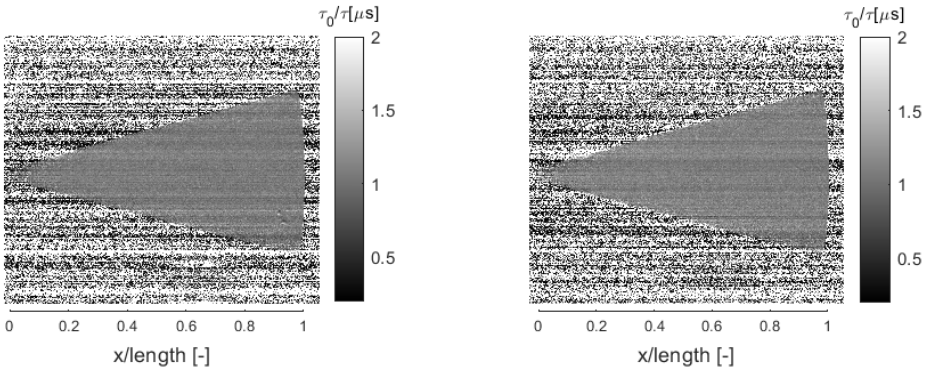


**Figure 6.5:** The two lifetime ratios of the validation experiment. On the left with the reference pressure pre-run and on the right with the reference post-run.

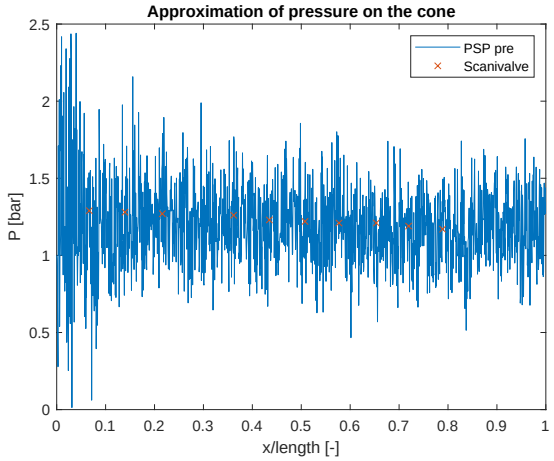


**Figure 6.6:** Plotted pressure using the lifetime ratio with the data captured before the wind tunnel run.

an error in computing the pressure. This can be seen in the equations for the cases using the pressure before and after the wind tunnel run, where the temperature changes before, during and after the run. During the main experiments with the airfoil, the error due to the temperature will be larger because of the lack of ability for fine-tuning the equation throughout the entire surface of the model and time. Another important factor in reducing the accuracy of the measurements is the high amount of noise. The trend of the pressure fits the pressure from the Scanivalve. These were the first measurements in the wind tunnel, thus the amount of paint and exact position of the camera and LEDs with respect to the models were still being optimized, which contributed to higher levels of noise. There is another increase in noise,

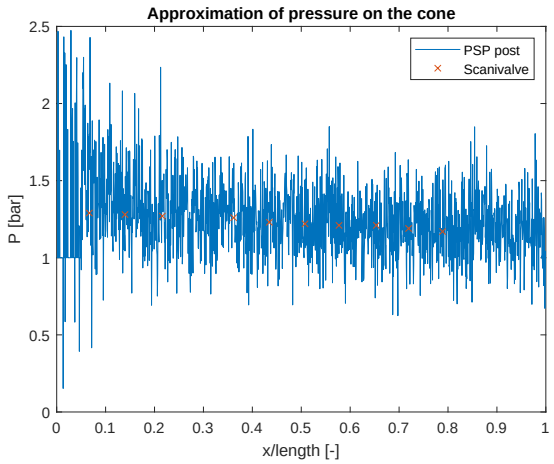


**Figure 6.7:** Plotted pressure using the lifetime ratio with the data captured after the wind tunnel run.

which has increased with each computation further from the intensities towards the pressure. Because the equation to determine the lifetime does not account for the actual value but it takes a ratio, the noise does not remain unnoticeable.

## 6.2. OAT15A Supercritical Airfoil Results

The purpose of this section is to present the results from the experiments with the OAT15A airfoil. For testing the vertical wing, there were three different setups. The first set-up was the pressure side of the airfoil facing the window of the wind tunnel. The second set-up was the clean configuration of the suction side of the airfoil facing the window of the wind tunnel. The third and final one is the airfoil with shock control bumps, whose suction side is placed towards the window.

Figure 6.8 shows how the surface locations of the wind tunnel model correlate to the airfoil's chord location. The reason for this is that it is difficult to know which part of the chord the image is showing and what it looks like.

### 6.2.1. Image intensities

The results of the main experiments also consist of two reference measurements, one before and after the wind tunnel run, and one during the run. Starting with the clean configuration of the suction side: Figure 6.9 shows the average results from the two capture windows before the wind tunnel as the first reference. Figure 6.10 shows the intensity results from the model during the wind tunnel run. The captures show the shape that the shock wave takes on the airfoil. Throughout the span of the airfoil, the location of the shock varies causing the curved-shaped location. This whole region with higher emitted intensity is where the shock oscillates and happens between where the trip line is located and about 40% of the chord corresponding to a lower pressure in that area of the surface. The second reference measurements are shown in Figure 6.11.

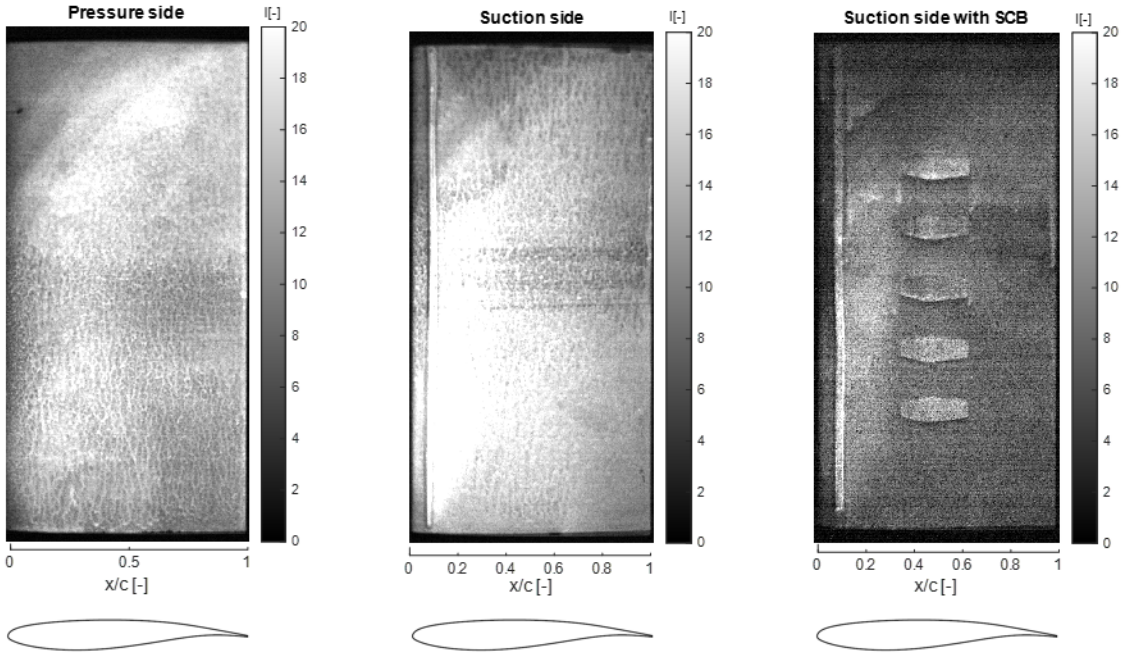


**Figure 6.8:** Images showcasing what the results of the model in the wind tunnel look like with respect to the OAT15A airfoil chord.

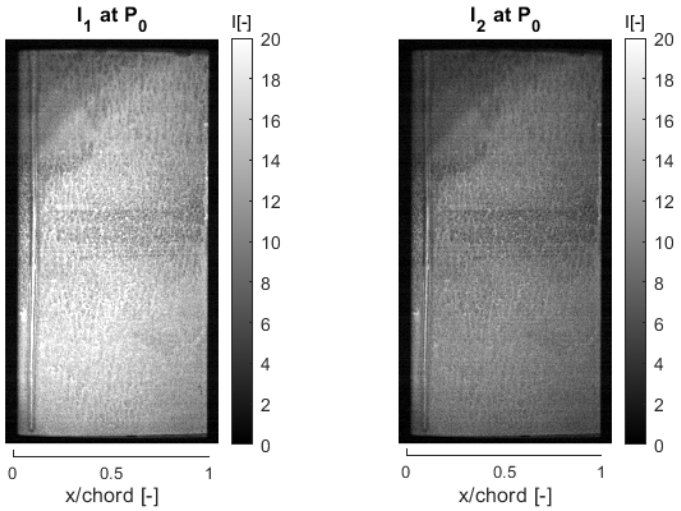


**Figure 6.9:** On the left: First capture of the intensity of the clean configuration before the wind tunnel run. On the right: Second capture of the intensity of the airfoil before the run.

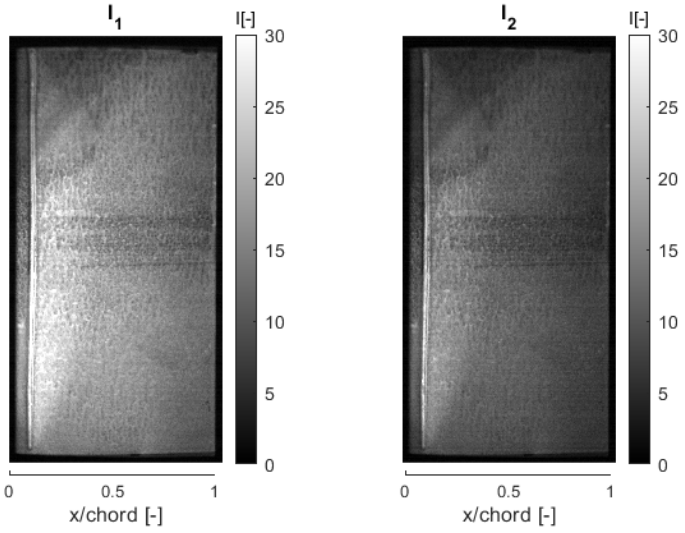


**Figure 6.10:** On the left: First capture of the intensity of the clean configuration during the wind tunnel run. On the right: Second capture of the intensity of the clean configuration during the run.

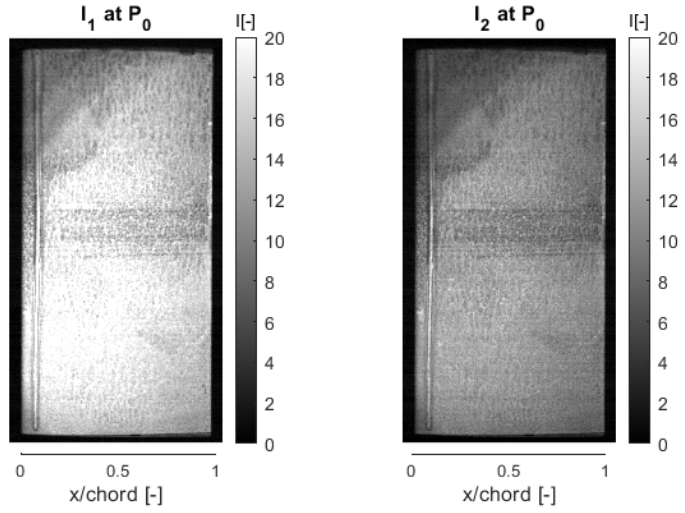


**Figure 6.11:** On the left: First capture of the intensity of the clean configuration after the wind tunnel run. On the right: Second capture of the intensity of the airfoil after the run.

The capture of reference measurements for the pressure side of the airfoil is shown in Figure 6.12. Figure 6.13 shows the average of the captured images for the measurements during the wind tunnel run. From the image, it is noticeable, that the region from the leading edge to half the chord has a lower pressure than from half the chord towards the trailing edge. Figure 6.14 shows the measurements from the reference after the wind tunnel run.

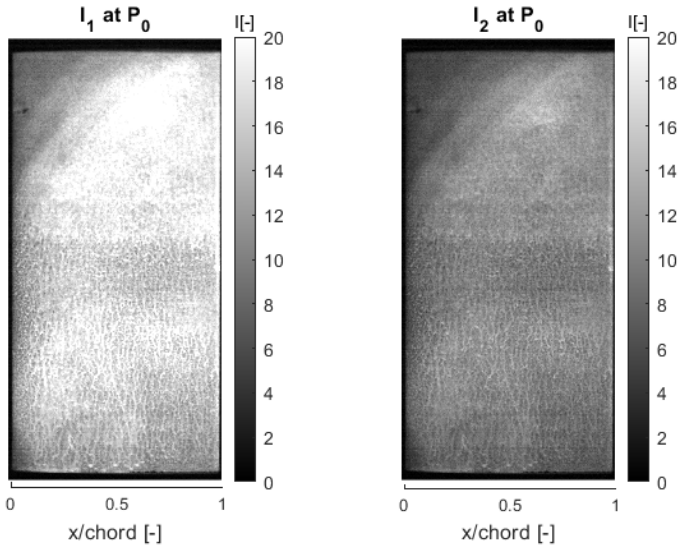


**Figure 6.12:** On the left: First capture of the intensity of the pressure side before the wind tunnel run. On the right: Second capture of the intensity of the pressure side before the run.

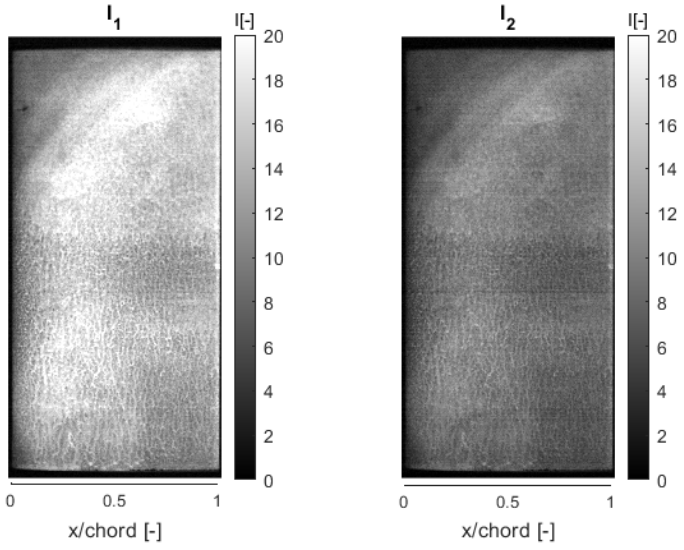


**Figure 6.13:** On the left: First capture of the intensity of the pressure side during the wind tunnel run. On the right: Second capture of the intensity of the airfoil during the run.

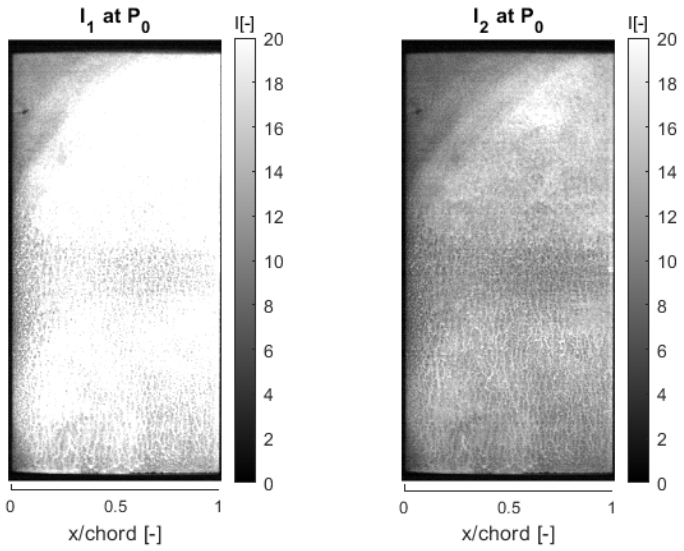


**Figure 6.14:** On the left: First capture of the intensity of the pressure side after the wind tunnel run. On the right: Second capture of the intensity of the airfoil after the run.

The averaged capture windows from the reference measurements of the suction side of the airfoil with SCBs are shown in Figure 6.15. The intensities from the data obtained during the wind tunnel runs are presented in Figure 6.16. The image shows a region where the shock oscillates, this region starts passing the trip line downstream until the SCBs are reached. From the intensity on the surface, it is clear that the SCBs serve to decrease the oscillatory region of the shock. The location in the chord of the shock is more stable throughout the span than for the clean configuration. The intensities for the second reference measurements are shown in Figure 6.17.

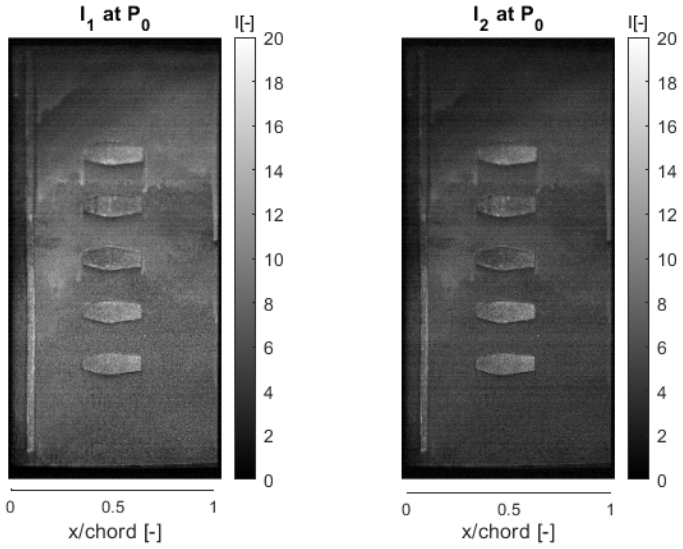


**Figure 6.15:** On the left: First capture of the intensity of the configuration with SCBs before the wind tunnel run. On the right: Second capture of the intensity of the airfoil before the run.

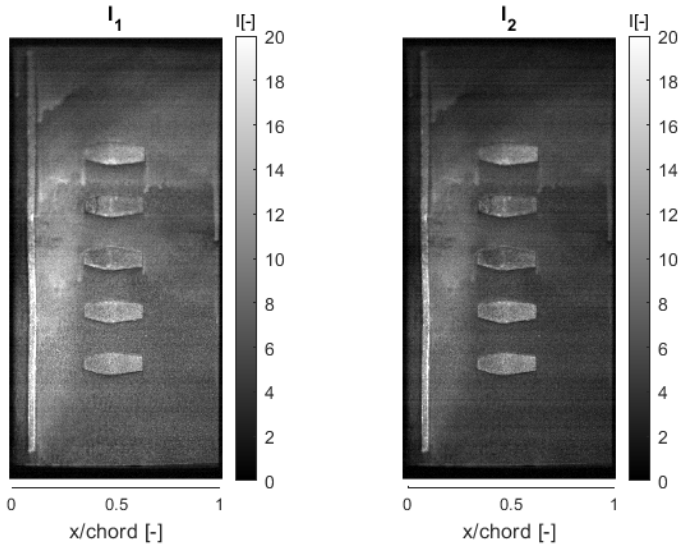


**Figure 6.16:** On the left: First capture of the intensity of the configuration with SCBs during the wind tunnel run. On the right: Second capture of the intensity of the airfoil during the run.

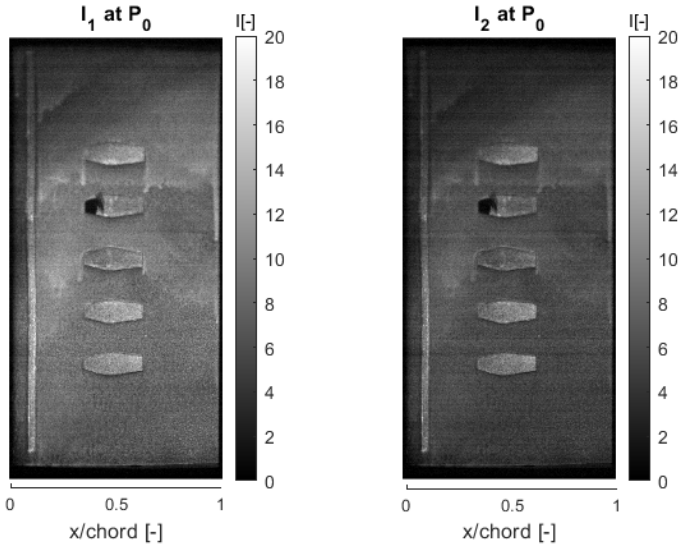


**Figure 6.17:** On the left: First capture of the intensity of the configuration with SCBs after the wind tunnel run. On the right: Second capture of the intensity of the airfoil after the run.

### 6.2.2. Lifetimes

As in the previous section, the intensities from both windows of the sets of captured images were used for the computation of the lifetimes. The first case is the lifetime of the suction side in a clean configuration, see Figure 6.18. The images show a constant lifetime for the pre-and post-run cases, which are both at ambient pressure. The data from during the run shows a higher range of lifetime values throughout the whole surface of the airfoil. The lifetime just passing downstream of the trip line is higher than that of the rest of the airfoil, with at the centre of the span with the largest area of a higher lifetime.

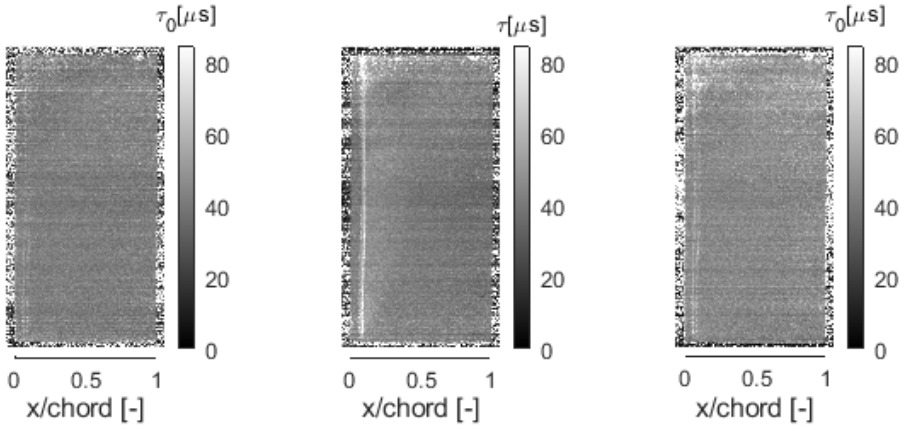


**Figure 6.18:** Lifetime, $\tau$ in $[\mu s]$, for the suction side data sets. On the left: the lifetime of the airfoil at ambient pressure before the wind tunnel run. On the centre: the lifetime of the airfoil during the wind tunnel run. On the right: the lifetime of the airfoil at ambient pressure after the wind tunnel run.

The lifetimes computed from the pressure side of the airfoil show the opposite as those from the clean suction side, see Figure 6.19. The lifetimes during the run appear to be higher than those from the captures at ambient pressure. The lifetime gradients during the run are also lower than those from the suction side of the airfoil, which until now agrees with the fact that for a positive lift to occur, the pressure side needs to experience a higher pressure than the suction side. The case with the SCBs does not show clear data by simply looking at the lifetimes from Figure 6.20. There is, however, a clear increase in the lifetime just downstream of the trip like throughout the whole region where the shock would occur, just as for the clean configuration.

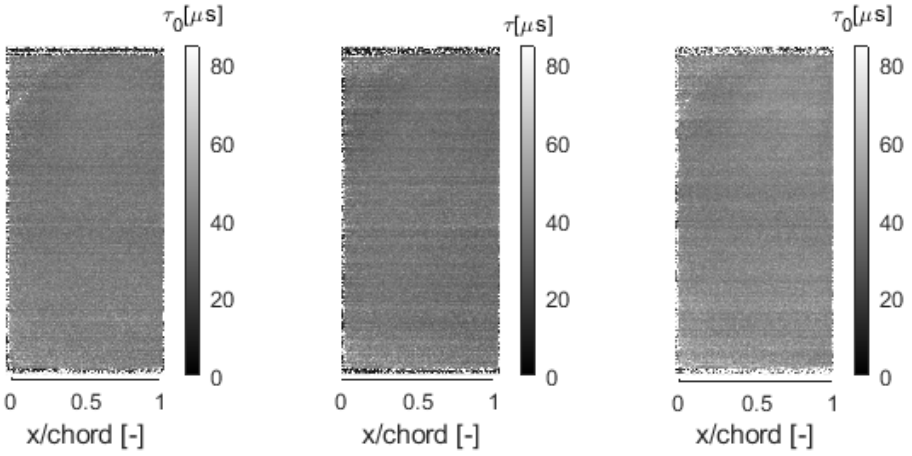


**Figure 6.19:** Lifetimes, $\tau$ in $[\mu s]$, for the three different data sets of the pressure side. On the left: the lifetime of the airfoil at ambient pressure before the wind tunnel run. On the centre: the lifetime of the airfoil during the wind tunnel run. On the right: the lifetime of the airfoil at ambient pressure after the wind tunnel run.

### 6.2.3. Lifetime ratios

The lifetime ratios provide a more accurate representation of the pressure behaviour during the experiments than just the lifetimes. The lifetime ratios of the clean configuration suction side are shown in Figure 6.21. The ratios for both cases show an overall value lower than 1.5 but starting at around 1. The region of supersonic flow is clearer in this image than in Figure 6.10 because the variables from the illumination angle and any camera tilt that could have occurred are removed. As mentioned in Section 6.1.3, the noise has increased up to this figure.

The lifetime ratios of the pressure side, see Figure 6.22, provide a higher lifetime ratio with the first part of the chord experiencing a lower ratio than after mid-chord. This lower ratio at the beginning makes sense with respect to what is expected from the literature when looking at the pressure coefficients.

The lifetime ratios from the suction side case with SCBs, see Figure 6.23, show a similar trend as the clean configuration case. The lower pressure part at the beginning of the chord is smaller than in the clean case, which can be seen as a smaller shock oscillation region. However, the data shown for the SCBs has an even higher level of noise, which is caused by the lower

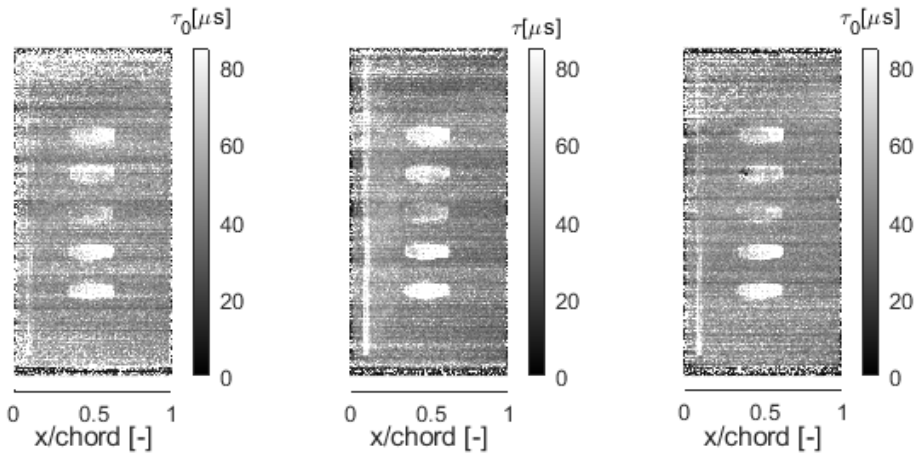


**Figure 6.20:** Lifetimes, $\tau$ in $[\mu s]$, for the suction side with SCBs. On the left: the lifetime of the airfoil at ambient pressure before the wind tunnel run. On the centre: the lifetime of the airfoil during the wind tunnel run. On the right: the lifetime of the airfoil at ambient pressure after the wind tunnel run.

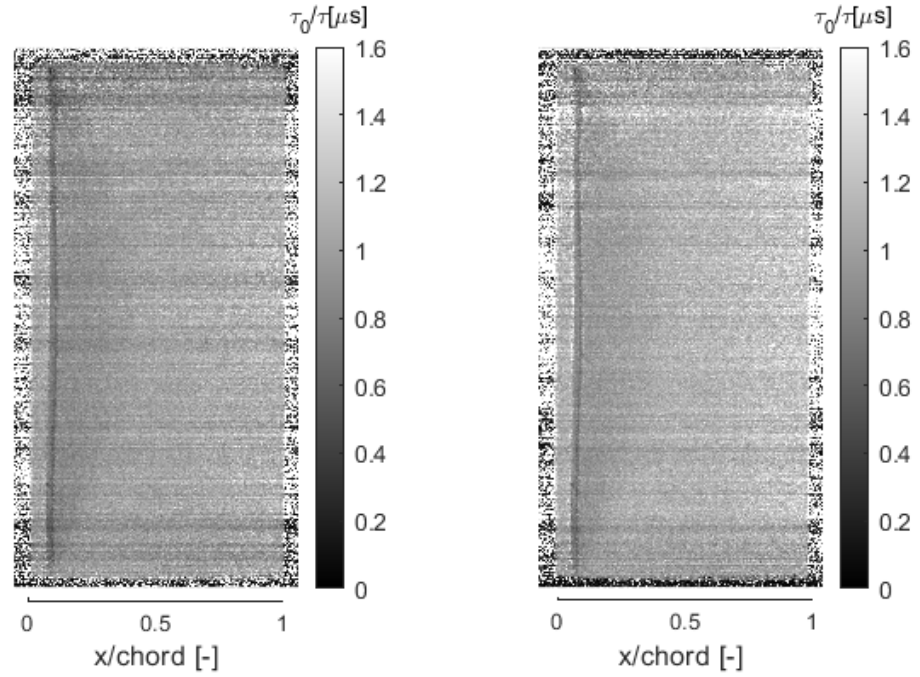


**Figure 6.21:** Lifetime ratios, $\tau_0/\tau$, from the suction side data. On the left: the ratio using the lifetime at ambient pressure before the run. On the right: the ratio using the lifetime at ambient pressure after the run.

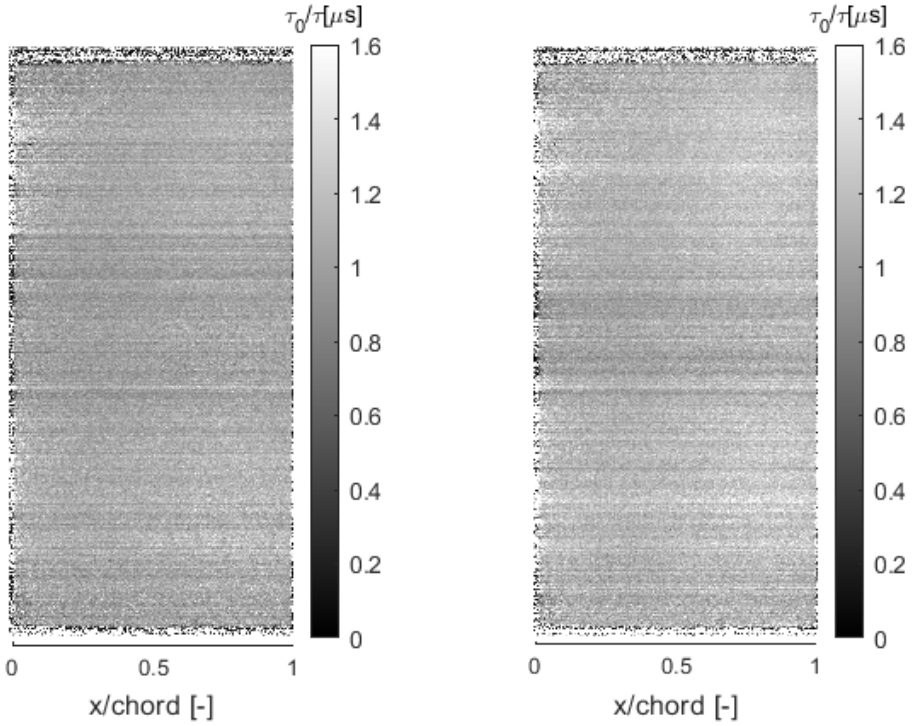


**Figure 6.22:** Lifetime ratios, $\tau_0/\tau$, for the pressure side experiments. On the left: the ratio using the lifetime at ambient pressure before the run. On the right: the ratio using the lifetime at ambient pressure after the run.

amount of PSP applied to this airfoil configuration.

From the lifetime ratio results, it can be concluded that firstly, the amount of PSP applied to the models is crucial for obtaining results with less levels of noise. Secondly, the changes in surface pressure can be visualised with PSP, which makes it possible to see the region on the airfoil experiencing the supersonic flow and the shock wave. Thirdly, the method is non-intrusive, making the experimental data more accurate.

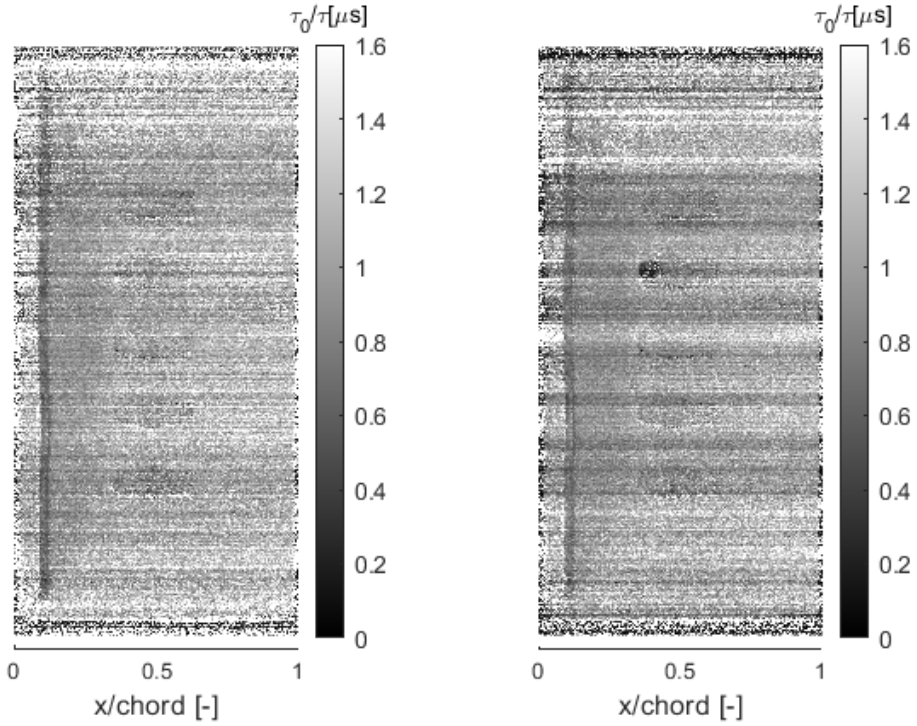


**Figure 6.23:** Lifetime ratios, $\tau_0/\tau$, for the suction side with SCBs. On the left: the ratio using the lifetime at ambient pressure before the run. On the right: the ratio using the lifetime at ambient pressure after the run.

## 6.3. Pressure results

For the computation of the pressure coefficients, the corrected Mach number for the experiments was used. The corrected Mach number for the OAT15A is 0.75 for a set Mach number of 0.72 at $\alpha$=3.5$^o$.(Solana Pérez (2017))

The pressure coefficient can be computed as:

$$C_P = \frac{p - p_\infty}{q_\infty} \tag{6.1}$$

With a freestream pressure of $p_\infty$= 1.39 bar, according to $\frac{p_\infty}{p_t} = \left(1 + \frac{\gamma-1}{2}M_\infty^2\right)^{\left(\frac{-\gamma}{\gamma-1}\right)}$ with $p_t$ being the chamber pressure of 2 bar, $\gamma$ = 1.4 and $q_\infty = \frac{\gamma}{2}pM^2$.

### 6.3.1. Shifted Pressure and Coefficients

The lifetime ratios can be converted into pressures and from there into the pressure coefficients. When looking at the pressure coefficients, these appear to be shifted in comparison with the $C_P$ values found in the literature (Brunet et al. 2005). Therefore, a shift in the results was made, each of the pressure coefficients was shifted by a specific value to match the trailing edge results from the literature. The values for the shift are presented in Table 6.1. Figures 6.24 and 6.25 show the plots for the pressure and the pressure coefficient of the pressure side of the airfoil. From those shifted coefficients the new pressure was computed and also plotted. From

the pressure before and after the shift, the pressure using the data before the wind tunnel run has an error of 0.2871 bar and an error of 0.3916 bar when using the data after the run. From the plot is clear that the shift is lower in the computation using the data from before the wind tunnel run than when the data from after the run was used. The discrepancy in the pressure remains more or less constant throughout the entire chord.

**Table 6.1:** Table showing the $C_P$ shift values for computing the pressures using PSP with the data before the wind tunnel run and after the wind tunnel run.

| | Pre: $C_P$ shift [-] | Post: $C_P$ shift [-] |
|---|---|---|
| Clean configuration | +0.3 | +0.1 |
| SCB configuration | -0.3 | -0.5 |
| Pressure side | +0.75 | +0.55 |

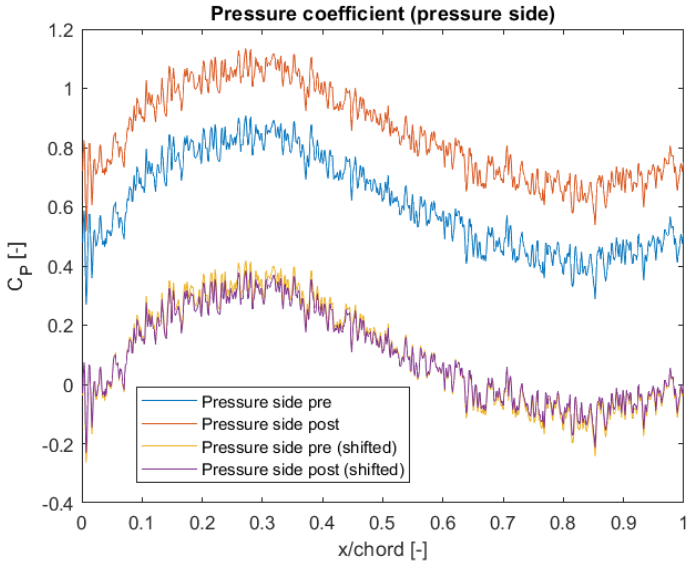


**Figure 6.24:** Pressure coefficient throughout the whole span of the airfoil with a shift in the computed coefficient to make it fit for the trailing edge conditions from literature.

For the suction side clean configuration, see Figures 6.26 and 6.27, also a shift in values is visible. The shift for the clean configuration is smaller than for the pressure side. The pressure shift varies by 0.0940 bar for the case using the data before the run and 0.2245 bar for the case using that after the run. The plots show that the pressure obtained with the data and equation from before the run yields a lower shift, especially towards the trailing edge of the airfoil. However, the shift in pressure obtained with the data after the run increases towards the trailing edge.

Figures 6.28 and 6.29 shows the pressure and its coefficients before and after shifting. By recalculating the pressures from the shifted pressure coefficients, the pressure appears to vary by 0.2611 bar for the case using the data before the run and 0.1044 bar for the case using the data after. These plots show a different trend than those of the clean configuration. For this case, the shift is greater when the data and equation from before the wind tunnel run are used.

To check for any discrepancies in the pressure coefficients throughout the entire span, the span was split into three different sections: top (Figure 6.32), bottom (Figure 6.33) and middle

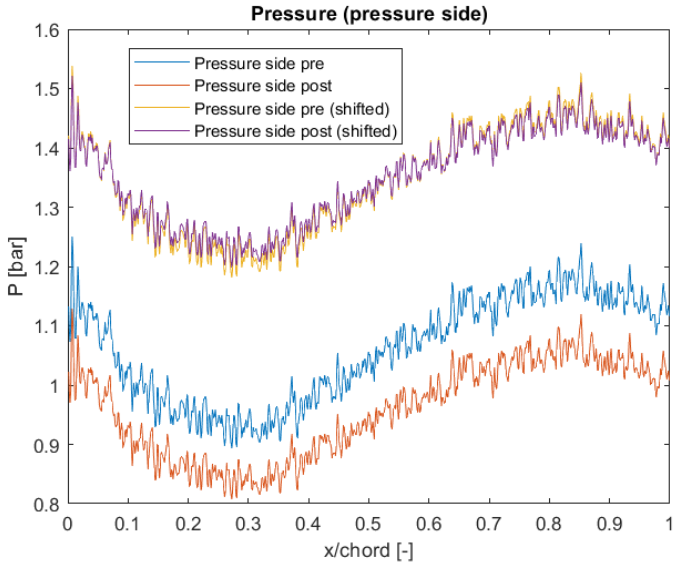


**Figure 6.25:** Pressure throughout the whole span of the airfoil with the shift to fit the trailing edge value from literature.

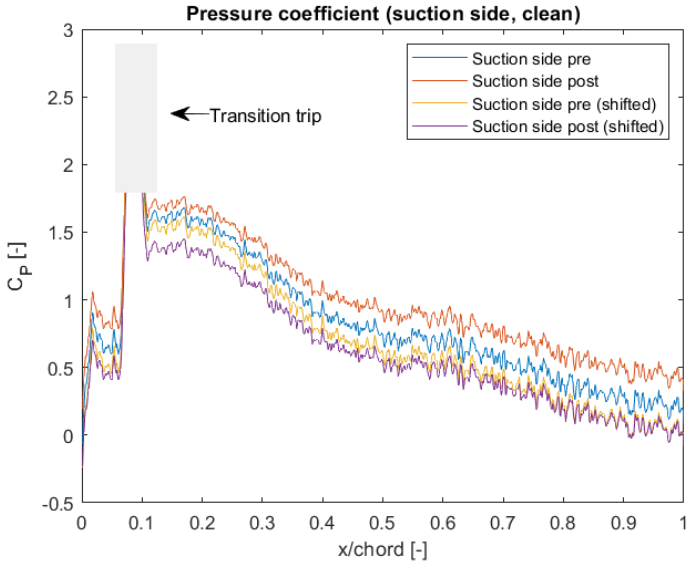


**Figure 6.26:** Pressure coefficient throughout the whole span of the airfoil for the clean configuration with a shift in the computed coefficient to make it fit for the trailing edge conditions from literature.

(Figure 6.34). The $C_P$ of the clean configuration does not vary drastically with respect to the location on the span. However, the configuration with the SCBs does vary depending on the span location. One reason for this is that the SCB has an effect on the flow and thus the pressure. Depending on if only the location where a SCB was located is used to compute the coefficient a different result will be obtained.

With the pressure coefficient and the small angle of attack assumption, the normal force coefficient is computed. The normal force coefficient can be assumed to be approximately the

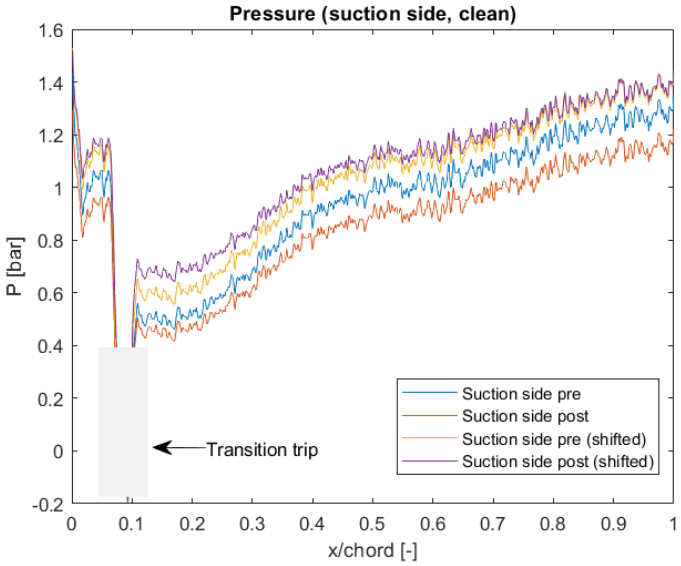


**Figure 6.27:** Pressure throughout the whole span of the airfoil for the clean configuration with the shift to fit the trailing edge value from literature.

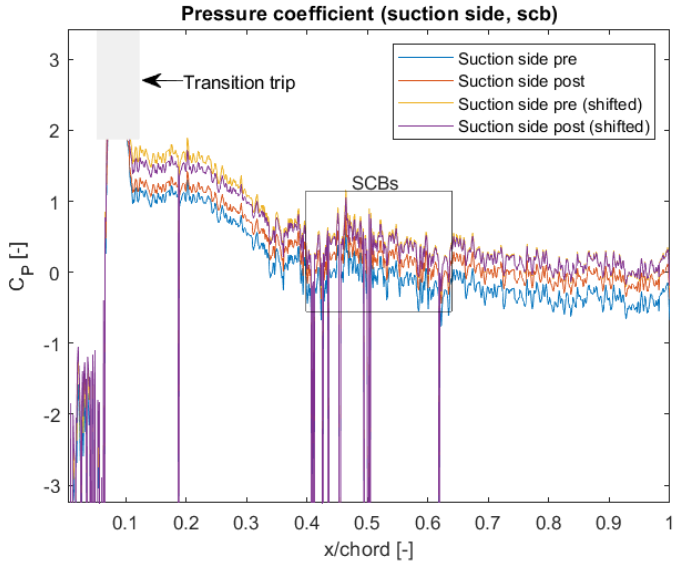


**Figure 6.28:** Pressure coefficient throughout the whole span of the airfoil for the configuration with SCBs with a shift in the computed coefficient to make it fit for the trailing edge conditions from literature.

lift coefficient as long as the angle of attack $< 5^o$.

$$C_N = \frac{1}{c}\int_0^1 (C_{Pl} - C_{Pu})\, dx \qquad \alpha \leq 5^o \tag{6.2}$$

The computed normal force coefficients are the following:

- $C_N$ 0.1301 for the clean configuration.
- $C_N$ -0.9261 for the configuration with SCBs before removing the outliers and -0.7261 after removing the outliers.

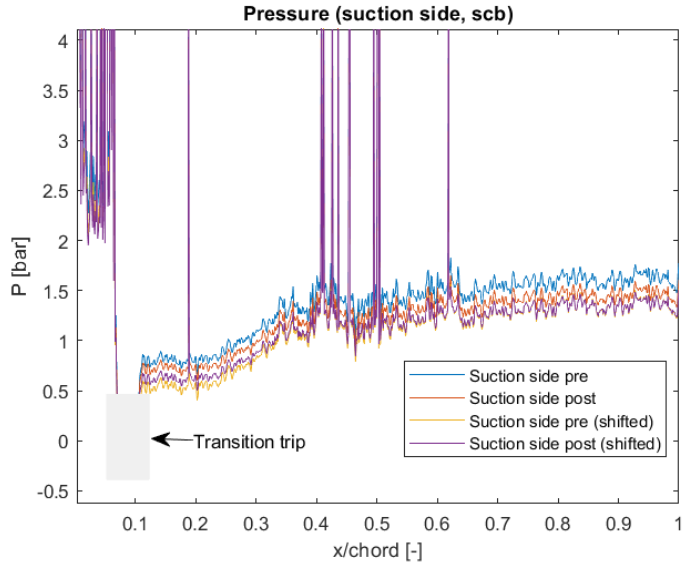


**Figure 6.29:** Pressure throughout the whole span of the airfoil for the configuration with SCBs with the shift to fit the trailing edge value from literature.

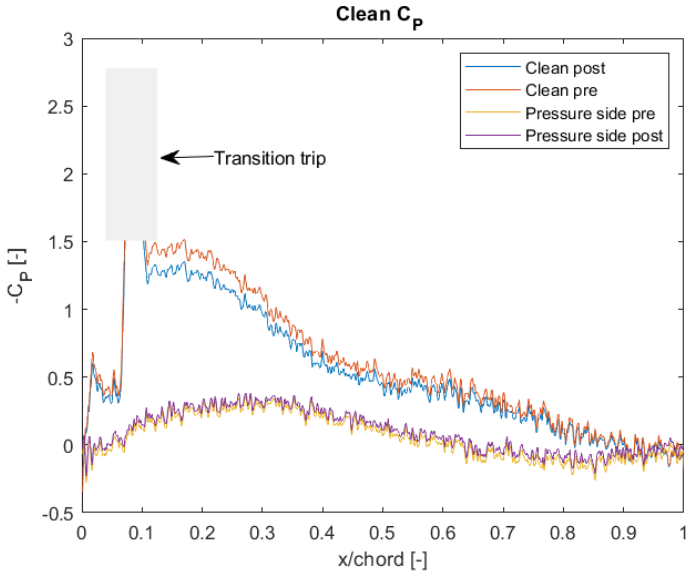


**Figure 6.30:** Pressure coefficient of the clean configuration.

From the computed normal force coefficients, it is clear that the objective of obtaining the lift coefficient for the OAT15A supercritical airfoil with and without SCBs was not entirely successful. The normal force coefficient for the clean configuration shows a positive sign, which means that there is a positive lift. However, the normal force for the configuration with the SCBs is negative, which is most likely caused by the high error in pressure right before the transition trip and the slight dip close to the trailing edge of the chord.

The two main takeaways from this section are the following:

- Being able to control the temperature in the calibration and also being able to measure it during the experiments is crucial because of the temperature dependence of PSP.
- To always cover fully the model with PSP because the data from the configuration with

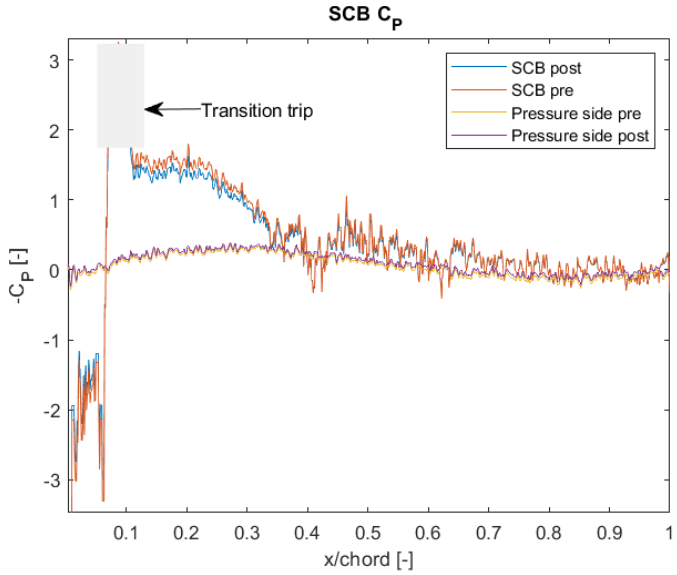


**Figure 6.31:** Pressure coefficient of the configuration with SCBs with the outliers removed.

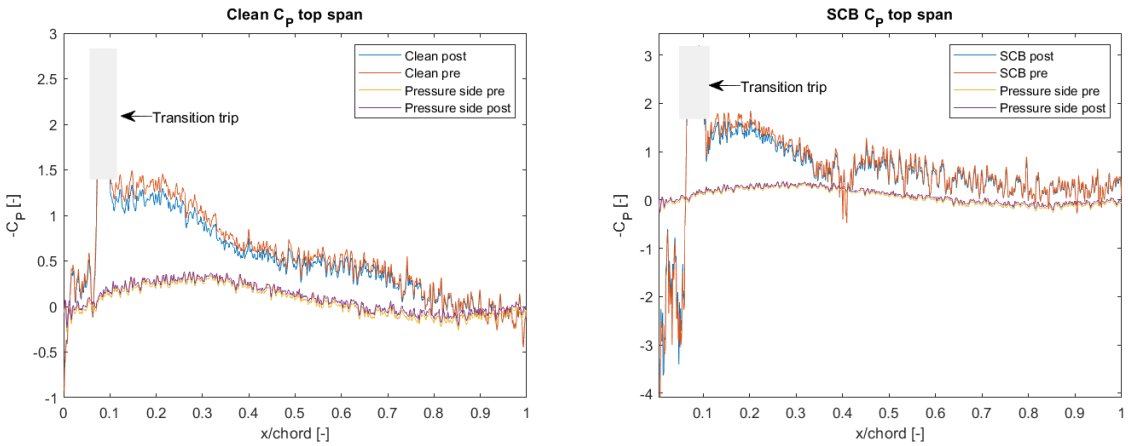


**Figure 6.32:** On the left: pressure coefficient with the clean suction side. On the right: pressure coefficient with SCBs on the pressure side.

SCBs has higher noise levels than the rest due to not having enough paint for full coverage.

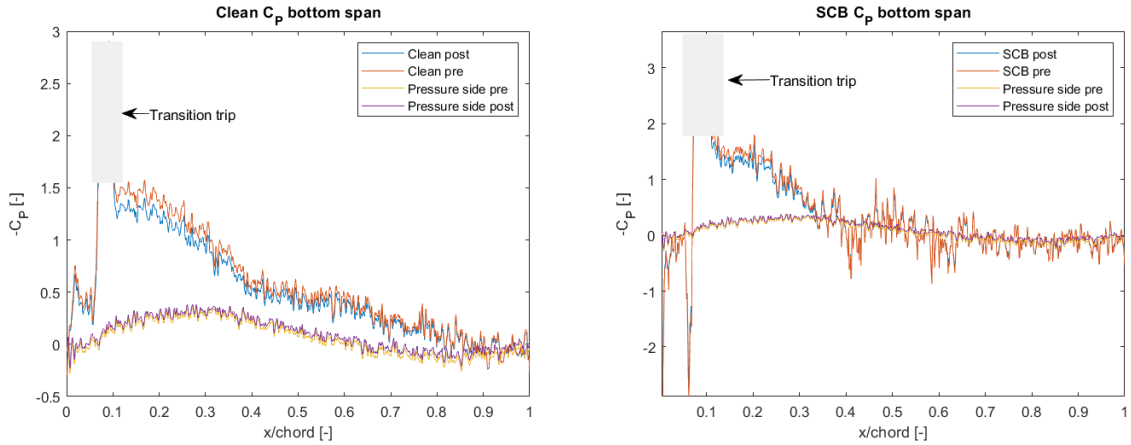


**Figure 6.33:** On the left: pressure coefficient with the clean suction side. On the right: pressure coefficient with SCBs on the pressure side.

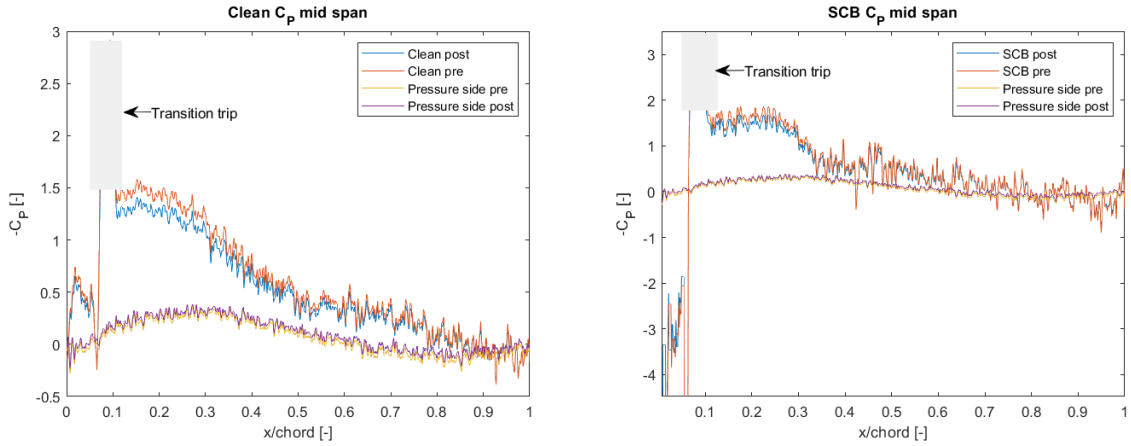


**Figure 6.34:** On the left: pressure coefficient with the clean suction side. On the right: pressure coefficient with SCBs on the pressure side.

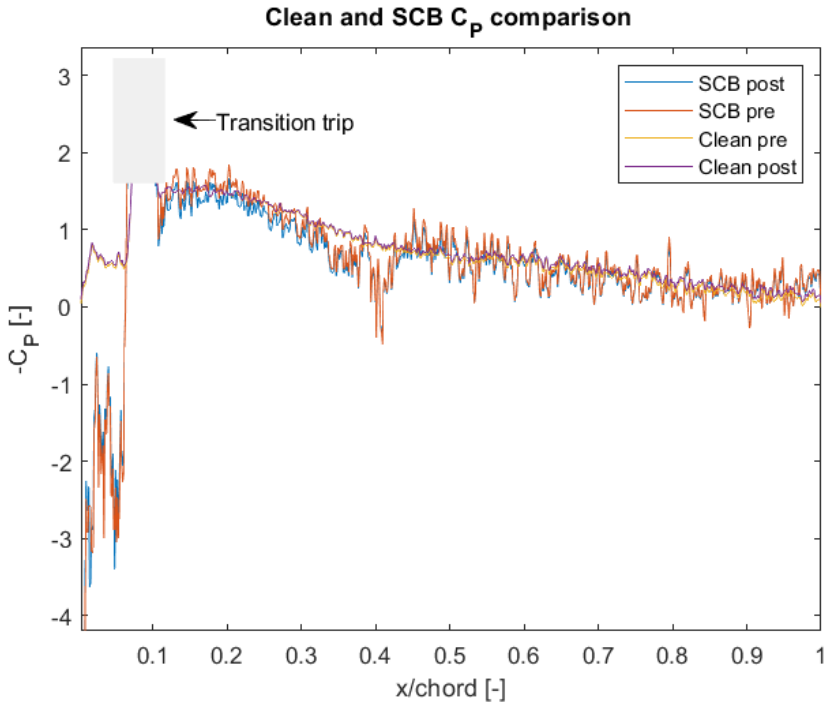


**Figure 6.35:** Cp wholespan

# 7

# Discussion

The purpose of this chapter is to present a more in-depth discussion of the results presented in Chapter 6 with a comparison to the findings from the literature, what types of errors are responsible for the discrepancies and what can be improved in the future for PSP experiments.

## 7.1. Comparison with literature

Brunet et al. (2005) did a numerical study on the OAT15A supercritical airfoil during buffer. For their study, they did experimental experiments and numerical simulations using different numerical methods. Figure 7.1 shows their found pressure coefficients. In the graph, the experimental data shows a shock wave happening earlier in the chord than in the simulations.

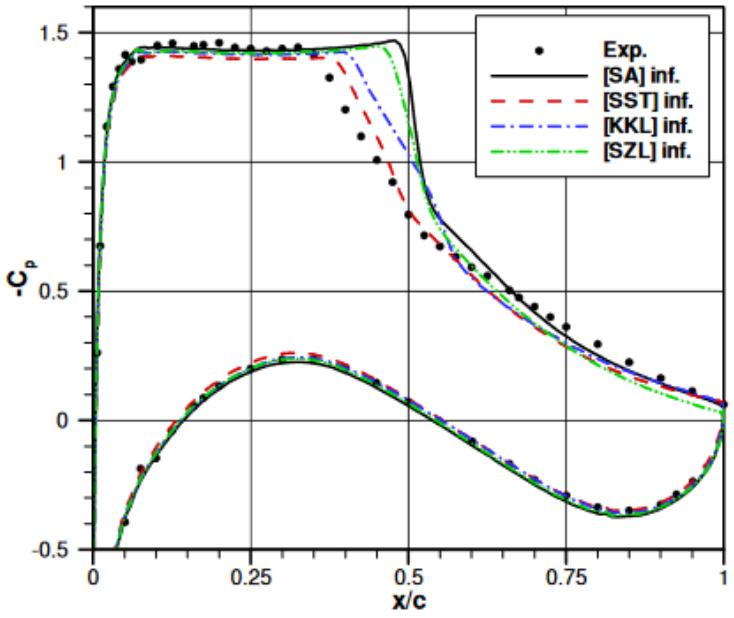


**Figure 7.1:** $C_p$ plots from the numerical study performed by Brunet et al. (2005): Mean pressure distributions with different turbulence models for $\alpha = 3.5^o$.

Figure 7.2 shows the comparison of the results from the experiments with the clean airfoil configuration with those from the experiments by Brunet et al. (2005). It is clear that the shape

from the obtained coefficients differs from that found in the literature. The transition trip on the model causes an error in determining the coefficients. Furthermore, the data from the literature shows a greater range in the $C_P$ values. From the plot, it is noticeable that the shock wave in these experiments occurs earlier than what is found in the literature with an agreement in the lowest pressure coefficient of -1.5. The pressure side of the data from the literature also shows a higher pressure coefficient by the leading edge and around 0.85 of the chord. Figure 7.3 shows the comparison with the results from the configuration with SCBs. The results from the configuration with SCBs have the shock more upstream in the chord than the clean configuration.

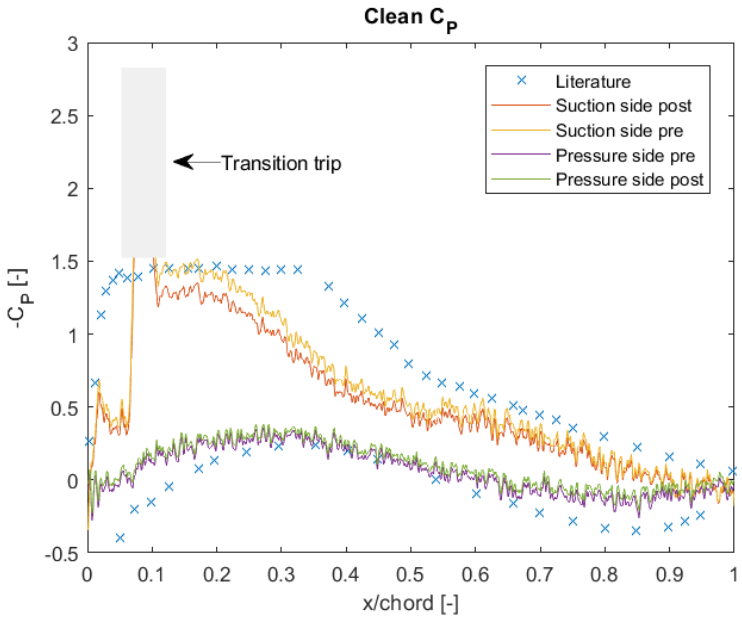


**Figure 7.2:** $C_p$ plots from the experiments performed by Brunet et al. (2005), next to the clean configuration.

Jacquin, Brion, et al. (2016) have also presented work on the OAT15A supercritical airfoil. The results from their work show the shock wave on the OAT15A airfoil moving from 0.4 to 0.55 of the chord, which corresponds to the research shown in Figure 7.1.

### 7.1.1. Effects of the shock control bumps

Section 2.4 explains how SCBs can improve the aerodynamic performance of transonic wings by influencing the flow conditions such as shock strength, position and the pressure gradient after the shock. This occurs by the SCB splitting the shock into multiple weaker shocks. The SCBs used in the experiments are 3D, which means that the shock goes along their central axes, which leads to 3D SCBs improving the Buffet margin. However, the peak aerodynamic performance can decrease. Figures 7.2 and 7.3 show the effect created by the SCBs in terms of the pressure coefficient, where there is an earlier and more drastic increase in the pressure coefficients at the location where the shock begins. Figure 7.4 shows a comparison of the intensities between the two airfoil configurations. It is noticeable that the clean configuration has a more gradual decrease in intensity when moving towards the trailing edge, meanwhile, the SCBs configuration has already a drop at the beginning of the SCBs in the centre of the model's span.

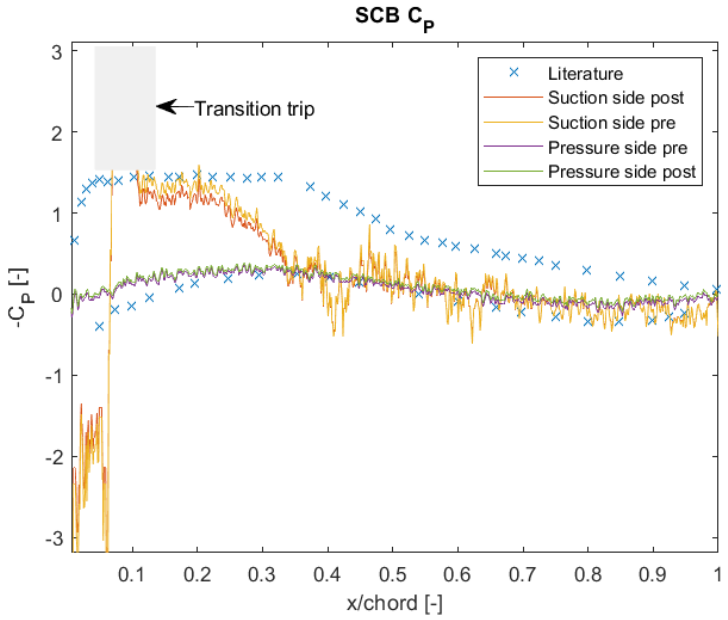


**Figure 7.3:** $C_p$ plots from the experiments performed by Brunet et al. (2005), next to the configuration with SCBs.

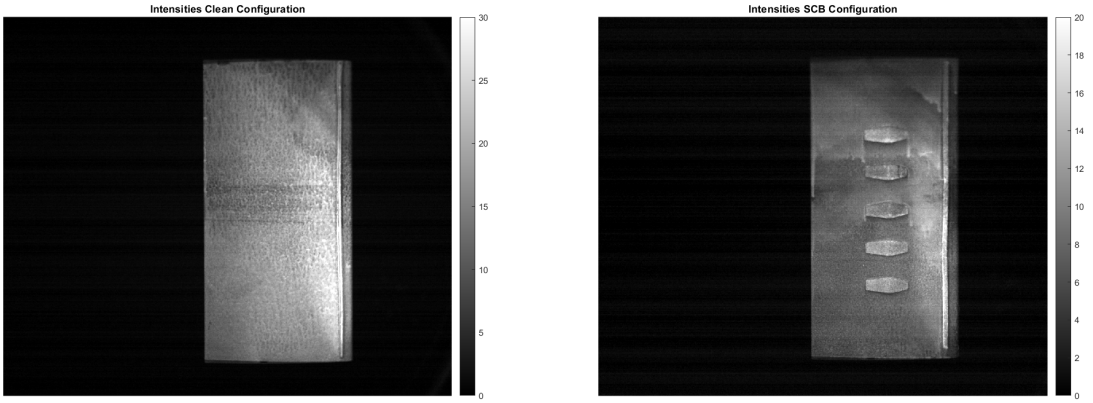


**Figure 7.4:** The plots of the intensities, the clean configuration shows a less drastic drop in intensity than the configuration with the SCBs. Caused by the weaker shock created at the start of the centre SCBs, which slows the flow down before the main shock.

### 7.1.2. Effects of the surface temperature on measurements

Due to equipment limitations, the surface temperature could not be measured. In the results, the pressures were shifted such that the pressure and suction side coefficients would meet at the trailing edge. However, the comparison with the literature shows that although the coefficient distributions match better after the shift, the values at the leading edge do not match. When the temperature can be accounted for during the calibration and the main experiments, the pressure can be calculated in a more exact manner. During the wind tunnel run, the airflow gets colder which means that the decay rate of the luminophores also decreases resulting in lower perceived pressure. This means that in reality, the pressure could have been higher during the experiments than that measured with PSP. Figure 7.5 and 7.6 show how the temperature affects the slope of the decay rate of the luminophores. This means that the pressure coefficient plots from the experiments have a slight variation in value depending on the temperature at

said location on the chord.

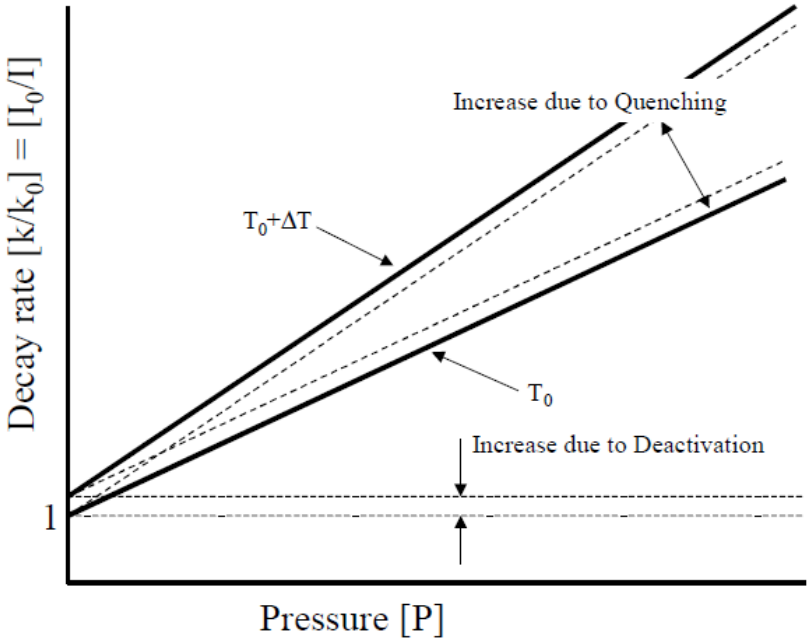


**Figure 7.5:** Normalised decay rate as function pressure and temperature (Mantel (2005))

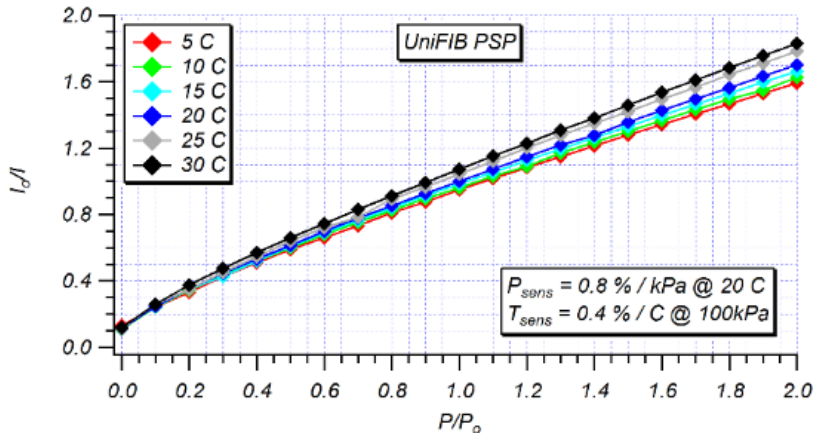


**Figure 7.6:** Data regarding the intensity of the paint depending on the pressure at different temperatures.

### 7.1.3. Effects of the number of images averaged.

The data acquisition for the experiments consisted of capturing the model 100 times. To understand what the effect is of averaging a high amount of images, Figure 7.7 the pressure coefficient of the pressure side of the OAT15A. The plot shows how with an increasing number of images, the noise decreases. The image also shows how the placement of the entire $C_P$ curve completely changes depending on the number of images used.

Furthermore, the turbulence in the flow creates fluctuations in the data between acquisitions. The error from the data during the flow has some turbulence is dependent on the amount of data acquired, which reduces as more data is collected. Due to the instability in the transonic

flow, the statistical error in the measurements is high. To account for this, 100 images were averaged and filtered in time using their standard deviation to minimise the error.

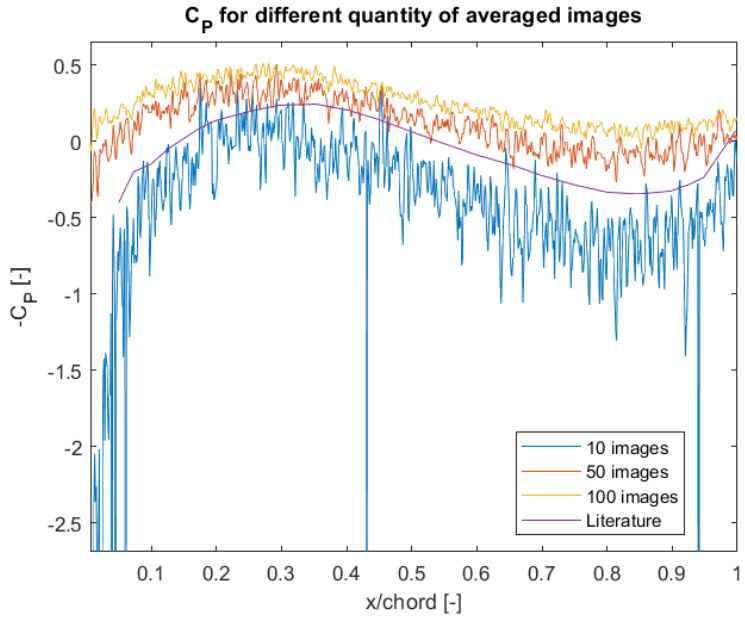


**Figure 7.7:** Pressure coefficient for the averaging of different quantities of images compared to literature.

## 7.2. Sources of error

Experimental fluid dynamics has the biggest advantage in being able to deal with real flows. However, experiments come with some disadvantages, such as the time and costs required, boundary conditions, limited test ranges, experimental errors, etc. (Scarano (2013)). This section deals with the possible scenarios during testing and their possible contribution towards the experimental error.

According to Scarano (2013), there are two types of measurement errors. The first type is the systematic (or biased) error, which is caused by constant factors, so the measured value has a continuous deviation from the actual value. It is difficult to identify this error and it increases the number of samples does not reduce it. The other errors are random errors, which are random deviations of the measurement values.

There are three typical errors in experimental aerodynamics that come from systematic and random errors, which are flow facility-related errors, errors due to measurement instruments, fluctuation due to turbulence and statistical errors.

### 7.2.1. Bias and random errors

The main bias errors in the experiments include the error in the timing of the pulse. The reason is that the timing of when the Stanford pulse generator would trigger the lamps shifted in the order of tenths of microseconds. This error was mostly dealt with and improved. Another bias error is the one caused by the limited calibration. As already mentioned, the temperature during the calibration in the pressurised chamber could not be changed and the temperature during the wind tunnel experiments could not be measured. This lack of data on temperature creates an error in the data, which generates faulty results.

A very recurrent random error during the experiments is the captured camera noise. This noise cannot be prevented and the only way to minimise it is by averaging multiple captures. Another important random error is the slight deviations in the Mach number during the experiments. The flow in the wind tunnel remains quite stable during the run, however, the Mach number oscillates slightly around the set value during the run.

### 7.2.2. Flow facility-related errors in the experiments

These types of errors occur due to the limitations created by the testing environment, such as the pressurised chamber and wind tunnel. These errors can be both systematic or random. They should be estimated and if possible also corrected for.

- The first possible error of this category is a slight change in the angle of attack of the airfoil when the wind tunnel was running. The change in the angle of attack would cause the airflow to behave differently due to the change in perceived geometry affecting the pressure on the airfoil.
- The vibrations in the room are caused by the high-speed runs in the wind tunnel. These vibrations can shake up the camera and lamps just enough to have the airfoil in less focus. This can impact the quality of the images leading to a different lifetime, which leads to a different pressure.
- Distance between the camera and the wind tunnel model. If the camera is too close, the entire model does not fit in the image, so the camera needs to be slightly further away. The problem with having the camera further away from the model is that there are fewer photons arriving at the camera's sensor, so the images become noisier.

### 7.2.3. Errors due to measurement instruments

These errors depend on the specific precision of the instruments used to complete the experiments. Some of the errors from the instruments are:

- The not constant trigger-exposure reaction time between the camera and the pulse generator. This translates into the timing between the camera and LEDs being up to 2-10$\mu$s shifted. Unfortunately, this causes a different lifetime, hence a different pressure.
- Differences in the amount of paint on each model and per test. If a part of the model does not have a proper coat of paint, there will be more noise in the images, which affects the quality of the measurements.
- The paint sensitivity is 0.8% per kPa. And the range of the paint is from 0kPa to 200kPa.[1]

### 7.2.4. Offset error in the measurements

The total offset error in pressure from the experiments is larger than that presented by Vardaki et al. (2010), where the error was found to be 700Pa≈0.007 bar. This offset is from the pressure shift that occurred because of the lack of temperature measurements. Table 7.1 shows the maximum errors for all of the cases computed. Even when the errors were accounted for by the shifting in the pressure coefficients, the lift coefficient, normal force coefficient, at $\alpha$=3.5$^o$ for the case with SCB does not make sense because it is negative. The $C_N$ for the clean configuration is 0.1301, which is positive. However, no data on the lift coefficient for the OAT15A airfoil has been documented but the coefficient seems to be lower than in reality. One reason could be the

[1] https://innssi.com/wp-content/uploads/Pressure_Sensitive_Paint/UniFIB/Documentation/UniFIB-PSP-UF-XXX-Data-Sheet.pdf

discrepancy at the leading edge of the data, where the pressure coefficient was higher than expected and then lower at the transition trip line for the clean configuration. The configuration with the SCBs had a larger discrepancy with also the pressure and suction coefficients being practically equal to each other on the passing the mid-chord of the airfoil.

**Table 7.1:** Table showing the maximum error values from the computed pressures using PSP with the data before the wind tunnel run and after the wind tunnel run.

| | Pre: max error [bar] | Post: max error [bar] |
|---|---|---|
| Clean configuration | 0.0940 | 0.2245 |
| SCB configuration | 0.2611 | 0.1044 |
| Pressure side | 0.2811 | 0.3916 |

### 7.2.5. Uncertainty in pressure measurement

Table 7.2 presents the root mean square and standard deviations of the region presented in Figure 7.8 for the case with the reference pressure before the wind tunnel run. For the case of the SCBs, the standard deviation is almost as large as the RMS value, which translates into very low reliability of measurements. The pressure side results are the most reliable in having the STD only a fraction of the RMS.

**Table 7.2:** The RMS and STD values of the square marked in 7.8

| Pre run as $P_0$ | RMS (0.7-0.75c) [-] | STD (0.7-0.75c) [-] | RMS (0.75-0.8c) [-] | STD (0.75-0.8c) [-] |
|---|---|---|---|---|
| Presssure side | 0.1016 | 0.0438 | 0.1270 | 0.0323 |
| Suction side clean | 0.4005 | 0.0435 | 0.3336 | 0.0673 |
| Suction side SCB | 0.2143 | 0.0954 | 0.1783 | 0.1213 |

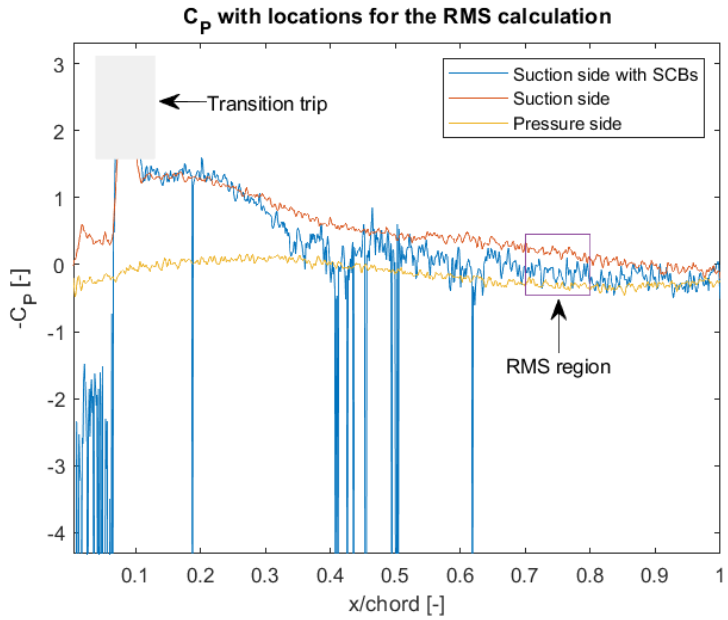


**Figure 7.8:** Plot showing the region for the computation of the RMS and STD values with the pre-run data as the reference.

Table 7.3 presents the root mean square and standard deviations of the region presented in Figure 7.9. In the case of the SCBs, the same pattern as for the computation with the data

before the run can be seen; the STD is more than 50% the RMS. For this data, the case of the suction side in the clean configuration shows the most promise with the lowest STD for the RMS value.

**Table 7.3:** The RMS and STD values of the square marked in 7.9

| Post run as $P_0$ | RMS (0.7-0.75c)[-] | STD (0.7-0.75c) [-] | RMS (0.75-0.8c)[-] | STD (0.75-0.8c) [-] |
|---|---|---|---|---|
| Presssure side | 0.1009 | 0.0396 | 0.1244 | 0.0292 |
| Suction side clean | 0.3950 | 0.0393 | 0.3342 | 0.0608 |
| Suction side SCB | 0.2006 | 0.0862 | 0.1678 | 0.1096 |

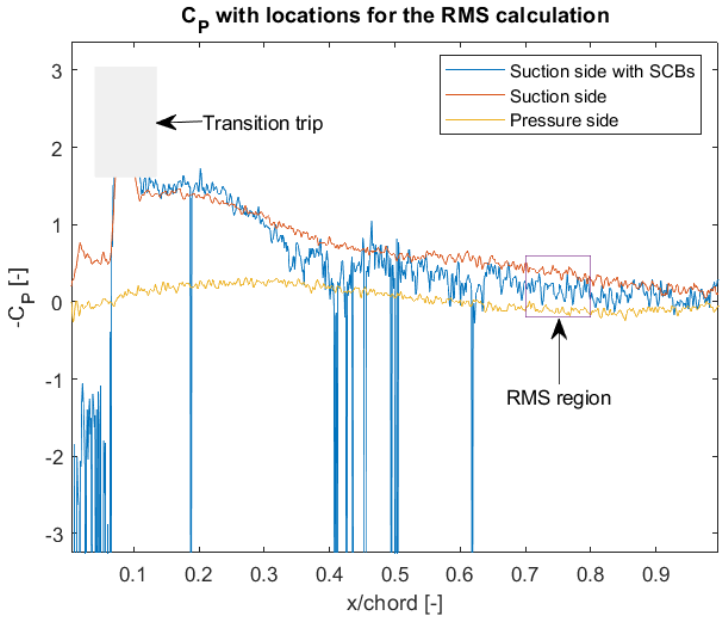


**Figure 7.9:** Plot showing the region for the computation of the RMS and STD values with the post-run data as the reference.

# 8

# Conclusion

## 8.1. Synopsis of the research

For determining what **effect shock control bumps have on the average pressure and lift coefficient of a supercritical airfoil during buffet by using the average surface pressure obtained with pressure sensitive paint**, the first thing to familiarise oneself with is the background information on transonic flow and buffet. The flow instability during the transonic regime was brought up together with two ways to decrease it, which consist in using a supercritical airfoil and shock control bumps. The supercritical airfoil postpones the Mach number and location on the airfoil at which the shock wave begins, and the shock control bumps split the main shock to have multiple weaker shock waves. Chapters 3 presented the necessary pressure sensitive paint information to understand the principle behind the technique and what the possibilities are. Chapters 4 and 5 presented the methodologies, data handling and calibration with as goal to perform **measurements using pressure sensitive paint and obtain reliable data**. Chapter 6 presented the results from the experiments, the chapter began by presenting all the images from the experiments and the computed lifetimes, and at the end of the chapter, the computed **surface pressures from the experiments using the OAT15A supercritical airfoil in transonic conditions** are given. Finally, Chapter 7 provided more in-depth information on what the **effect of the shock control bumps is on the surface pressure of the supercritical airfoil during buffet**. In the end, it was clear that the objective of the research **to apply pressure sensitive paint to measure the average pressure distribution in a transonic wind tunnel to study the effect of shock control bumps on a supercritical airfoil during buffet** was partially successful.

## 8.2. Conclusions from the experiments

Throughout the entire process of the research, it was clear that pressure sensitive paint can be a reliable technique for measuring surface pressure in a non-intrusive manner. The calibration of the paint in the pressurised chamber showed that at a controlled temperature, the relationship of the paint's lifetime to the pressure is linear. Reversing the process from the calibration equation to determine the pressures from the different paint lifetimes in the pressurised chamber showed that the equation could determine the pressure correctly up to about 2 bar at the specific temperature during the calibration tests.

The validation experiments, which also served as in-situ calibration, showed that when the pressure was determined using the data from wind tunnel experiments, the pressure was slightly off. The reason for this was the temperature differences on the model between the

measurements before the wind tunnel run, during the wind tunnel run and after the run. Therefore, the equation for determining the pressure had to be adapted twice, once when using the ratio with the data before the run and another time when the data after the run was used. With those changes, the pressure from PSP was close to that measured by pressure taps.

The main experiments showed that without having a reference pressure which can be used to twink the equation or knowledge of the temperature and its changes, the measured pressure will never be the real value. Although the adaptations made from the validation experiments helped with some temperature changes, the geometry of the model and flow conditions during the main experiments were different, therefore, the equation did not work to obtain the exact pressure value. However, the changes in the surface pressure throughout the chord of the airfoil were accurately resolved for the pressure side and the clean configuration experiments, providing a normal force coefficient of 0.1301. The experiments of the airfoil with shock control bumps did not show reliable results overall due to the lower intensity captured during the experiments because the paint was finished before properly covering the model with SCBs, ensuring the unreliability of the results for the configuration with SCBs, providing a normal force coefficient of -0.7261.

### 8.2.1. Improvements for future experiments

The first recommendation for future experiments with the pressure sensitive paint technique is to have a way to control the temperature during the calibration of the paint and to be able to measure the surface temperature of the model prior to, during and after the wind tunnel runs. Furthermore, in future experiments, at least another wind tunnel run per case is necessary to improve the statistics of the experiments. Also, the more data is obtained, the more outliers can be taken out, leading to more trustworthy results. Finally, to account for any differences in data acquisition, the model should always be fully covered in PSP and, the camera and LED lamps should always stay in the same location with respect to the model.

# References


Anderson, J. D. (2011). *Fundamentals of Aerodynamics, Fifth Edition in SI Units*. McGraw-Hill.

Ashill, P. R. and J. L. Fulker (1992). "A Novel Technique for Controlling Shock Strength of Laminar-Flow Aerofoil Sections". In: pp. 175–175.

Bell, J. H. et al. (2001). "Surface Pressure Measurements Using Luminescent Coatings". English. In: DOI: 10.1146/annurev.fluid.33.1.155.

Birkemeyer, J., H. Rosemann, and E. Stanewsky (2000). "Shock Control on a Swept Wing". In: *Aerospace Science and Technology* 4.3, pp. 147–156.

Bruce, P. J. K. and S. P. Colliss (2014). "Review of Research into Shock Control Bumps". English. In: *Shock Waves*. DOI: 10.1007/s00193-014-0533-4.

Brunet, V. et al. (2005). "A complete experimental and numerical study of the buffet phenomenon over the oat15 airfoil". In: *ONERA: Tire a Part* 35, pp. 1–9.

D'Aguanno, A., F. Schrijer, and B. van Oudheusden (2019). "Study of Upstream Travelling Waves in Transonic Buffet". English. In: ed. by Christian J. Kähler et al., pp. 430–440. DOI: 10.18726/2019_3.

Eastwood, J. P. and J. P. Jarrett (2012). "Toward Designing With Three-Dimensional Bumps for Lift/Drag Improvement and Buffet Alleviation". In: *AIAA journal* 50.12, pp. 2882–2898. DOI: 10.2514/1.J051740.

Engler, R. H., C. Klein, and O. Trinks (2000). "Pressure Sensitive Paint Systems for Pressure Distribution Measurements in Wind Tunnels and Turbomachines". In: *Measurement Science and Technology* 11.7, pp. 1077–1085. DOI: 10.1088/0957-0233/11/7/32010.1021/ed074p697.

Gianelis, Nicholas F., G. A. Vio, and O. Levinski (2017). "A Review of Recent Developments in the Understanding of Transonic Shock Buffet". English. In: *Progress in Aerospace Sciences*. DOI: 10.1016/j.paerosci.2017.05.004.

Gouterman, M. (1997). "Oxygen Quenching of Luminescence of Pressure Sensitive Paint for Wind Tunnel Research". English. In: *Journal of Chemical Education*. DOI: 10.1021/ed074p697.

Harris, C. D. (1990). "NASA supercritical airfoils: A matrix of family-related airfoils". In.

Hilton, W. F. and R. G. Fowler (1952). *Photographs of Shock Wave Movement*.

Iovnovich, M. and D. E. Raveh (2012). "Reynolds-averaged Navier-Stokes study of the shock-buffet instability mechanism". In: *AIAA journal* 50.4, pp. 880–890.

Jacquin, L., V. Brion, et al. (2016). "Testing in aerodynamics research at ONERA: The example of the transonic buffet". In: *Aerospace Lab* 12, pages–1.

Jacquin, L., P. Molton, et al. (2009). "Experimental Study of Shock Oscillation over a Transonic Supercritical Profile". In: *AIAA journal* 47.9, pp. 1985–1994. DOI: 10.2514/1.30190.

Jahanmiri, M. (2011). *Pressure Sensitive Paints: The Basics and Applications*. Tech. rep. Göteborg, Sweden: Chalmers University of Technology.

König, B. et al. (2009). "Numerical and Experimental Validation of Three-Dimensional Shock Control Bumps". In: *Journal of Aircraft* 46.2, pp. 675–682. DOI: 10.2514/1.41441.

Lee, B. H. K. (1990). "Oscillatory Shock Motion Caused by Transonic Shock Boundary-Layer Interaction". In: *AIAA journal* 28.5, pp. 942–944. DOI: 10.2514/3.25144.

Liu, T. and J. P. Sullivan (2005). *Pressure and Temperature Sensitive Paints*. Springer-Verlag Berlin Heidelberg.

Mantel, J. (Oct. 2005). "Understanding and Improving Pressure Sensitive Paint Based on Luminescence Decay". MA thesis. Delft University of Technology.

Mason, W. (2006). *7. Transonic Aerodynamics of Airfoils and Wings 7.1 Introduction*.

Merienne, M. C. et al. (2013). "Transonic buffeting investigation using unsteady pressure-sensitive paint in a large wind tunnel". In: *51st AIAA Aerospace Sciences Meeting including the New Horizons Forum and Aerospace Exposition*, p. 1136.

Messina, M. (Mar. 2020). "Study of Shock Control Bumps on Controlling Transonic Buffet". MA thesis. Delft University of Technology, Universita degli Studi di Palermo Scuola Politecnica.

Milholen, W. and L. Owens (2005). "On the Application of Contour Bumps for Transonic Drag Reduction". In: *43rd AIAA Aerospace Sciences Meeting and Exhibit*, p. 462. DOI: 10.2514/6.2005-462.

Ogawa, H. et al. (2008). "Shock-Wave/Boundary-Layer Interaction Control Using Three-Dimensional Bumps for Transonic Wings". In: *AIAA journal* 46.6, pp. 1442–1452. DOI: 10.2514/1.32049.

Raghunathan, S. et al. (2008). "Periodic Transonic Flow and Control". In: *The Aeronautical Journal (1968)* 112.1127, pp. 1–16. DOI: 10.1017/S0001924000001949.

Scarano, F. (2013). *Experimental Aerodynamics*. University Reader.

Schanze, K. S. et al. (1997). "Temperature Dependence of Pressure Sensitive Paints". In: *AIAA journal* 35.2, pp. 306–310. DOI: 10.2514/2.92.

Sobieczky, H. and A. R. Seebass (1984). "Supercritical Airfoil and Wing Design". In: *Annual Review of Fluid Mechanics* 16.1, pp. 337–363. DOI: 10.1146/annurev.fl.16.010184.002005.

Solana Pérez, Roberto (2017). "On the unsteady development of the flow under transonic Buffet conditions". Delft University of Technology.

Stanewsky, E. and D. Basler (1989). *Mechanism and Reynolds Number Dependence of Shock-Induced Buffet on Transonic Airfoils*.

Tai, T. C. (1977). *Theoretical Aspects of Dromedaryfoil*. Tech. rep. Naval ship research and development center Bethesda MD.

Tambe, S. et al. (2022). "Spiral instability modes on rotating cones in high-Reynolds number axial flow". In: *Physics of Fluids* 34.3, p. 034109.

Terlizzi, A. (July 2020). "On Transonic Buffet: Experimental Investigation of Cross-Flow Effects and Aspect Ratio Influence". MA thesis. Delft University of Technology, University of Pisa.

Tijdeman, H. (1977). "Investigations of the Transonic Flow around Oscillating Airfoils". In: *NLR-TR 77090 U*.

Vardaki, E. et al. (2010). "Pressure sensitive paint measurements at the ARA transonic wind tunnel". In: *27th AIAA Aerodynamic Measurement Technology and Ground Testing Conference*, p. 4796.

Vos, R. and S. Farokhi (2015). *Airfoil Aerodynamics*.

Whitcomb, R. T. (Aug. 1974). "Review of NASA Supercritical Airfoils". In.

Yun, T. et al. (2017). "Transonic Buffet Control Research with Two Types of Shock Control Bump Based on RAE2822 Airfoil". In: *Chinese Journal of Aeronautics* 30.5, pp. 1681–1696. DOI: 10.1016/j.cja.2017.07.011.